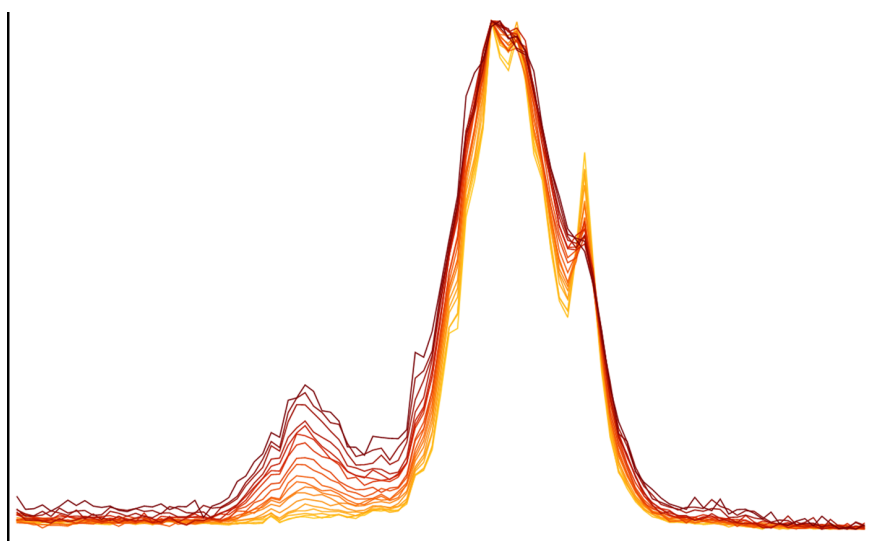




Ln^{3+} doped rare earth phosphate nanocrystals for luminescence nanothermometry

Daniël W. Groefsema

November 26, 2018



Master's thesis

Supervised by

Robin G. Geitenbeek, MSc

and

Prof. dr. A. Meijerink

CONDENSED MATTER AND INTERFACES
DEBYE INSTITUTE FOR NANOMATERIALS SCIENCE
UTRECHT UNIVERSITY



Utrecht University

Abstract

In the field of nanomaterials, information about the local temperature in a system can be crucial for the performance of these systems. In literature, several methods of temperature measurements on small length scales, in the order of micrometers, have been reported. Of these techniques, luminescence nanothermometry is a promising non-invasive technique.

For some applications, however, the working temperature range of these techniques is not yet sufficient to be able to apply it in processes at elevated temperatures, such as catalytic reactions.

In this thesis, different lanthanide-doped rare earth phosphate nanoparticles are investigated for the potential use as nanothermometers. Due to the small size of these particles, in the order of ~ 5 nm, very small spatial resolutions can, in principle, be obtained, while thermally coupled energy states in the lanthanide dopants can provide a temperature dependent change in the band shape of the emission.

Luminescent dysprosium-cerium co-doped lanthanum phosphate nanoparticles were synthesized and subsequently coated with a pure LaPO_4 shell, to enhance the luminescence. In these particles, a temperature dependency of the emission from the $^4\text{F}_{9/2}$ and $^4\text{I}_{15/2}$ energy levels was found up to a temperature of 250°C . Incorporation of the particles in silica spheres of ~ 40 nm provided further thermal stability, and temperature dependent emission was observed up to a temperature of 450°C .

Additionally, europium-doped LaPO_4 nanoparticles with a pure LaPO_4 shell were synthesized. In these particles, a temperature dependency of the emission from the $^5\text{D}_1$ and $^5\text{D}_0$ energy levels was found up to a temperature of $\sim 300^\circ\text{C}$.

Although further studies still have to be performed, these results provide a good indication that lanthanide-doped rare earth phosphate nanoparticles can be a useful addition to the variety of nanothermometry techniques available today.

Contents

1	Introduction	1
1.1	Nanothermometry techniques	1
1.2	Optical nanothermometry	2
1.3	Towards imaging catalysis	4
2	Theory	6
2.1	Lanthanide luminescence	7
2.1.1	Ln^{3+} energy levels	8
2.1.2	Transitions and selection rules	11
2.2	Radiative and non-radiative decay	13
2.3	Band shape luminescence nanothermometry	14
2.4	$\text{REPO}_4\text{:Ln}$ for nanothermometry	15
2.4.1	Lanthanide dopants	15
2.4.2	REPO_4 nanoparticles	15
2.4.3	Nanoparticle coating	16
3	Methodology	18
3.1	Synthesis	18
3.1.1	Microcrystalline $\text{REPO}_4\text{:Ln}$	18
3.1.2	$\text{REPO}_4\text{:Ln}$ nanoparticles	18
3.1.3	$\text{REPO}_4\text{:Ln/REPO}_4$ core-shell nanoparticles	19
3.1.4	Silica coating	20
3.2	Characterization	20
3.2.1	X-ray diffraction	21
3.2.2	Transmission electron microscopy	21
3.2.3	Photoluminescence	21
4	Results & discussion	22
4.1	$\text{LaPO}_4\text{:Dy,Ce}$	22
4.1.1	$\text{LaPO}_4\text{:Dy}$ nanoparticles	22
4.1.2	$\text{LaPO}_4\text{:Dy,Ce}$ nanoparticles	25
4.1.3	$\text{LaPO}_4\text{:Dy,Ce/LaPO}_4$ nanoparticles	28
4.1.4	$\text{LaPO}_4\text{:Dy,Ce/LaPO}_4\text{/Si}$ nanoparticles	32
4.2	$\text{LaPO}_4\text{:Dy,Ce}$ nanoparticles on gold nanoparticles	41
4.3	$\text{LaPO}_4\text{:Eu}$	43
4.3.1	$\text{LaPO}_4\text{:Eu}$ nanoparticles	43
4.3.2	$\text{LaPO}_4\text{:Eu/LaPO}_4$ nanoparticles	46
4.4	$\text{LaPO}_4\text{:Er,Yb}$	50

4.4.1	LaPO ₄ :Er,Yb nanoparticles	50
4.4.2	LaPO ₄ :Er,Yb/LaPO ₄ nanoparticles	51
4.4.3	LaPO ₄ :Er,Yb bulk	51
4.5	YPO ₄ :Er,Yb	54
4.5.1	YPO ₄ :Er,Yb nanoparticles	54
4.5.2	YPO ₄ :Er,Yb/YPO ₄ nanoparticles	54
4.5.3	YPO ₄ :Er,Yb/LaPO ₄ nanoparticles	56
4.5.4	YPO ₄ :Er,Yb bulk	57
5	Conclusions	60
5.1	LaPO ₄ :Dy,Ce nanoparticles for nanothermometry	60
5.2	LaPO ₄ :Eu nanoparticles for nanothermometry	60
5.3	LaPO ₄ :Er,Yb nanoparticles for nanothermometry	61
5.4	YPO ₄ :Er,Yb nanoparticles for nanothermometry	61
6	Outlook	62
7	Acknowledgements	63
Appendices		
A	Dieke diagram	65
B	Chemicals	66
C	LaPO₄:Dy,Ce-coated gold nanoparticles; coating procedure	67
D	Bibliography	68

Chapter 1

Introduction

The field of nanothermometry aims to obtain information about the local temperature of a system on very small length scales, up to spatial resolutions lower than one micrometer. This information can be crucial in the understanding of small-scale systems, of which the performance is dependent on temperature. Examples of these systems, where nanothermometry can play a pivotal role, are numerous in the fields of nanotechnology and cellular chemistry, such as micro/nano-electronic systems, photonic devices and catalytic systems.^{1,2}

In the field of micro/nano-electronics, high transistor densities and switching speeds on a chip can lead to a large heat flux on the chip. The presence of these so-called ‘hot spots’ on the chip can be detrimental for the performance of these systems. Here, obtaining information about the local temperature could facilitate detailed studies and lead to a better understanding of the hot spots, in order to repress the creation of these hot spots and thereby improve the system.

Another area where temperature fluctuations on small length scales are important, is in integrated photonic devices. The performance of these devices depends on the optical properties of the constituting materials, such as refractive index and spectral properties of band gap structures. Because these properties can be affected by changes in temperature, knowledge about the local temperature can contribute to the development of efficient and reliable photonic devices.

Furthermore, temperature fluctuations can play a crucial role in catalytic systems. The outcome of a chemical reaction can be highly dependent on the temperature at which the reaction takes place. Since these reactions are often either endothermic or exothermic, the local temperature can vary from the bulk temperature and because catalytic processes typically benefit from large surface areas (and thus small particle sizes), the measurement of temperature fluctuations on small length scales can be vital for the analysis and development of catalytic materials.

Due to major advances towards smaller and smaller length scales in the field of nanotechnology, the demands on spatial resolution for temperature measurements have increased, to the point where conventional thermometry is no longer sufficient. Therefore, the field of nanothermometry has developed into a very active field of research. This has led to new and interesting studies of different nanothermometry techniques.^{1,2}

1.1 Nanothermometry techniques

The numerous potential applications of nanothermometry have resulted in a variety of different techniques to achieve thermal sensing. Each of these techniques has its own advantages and drawbacks.

For different fields of research, different nanothermometry techniques may be applicable. The different techniques can be roughly classified into three main groups: electrical, mechanical and optical nanothermometry.

Some examples of these different techniques include:

- Point contact nanoscale thermocouples
based on measurements of thermoelectric voltage³
- Liquid-in-nanotube thermometers
based on the thermal expansion of liquids⁴
- Luminescent nanoparticle thermometers
based on temperature dependent luminescence properties^{1,2}

Many of the available point contact techniques use the principle of atomic force microscopy, where the sample surface is scanned with a small tip, that responds to changes in temperature. This method can, in principle, reach spatial resolutions similar to that of conventional atomic force microscopy.

Despite this, there are some drawbacks for this method. First, it is a surface scanning method, so it can only be used to produce two dimensional images of a relatively flat surface. This puts major restrictions on the types of systems that can be measured this way. Second, long acquisition times are necessary for the tip to scan the whole surface, making the analysis a very time consuming process. Third, due to the requirement of physical contact between the tip and the sample, the thermal measurement can be affected by heat transfer between the tip and the sample, resulting in less accurate temperature measurements.⁴

The liquid-in-nanotube thermometry technique, on the other hand, does not have the drawbacks of the surface scanning techniques. This technique is based on the thermal expansion of liquid gallium within a carbon nanotube that is closed on one end and open on the other end. The volume of gallium inside the carbon nanotubes expands as the temperature increases. When exposed to air, the gallium is oxidized and a gallium oxide layer sticks to the inner wall of the nanotube. The height of this gallium oxide layer within the tube can be analyzed after cooling the system down and is a measure of the temperature that has been achieved in the system.

One major disadvantage for this technique is the fact that temperature information can only be abstracted after cooling the system down, so temperature fluctuations can not be measured *in situ*, but only the maximum achieved temperature can be determined. Furthermore, these nanotubes have to be closed on one end and open on the opposite end, which is difficult to achieve with the current synthesis technique. The amount of nanotubes with one open end and one closed end in the obtained product, is reported to be only 2 – 5 vol%. Another disadvantage, is that the process is irreversible; the carbon nanotubes can only be used once.⁴

1.2 Optical nanothermometry

The limitations mentioned above have led to the development of a variety of non-contact thermal sensing techniques, based on temperature dependent optical properties of optically active materials.^{1,2} Among the different methods of optical nanothermometry, the use of temperature dependent luminescence is a promising technique, because a high sensitivity and spatial resolution can be obtained, whilst maintaining short acquisition times, using relatively straight-forward emission analysis.

The luminescence of these systems can depend on different luminescence parameters, some of which are shown in figure 1.1. The temperature dependent parameters shown in this figure include spectral position, band shape, bandwidth, intensity, polarization and lifetime.

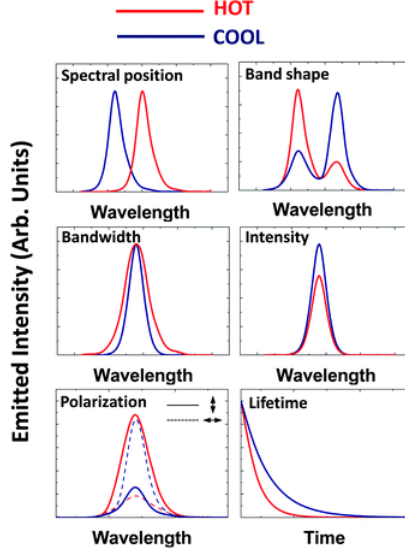


Figure 1.1: Temperature dependent spectral parameters.²

The use of temperature dependent spectral position of cadmium selenide quantum dots emission has been demonstrated by Yang *et al.*⁵ Here, CdSe quantum dots that show emission with a maximum intensity centred around ~ 655 nm after two-photon near-infrared excitation, are inserted in living cells. Then, a calcium complex is added to the cell culture to elevate the Ca^{2+} concentration and thereby induce Ca^{2+} shock in the cells. The heat generation within the cell, which is a result of the Ca^{2+} shock, is then determined by measuring the red-shift of the emission. This temperature dependent red-shift is attributed to various phenomena, such as the thermally induced variation in quantum yield of different emitting levels and the solvent's refractive index as well as thermal expansion of the quantum dots and thermally induced variation of the band gap energy, the latter being proposed to be the dominant effect.⁶ The major contribution to this process comes from a temperature dependent electron-lattice interaction, that shifts the relative positions of the conduction band and the valence band. According to the Varshni equation, the temperature dependent energy gap then becomes⁷:

$$E_g = E_0 - \frac{\alpha T^2}{T + \beta} \quad (1.1)$$

Here, E_g is the band gap energy, E_0 is the band gap energy at $T = 0$ K and α and β are material-specific constants.⁷

With this technique, a spatial resolution close to 400 nm is reported with temperatures ranging from room temperature up to 50 °C. Although this technique is suitable for biological systems, the small temperature range makes it inapplicable for systems at elevated temperatures above 50 °C.

In addition to the use of luminescent quantum dots as optical nanothermometers, the temperature dependent emission intensity of an organic dye molecule, rhodamine B, has been used

by Ross *et al.* to measure the fluid temperature in a microfluidic system.⁸ Here, the intensity of the emission from the rhodamine B dye, that occurs after excitation around 525 nm, decreases as the temperature of the system increases. A dilute solution of rhodamine B in a carbonate buffer is loaded in a microfluidic channel and, after applying an electric field over the channel, the temperature of the buffer increases due to Joule heating. To determine the increase in temperature, the fluorescence intensity is measured with a standard fluorescence microscope and a CCD camera.

With this technique, a spatial resolution of 1 μm with temperatures ranging from room temperature up to 90 °C is reported. This is an almost twofold increase in the temperature range compared to the previous example, but it is still relatively narrow and the spatial resolution for this technique is more than twice as large. Furthermore, the intensity of the dye emission, and thus the temperature determination, can be influenced by fluctuations in both the concentration of the dye and the intensity of the excitation light, which makes accurate temperature measurements challenging.

In another study, Xu *et al.* showed the use of fluorescent lanthanide ions (Er^{3+} and Tm^{3+}) incorporated in $\alpha\text{-NaYb}(\text{Mn})\text{F}_4/\text{NaYF}_4$ nanoparticles with an average diameter of 27 nm, to achieve temperature measurements based on the band shape of the lanthanide emission.⁹ Lanthanide ions typically show several emission peaks, of which the ratio of intensity can be dependent on the local temperature (more information about band shape luminescence nanothermometry and lanthanide emission can be found in chapter 2). After excitation with a 980 nm laser, the emission was measured with a fluorescence spectrometer.

Xu *et al.* reported a temperature dependent emission intensity ratio over a temperature range from -150 °C up to 150 °C. Although this is a large increase in the temperature range compared to the previous examples, the measurement of higher temperatures is still challenging. Additionally, information about the spatial resolution that can be achieved with this technique is lacking and applications of this system have not yet been reported.

Of these examples, band shape luminescence nanothermometry is an effective and promising method of temperature sensing, because it is based on the intensity ratio between two different emission bands. The relative intensity of these emission bands is solely dependent on the temperature and not on fluctuations of the local concentration of emitting centers or the intensity of the excitation source.^{9,10}

1.3 Towards imaging catalysis

In the field of optical nanothermometry, the use of trivalent lanthanide ions (Ln^{3+}) as emitting centres has been studied. A variety of nanothermometry techniques, based on this concept, has been developed for temperature sensing in different systems.^{1,2}

For the measurement of temperature fluctuations in catalytic reactions, however, suitable techniques have not yet been developed. Due to the typically high temperatures in catalytic processes, which can be in the order of hundreds of degrees Celsius,¹¹ and the presence of (catalytically) active reagents, relatively robust particles, that are chemically and thermally stable, are required in order to measure temperatures in catalytic processes. As for now, nanothermometry systems that meet these demands have not yet been synthesized.

In a more recently emerging field within the area of catalysis, the phenomenon of surface plasmon resonance has been studied.¹² In this approach, noble metal nanoparticles, such as gold nanoparticles, are exposed to an external electromagnetic field, thereby resonantly exciting surface plasmon modes of the particles (i.e. nearly free electron oscillations coupled to an incident electromagnetic wave). The energy that is absorbed this way, is subsequently converted to lattice

vibrations on a picosecond time scale, resulting in very rapid and local heating of the particle.¹² However, crucial information about the behaviour of these particles, such as the temperature that can be achieved with this technique, is lacking. Due to the small sizes of these particles (in the order of 50 to 100 nm in diameter¹³) and the local nature of this effect, optical nanothermometry potentially provides a useful tool for the study of these systems, given that an adequate spatial resolution can be acquired, which can, in principle, be obtained by employing suitably small temperature sensing nanoparticles.

In the work described by this thesis, band shape luminescence nanothermometry with rare earth (RE) phosphate nanoparticles is investigated. These REPO₄ nanoparticles are doped with fluorescent lanthanide ions or lanthanide ion pairs, such as europium, dysprosium/cerium or erbium/ytterbium, which are expected to show temperature dependent emission. In order to enhance the luminescence of the particles, they are coated with a pure REPO₄ shell on the surface of the doped nanoparticles, which is expected to decrease surface quenching effects. To stabilize the doped REPO₄:Ln/REPO₄ core-shell particles over a wide temperature range, the particles are coated with a silica shell. This way, REPO₄:Ln/REPO₄/Si particles with a core-shell-shell structure are obtained with high luminescence and stability, making them suitable for nanothermometry applications at elevated temperatures.

Chapter 2

Theory

Lanthanides (sometimes referred to as rare-earth elements, although this definition includes the elements yttrium and scandium of atomic numbers 21 and 39, respectively) are the elements situated in the top row of the f-block elements at the bottom of the periodic table. The lanthanide series goes from lanthanum to lutetium, with atomic numbers 57 – 71. In the 3+ oxidation state, which is the most common oxidation state for lanthanides, the 4*f* orbitals gradually get filled, going from 4*f*⁰ for lanthanum up to 4*f*¹⁴ for lutetium. The corresponding electron configurations are shown in table 2.1 in the column marked “Ln³⁺”. Since the ions are more stable with completely empty, completely filled or half-filled orbitals, Ce⁴⁺ (4*f*⁰), Eu²⁺ (4*f*⁷), Tb⁴⁺ (4*f*⁷) and Yb²⁺ (4*f*¹⁴) are also commonly encountered.¹⁴ An overview of the lanthanide elements, including their symbol, atomic number and electron configuration, is given in table 2.1.

Table 2.1: Overview of the lanthanide elements

Name	Symbol	Atomic nr.	Configuration	Ln ³⁺
Lanthanum	La	57	[Xe] 5 <i>d</i> ¹ 6 <i>s</i> ²	[Xe] 4 <i>f</i> ⁰
Cerium	Ce	58	[Xe] 4 <i>f</i> ¹ 5 <i>d</i> ¹ 6 <i>s</i> ²	[Xe] 4 <i>f</i> ¹
Praseodymium	Pr	59	[Xe] 4 <i>f</i> ³ 6 <i>s</i> ²	[Xe] 4 <i>f</i> ²
Neodymium	Nd	60	[Xe] 4 <i>f</i> ⁴ 6 <i>s</i> ²	[Xe] 4 <i>f</i> ³
Promethium	Pm	61	[Xe] 4 <i>f</i> ⁵ 6 <i>s</i> ²	[Xe] 4 <i>f</i> ⁴
Samarium	Sm	62	[Xe] 4 <i>f</i> ⁶ 6 <i>s</i> ²	[Xe] 4 <i>f</i> ⁵
Europium	Eu	63	[Xe] 4 <i>f</i> ⁷ 6 <i>s</i> ²	[Xe] 4 <i>f</i> ⁶
Gadolinium	Gd	64	[Xe] 4 <i>f</i> ⁷ 5 <i>d</i> ¹ 6 <i>s</i> ²	[Xe] 4 <i>f</i> ⁷
Terbium	Tb	65	[Xe] 4 <i>f</i> ⁹ 6 <i>s</i> ²	[Xe] 4 <i>f</i> ⁸
Dysprosium	Dy	66	[Xe] 4 <i>f</i> ¹⁰ 6 <i>s</i> ²	[Xe] 4 <i>f</i> ⁹
Holmium	Ho	67	[Xe] 4 <i>f</i> ¹¹ 6 <i>s</i> ²	[Xe] 4 <i>f</i> ¹⁰
Erbium	Er	68	[Xe] 4 <i>f</i> ¹² 6 <i>s</i> ²	[Xe] 4 <i>f</i> ¹¹
Thulium	Tm	69	[Xe] 4 <i>f</i> ¹³ 6 <i>s</i> ²	[Xe] 4 <i>f</i> ¹²
Ytterbium	Yb	70	[Xe] 4 <i>f</i> ¹⁴ 6 <i>s</i> ²	[Xe] 4 <i>f</i> ¹³
Lutetium	Lu	71	[Xe] 4 <i>f</i> ¹⁴ 5 <i>d</i> ¹ 6 <i>s</i> ²	[Xe] 4 <i>f</i> ¹⁴

2.1 Lanthanide luminescence

In lanthanide ions, generally, there are three types of electronic transitions:

- Broad $4f - 5d$ transitions
- Broad charge transfer transitions between metal and ligand
- Sharp, intraconfigurational $4f - 4f$ transitions

Of these different types of electronic transitions, the $4f - 4f$ transitions are responsible for characteristic lanthanide luminescence. The origin of this luminescence lies in the partially filled $4f$ orbitals of the trivalent lanthanide ions cerium to ytterbium. Because these elements have partially filled $4f^n$ orbitals (where $n = 1 - 13$), transitions within the $4f$ orbitals are possible.

An illustration of the radial distribution functions for $4f$, $5s$ and $5p$ orbitals is shown in figure 2.1. In this figure, it can be seen that the $4f$ orbitals are located closer to the nucleus (smaller value of r) with respect to the $5s$ and $5p$ orbitals. Since lanthanides have filled $5s$ and $5p$ orbitals, the $4f$ electrons are shielded from the surroundings by the $5s$ and $5p$ electrons. Due to this shielding, the $4f$ energy levels are, to a large extent, independent of the host lattice.

Additionally, the $4f$ electrons do not participate much in the lanthanide to ligand binding, so the internuclear distance remains almost the same upon excitation of a $4f$ electron to a higher energy $4f$ state. In figure 2.2, illustrations of the configurational coordinate diagrams for lanthanide ions ($4f - 4f$ transitions, figure 2.2a) and for a general luminescent material (e.g. $4f - 5d$ transitions, figure 2.2b) are shown. Due to the small change in internuclear distance (small ΔR in figure 2.2a), lanthanides show sharp, characteristic absorption and emission lines in their luminescence spectra with a small, negligible Stokes shift.^{14,15} In contrast, most other luminescent materials have a larger change in internuclear distance (large ΔR in figure 2.2b) upon excitation and thus show broader emission peaks with larger Stokes shifts.

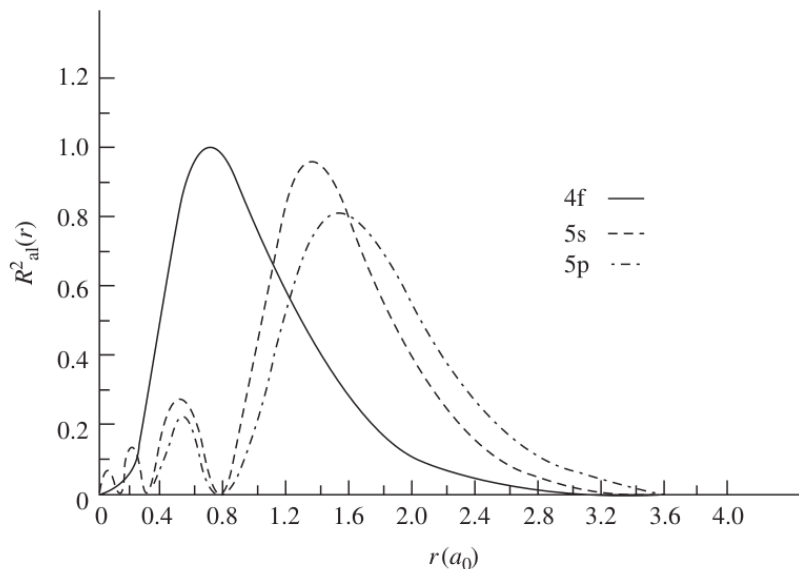


Figure 2.1: Example of radial distribution functions for $4f$, $5s$ and $5p$ orbitals.¹⁶

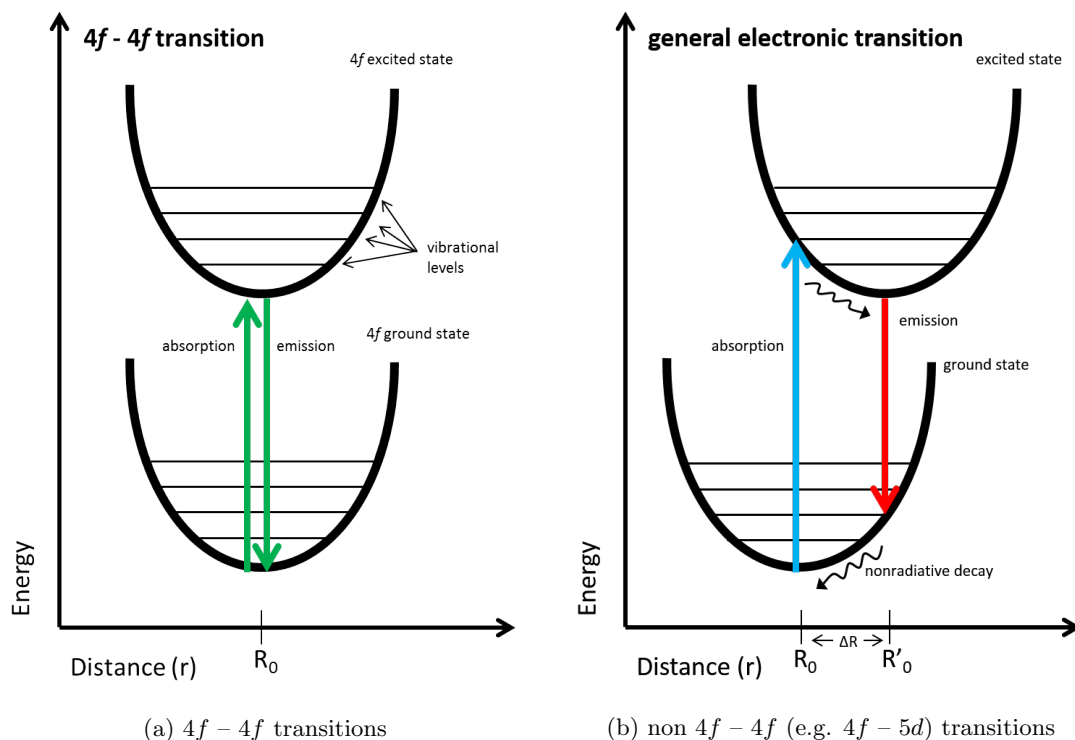


Figure 2.2: Configurational coordinate diagrams for different types of electronic transitions.

2.1.1 Ln^{3+} energy levels

In lanthanides, the partially filled $4f$ orbitals give rise to a large number of different energy levels. These energy levels are related to different distributions of the n $4f$ electrons over fourteen possible $4f$ orbitals (seven orbitals, each capable of having one electron with spin up and one with spin down). Due to electrostatic interactions and spin-orbit coupling, the energy levels for different $4f$ orbitals are split. This results in the rich energy level scheme characteristic for lanthanides.^{14,17}

The Dieke diagram (appendix A on page 65) is a well known diagram that depicts different energy levels for Ln^{3+} ions. Here, the horizontal bars represent energy levels of different Ln^{3+} ions (on the x-axis) and their relative energy (on the y-axis), with the thickness of the horizontal bars indicating the magnitude of the crystal-field splitting.¹⁸

Energy level splitting

The origins of the energy level splitting, as observed in the Dieke diagram, can be divided into three different types of interactions.

A schematic illustration of the energy level splitting, due to these interactions, is shown in figure 2.3. Here, the labels in the form of $^{2S+1}L_J$ originate from the term symbols, as will be discussed in the next section.

The three different types of interactions include:

- Electrostatic interactions:

For a given electron configuration, splitting of the energy levels occurs due to electrostatic interactions of different spatial distributions of the electrons (i.e. occupancy of different $4f$ orbitals). This leads to different repulsion interactions between the electrons and thus a different total orbital angular momentum.

- Spin-spin interactions:

For a given spatial distribution of the electrons, additional splitting of the energy levels occurs due to spin-spin interactions of the electrons. The difference in energy, here, lies in the different orientations of the electron spins with respect to each other, which leads to a different total spin angular momentum

- Spin-orbit coupling:

Finally, for a given electron spin orientation, additional splitting of the energy levels occurs due to spin-orbit coupling. This is a magnetic interaction where the magnetic moment of an electron, that arises from its orbital angular momentum, interacts with another magnetic moment of the electron, that arises from its spin angular momentum. Here, the difference in energy lies in the different orientations of the orbital angular momentum with respect to the spin angular momentum, resulting in a different total angular momentum.

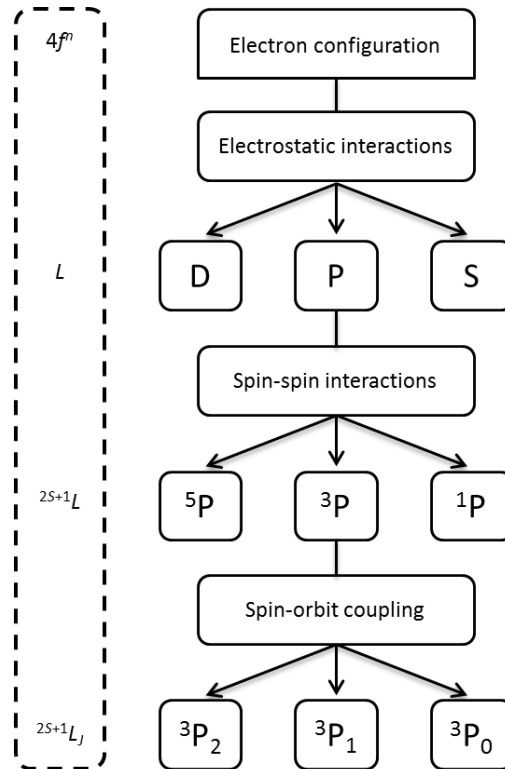


Figure 2.3: Illustration of energy level splitting due to different interactions.

It is worthy to note, that, generally, the coupling of all the spins and all the orbital angular momenta can be a complicated problem if there are multiple electrons outside a closed shell (as is the case for most lanthanides). However, if the spin-orbit coupling is weak, all the individual

angular momenta have to operate cooperatively in order for the spin-orbit coupling to be effective. This way, the total angular momentum can be thought of as a coupling between the total orbital angular momentum and the total spin, instead of coupling the individual angular momenta of the electrons. This is known as the Russel-Saunders coupling scheme.¹⁹

Although the spin-orbit coupling generally is weak only for lighter atoms (atomic numbers $Z < 30$), the $4f$ electrons in lanthanides penetrate only slightly through the inner shells of the atom and they experience only a fraction of the electric field at the nucleus. Therefore, despite their relatively high atomic numbers, the spin-orbit coupling is weak and the Russel-Saunders coupling scheme remains applicable for lanthanide ions.²⁰

Term symbols

For the discussion of the splitting of the different energy levels, term symbols will be introduced. Term symbols, generally, are a way of describing the different energy levels, based on the quantum numbers to describe orbitals.¹⁹ These quantum numbers are n , l and m_l . Here, n is a positive integer called the *principal quantum number*, which can have values of $1 \leq n \leq \infty$. The value of n indicates the energy and the radial expansion of the orbital. The quantum number l is called the *orbital quantum number* and can have values of $l = 0, 1, 2, \dots, (n-1)$. The value of l indicates the shape of the atomic orbital and the orbital angular momentum of the electron. The quantum number m_l is called the *magnetic quantum number* and gives information about the orientation of an atomic orbital in space. This quantum number can have integral values of $-l \leq m_l \leq +l$.

In term symbols, the energy levels are depicted by the general term $^{2S+1}L_J$. For example, the ground state of cerium is written as $^2F_{5/2}$. This symbol gives three pieces of information¹⁹:

1. L indicates the *total orbital angular momentum*, depicted by a letter
2. $2S + 1$ indicates the *multiplicity* of the term, depicted by a number
3. J indicates the *total angular momentum*, depicted by a number

The total orbital angular momentum, L , depicts the magnitude of the orbital angular momenta of the individual electrons combined. The permitted values of L (a non-negative integer) are obtained by coupling the individual orbital angular momenta l of the electrons, using the Clebsch-Gordan series:

$$L = l_1 + l_2, l_1 + l_2 - 1, \dots, |l_1 - l_2| \quad (2.1)$$

When there are more than two electrons to couple together, multiple series need to be used in succession. First, two electrons are coupled as in equation 2.1. Then, the next electron is coupled to the combined state, and so on. This way, the value of L can be determined, which is then converted into a letter:

$$\begin{array}{rcccccc} L = & 0 & 1 & 2 & 3 & \dots \\ \text{Letter:} & S & P & D & F & \dots \end{array} \quad (2.2)$$

The series of corresponding letters is derived from the nomenclature of orbitals (s, p, d, f) and is continued alphabetically, except for the omission of "J".

A closed shell has zero orbital angular momentum, because the individual orbital angular momenta of the electrons sum to zero. Therefore, only the electrons of partially filled shells are taken into account (the $4f$ -electrons for Ln^{3+} ions).

The multiplicity $2S + 1$ is based on the total spin angular momentum, S (a non-negative integer or half-integer). The spins of the individual electrons ($s = 1/2$ for each electron) are coupled together similar to equation 2.1 for the orbital angular momentum. The multiplicity is then given by $2S + 1$. For a closed shell, the electrons are all paired and $S = 0$ (there is no net spin). This gives a singlet term, because $S = 0$ thus $2S + 1 = 1$. For a single electron, $S = s = 1/2$ so $2S + 1 = 2$. This gives rise to a doublet term.

Finally, the total angular momentum J can be determined. The total angular momentum is the result of spin-orbit coupling of the electrons, using the Russel-Saunders coupling scheme (coupling of L and S). The permitted values of J are again obtained using the Clebsch-Gordan series:

$$J = L + S, L + S - 1, \dots, |L - S| \quad (2.3)$$

This way, the full term symbol can be written for the electronic energy states. For any ion, a number of these states is possible.

Ground state determination

To determine the ground state for the ion, Hund's rules have to be applied²¹:

1. The state with the highest spin multiplicity $2S + 1$ is the ground state
2. If there are more terms with equal multiplicity, the term with the highest L -value is the ground state
3. For a shell less than half-filled, the lowest value for J is the ground state

For a shell more than half-filled, the highest value for J is the ground state

Using these rules, the ground state for any ion can be written as a term symbol. For example, the ground state of a trivalent cerium ion ($4f^1$) has $L = 3$ (corresponding to the letter F), $2S + 1 = 2$ (one unpaired electron, $S = s = 1/2$) and $J_{min} = L - S = 5/2$. Thus, the ground state for Ce^{3+} is written as $^2\text{F}_{5/2}$. In the Dieke diagram (appendix A on page 65), it can be seen that this is indeed the lowest energy level for a Ce^{3+} ion. Similarly, the ground state of a trivalent ytterbium ion ($4f^{13}$) is labeled $^2\text{F}_{7/2}$, in accordance to the third of Hund's rules (since Yb^{3+} has a shell more than half-filled).

2.1.2 Transitions and selection rules

As mentioned above, lanthanide elements possess a large number of available energy levels, from which the characteristic lanthanide luminescence occurs. However, between these energy levels, not all transitions are observed in the excitation and emission spectra. The allowed transitions are described by a set of selection rules. It is worthy to note, that the selection rules are derived under several hypotheses, which are not always fulfilled (due to orbital mixing, for example). Therefore, when a given transition is "forbidden" by selection rules, this should be understood as "less probable". In the same way, transitions that are "allowed" by the selection rules, are "more probable".¹⁵

One important selection rule is Laporte's parity selection rule. This rule states that, for a given transition, there must be a change in parity for it to be allowed. In other words, the change in the orbital quantum number $\Delta l = \pm 1$. This means that transitions such as $s \leftrightarrow p$, $p \leftrightarrow d$ and $d \leftrightarrow f$ are allowed, whereas transitions such as $s \leftrightarrow s$, $f \leftrightarrow f$ and $p \leftrightarrow f$ are forbidden.¹⁴ The underlying principle for this rule is that a photon, that is absorbed or emitted by the system, has an intrinsic spin angular momentum, thus absorption or emission of a photon leads to a perturbation of the system. For the transition to take place, the difference between the initial and final state has to match the the angular momentum of the photon, i.e. the change in angular momentum of the electron must compensate the angular momentum that is introduced or carried away by the photon. For a transition where $\Delta l = 0$, there is no change in angular momentum of the electron to compensate the angular momentum of the photon. Similarly, for a transition where $\Delta l > 1$, the change in angular momentum of the electron overcompensates the angular momentum of the photon.¹⁹

Another important selection rule, is the spin selection rule. This rule states that, for a given transition, the overall spin can not change for it to be allowed ($\Delta S = 0$). This rule originates from the fact that photons do not affect the electron spins directly, so a transition that differs in spin between initial and final state, cannot be induced by a photon.¹⁹

However, the influence of a ligand field on the lanthanide ion can lead to interactions that result in the mixing of electronic states. This relaxes the selection rules to a small extent and transitions that would otherwise be forbidden (such as the characteristic $4f - 4f$ transitions), can become partially allowed.¹⁵

Generally, transitions between two energy levels can occur via a variety of mechanisms, the most important transitions being electric dipole transitions and magnetic dipole transitions. An overview of different types of transition mechanisms, including their selection rules and an indication of their oscillator strengths, is given in table 2.2. Here, the oscillator strength refers to the oscillating electric or magnetic vector of the radiation that interacts with the $4f$ electron, which is an indication of the probability of a transition to occur via that particular mechanism.²²

Table 2.2: Overview of different transition mechanisms.

Transition mechanism	<i>SLJ</i> selection rules	Oscillator strength
Electric dipole (ED)	$\Delta S = 0$ $ \Delta L \leq 1$; $L = 0 \leftrightarrow L' = 0$ is forbidden $ \Delta J \leq 1$; $J = 0 \leftrightarrow J' = 0$ is forbidden	$\sim 0.01 - 1$
Forced electric dipole (FED)	$\Delta S = 0$ $ \Delta L \leq 6$; if $L = 0$ or $L' = 0$, $ \Delta L = 2, 4, 6$ $ \Delta J \leq 6$; if $J = 0$ or $J' = 0$, $ \Delta J = 2, 4, 6$	$\sim 10^{-4}$ of ED
Magnetic dipole (MD)	$\Delta S = 0$ $\Delta L = 0$ $ \Delta J \leq 1$; $J = 0 \leftrightarrow J' = 0$ is forbidden	$\sim 10^{-6}$ of ED
Electric quadrupole (EQ)	$\Delta S = 0$ $ \Delta L \leq 2$; $L = 0 \leftrightarrow L' = 0, 1$ is forbidden $ \Delta J \leq 2$; $J = 0 \leftrightarrow J' = 0, 1$ is forbidden	$\sim 10^{-10}$ of ED

Note that, although a given transition may be forbidden for one mechanism, it might still be observed through another mechanism, albeit weaker than a fully allowed transition. Furthermore, additional selection rules based on the site symmetry of the ion can play a role, such that a

transition that is allowed by *SLJ* selection rules, can still be forbidden by site point group selection rules.²³ However, these site point group selection rules are beyond the scope of this thesis and will not be discussed further.

2.2 Radiative and non-radiative decay

In order to obtain high intensity luminescence, it is important that the energy states, from which the luminescence occurs, are well separated from other, lower energy states. Radiative transitions to the ground state (the luminescence of interest) can compete with non-radiative decay transitions of ions in solids.¹⁷ Therefore, the presence of energy states between the excited states and the ground state can give rise to non-radiative decay processes, that will result in quenching of the luminescence and thus a loss of signal in the measurement.

Generally, all energy that is absorbed by a material and not emitted as radiation, is dissipated as heat to the crystal lattice or through vibrations of ligands. These processes typically take place on a faster time scale than the emission of light.¹⁷ A rule of thumb is that radiative decay (the luminescence of interest) competes efficiently with non-radiative decay, if the difference in energy between the excited state and the first lower energy state is equal to or larger than five times the highest vibrational energy of the surroundings.²² If the energy gap is smaller, the excited state energy can simultaneously excite multiple high energy vibrations or phonons and the energy is dissipated non-radiatively as mentioned above, thereby quenching the luminescence. This process is called multi-phonon relaxation.^{15,17}

Multi-phonon relaxation especially is detrimental for luminescence in the presence of organic ligands or solvents. Organic bonds, such as O–H, N–H or C–H, typically have high vibrational energies of up to $\sim 3500\text{ cm}^{-1}$. As a result, the decay of a system in the presence of organic ligands has a relatively high probability to occur via a non-radiative pathway. One way to overcome this problem, is to incorporate the emitting centres in a crystalline host, instead of in organic complexes or solutions. This way, the emitting centres are separated from the organic species and non-radiative decay becomes less probable.²⁴

Energy transfer

Additional to multi-phonon relaxation, luminescence can also be quenched by energy transfer processes.¹⁷ Upon excitation to a higher energy level, the absorbed energy can be transferred from the absorbing ion (the donor) to a different ion (the acceptor) via a variety of mechanisms. The nature of this mechanism is dependent on the separation distance d between the donor and the acceptor and can be either radiative, if the separation is large ($d > \lambda/10$), or non-radiative, if the separation is small ($d \ll \lambda$). For both mechanisms, interactions between the dipole moments of the donor and acceptor species are involved.²⁵

When the concentration of emitting ions in a host lattice is large, the distances between the ions are small and energy transfer readily takes place. This way, the energy of an excited state can easily be transferred to neighbouring ions, until it reaches a defect in the lattice and is lost non-radiatively. This process is called concentration quenching. In order to reduce the concentration quenching effects, dopant concentrations should be suitably low (in literature, typical dopant concentrations of 0.1 % – 15 % are used for lanthanide-doped nanoparticles).¹⁵

2.3 Band shape luminescence nanothermometry

The concept of band shape luminescence nanothermometry (BSLNth) is based on systems, that have multiple emission bands or lines, of which the intensity ratio is dependent on the local temperature. Generally, there are two approaches to obtain such temperature dependent emission intensity ratios.

In the first approach (multi-centre BSLNth), the different emission bands or lines of interest originate from two different emitting centres. Here, the temperature dependent change in band shape arises from the different thermal quenching behaviour of each unique emitting centre,²⁶ or the temperature dependent energy transfer between these centres.^{27,28}

In the second approach (single-centre BSLNth), these emissions arise from different energy states of one unique emitting centre. In this case, the temperature dependent change in band shape arises from a thermally induced population redistribution over the different energy states of the emitting centre. The advantage of this approach, is that there is a single excitation process and the emission intensity ratio depends solely on the temperature dependent population redistribution. Naturally, this phenomenon is only observed if the population redistribution happens on a faster time scale than the radiative and non-radiative decay processes.

Generally, the energy states from which the temperature dependent emission occurs, are close to each other in energy, such that they are thermally coupled. Energy states are thermally coupled, if the energy difference between the states is in the order of $\Delta E \sim k_B T$. If this is the case, excitation of the system to a thermally coupled excited state is followed by a redistribution of the population over the coupled energy states. According to a Boltzmann distribution, the ratio of population of two thermally coupled energy states A and B is redistributed following an exponential relation, which is temperature dependent²⁹:

$$\frac{N_A}{N_B} = \exp\left(\frac{\Delta E_{AB}}{k_B T}\right) \quad (2.4)$$

Here, N_A and N_B are the population of energy states A and B , respectively, ΔE_{AB} is the energy difference $E_B - E_A$ between the states, k_B is the Boltzmann constant and T is the absolute temperature.

Since the intensity of emission from these states is proportional to the population of the states, the emission intensity ratio will show the same temperature dependence as show in equation 2.4. Thus, the intensity ratio I_A/I_B of emission from states A and B will behave according to²⁹:

$$\frac{I_A}{I_B} \propto C \cdot \exp\left(\frac{\Delta E_{AB}}{k_B T}\right) \quad (2.5)$$

Here, C is a constant, which is a measure for the spontaneous emission from both states, containing for both states the Planck constant h , the frequency ν , the degeneracy g and the spontaneous emission rate A :

$$C = \frac{h \cdot \nu_A \cdot g_A \cdot A_A}{h \cdot \nu_B \cdot g_B \cdot A_B} \quad (2.6)$$

As mentioned earlier, energy states A and B are thermally coupled when the energy difference is in the order of $\Delta E_{AB} \sim k_B T$. If this is the case, the thermal energy is large enough to bridge the energy gap between the energy states and, since the population redistribution happens on

a picosecond timescale, i.e. faster than the radiative and non-radiative decay,³⁰ the thermally induced emission intensity ratio is expected to be observed.

2.4 REPO₄:Ln for nanothermometry

In this work, temperature dependent luminescence of selected lanthanides will be investigated. In order to allow for high spatial resolutions, these lanthanides are incorporated in an inorganic rare earth phosphate nanoparticle host material (REPO₄).

2.4.1 Lanthanide dopants

The rich energy level scheme of lanthanides, as mentioned in section 2.1, makes the trivalent lanthanides viable candidates for application in nanothermometry. Due to the presence of a large amount of energy states, lanthanides with thermally coupled states can be selected and application of these lanthanides in nanothermometry techniques can be investigated. Of the different lanthanides, erbium, dysprosium and europium are expected to be suitable candidates for band shape luminescence nanothermometry, since all three of these elements possess two energy states that are close to each other in energy, yet relatively well separated from other, lower energy levels, i.e. the ⁴S_{3/2} and ²H_{11/2}, ⁴F_{9/2} and ⁴I_{15/2} and ⁵D₁ and ⁵D₀ energy states, respectively (as can be seen in the Dieke diagram in appendix A). Additionally, the energy difference between these states is slightly different, with erbium having the smallest energy difference and europium the largest. Therefore, they may be applicable for nanothermometry in different temperature regions.

2.4.2 REPO₄ nanoparticles

In literature, synthesis of different lanthanide phosphate nanoparticles has been reported.³¹ LnPO₄:Ln nanoparticles with a diameter in the order of a few nanometres can be synthesized with product yields in the order of a few grams. Because elements in the lanthanide series are chemically similar, doping of lanthanide phosphates with a desired luminescent lanthanide ion is expected to be relatively straight forward. In this approach, lanthanum phosphate serves as a transparent host (empty 4*f* orbitals) for the luminescent dopant ions. Additionally, the highest phonon energy for lanthanum phosphate is around $\sim 1050\text{ cm}^{-1}$, which is generally lower than that of organic ligands or complexes.²⁴ This will result in a decrease in the non-radiative multi-phonon relaxation in LaPO₄ nanoparticles and thus an increase in luminescence.

Different lanthanide phosphates have been reported to show different crystal structures, depending on the lanthanide that is used.³¹ Figure 2.4 shows X-ray diffraction patterns for different LnPO₄ nanoparticles, where Ln = any lanthanide from cerium to lutetium. Going from Ce to Lu, the X-ray diffraction patterns of the corresponding phosphate nanoparticles show a gradual transition from the monoclinic monazite phase for the lighter lanthanides, to the tetragonal xenotime phase for the heavier lanthanides. This difference is ascribed to the decreasing ionic radius of the lanthanide ions from lanthanum to lutetium, known as lanthanide contraction.

This contraction phenomenon originates from the properties of the 4*f* orbitals. As mentioned in section 2.1, the 4*f* orbitals are located closer to the nucleus with respect to the outer 5*s* and 5*p* orbitals. However, as can be seen in figure 2.1 on page 7, the 4*f* orbitals do not all distribute within the 5*s* and 5*p* orbitals. Rather, there is some overlap of the orbitals, resulting in a less effective shielding of the attractive interactions between the outer electrons and the nuclear charge. Since the nuclear charge increases with increasing atomic number, this partial shielding

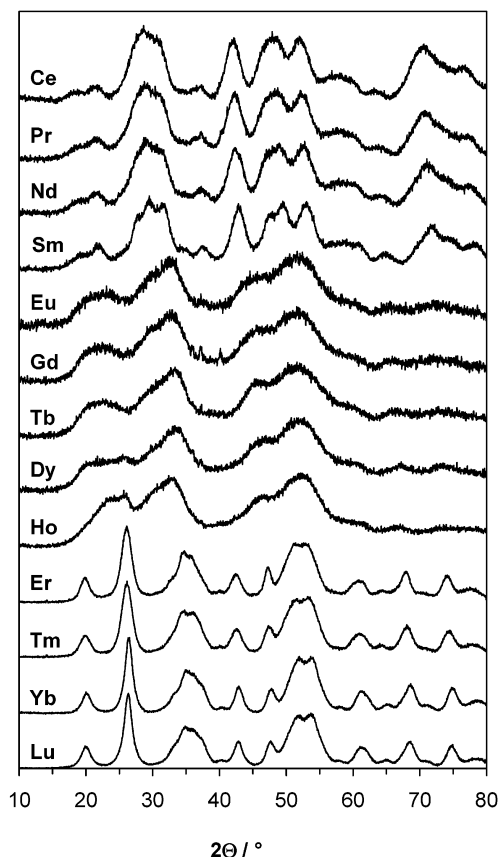


Figure 2.4: X-ray powder diffraction patterns of different LnPO_4 nanoparticles, going from CePO_4 (top) to LuPO_4 (bottom).³¹

results in an increasing attraction between the nucleus and the outer electrons, thus decreasing the ionic radius for the heavier lanthanides.¹⁶

Due to these differences in ionic radius, the LaPO_4 crystal structure may be less suitable as a host, depending on the ionic radius of lanthanide dopant. In this case, yttrium phosphate might be used as a host, since yttrium has a slightly smaller ionic radius, which is closer to the ionic radius of the heavier lanthanides. Yttrium, although officially not an element of the lanthanide series, is one of the rare earth elements, to which the lanthanides also belong. Since yttrium is expected to be chemically similar to lanthanum, the same methods are expected to be applicable for YPO_4 nanoparticle synthesis.

2.4.3 Nanoparticle coating

Due to the small particle size of rare earth phosphate nanoparticles, in the order of ~ 5 nm, a relatively large fraction of the dopant ions will be present at or near the particle surface. This can have a negative effect on the luminescence of the particles, because of energy-loss processes at the surface, due to surface defects or interactions of emitting ions in close proximity to the organic ligands at the surface, leading to non-radiative decay.³²

REPO₄ shell

One approach of overcoming this surface quenching, is by coating the doped nanoparticles with a shell of pure REPO₄. This way, the dopant ions will be farther away from the surface and thus farther away from the ligands at the surface, while the crystal structure in the vicinity of the dopant ions is preserved.^{32,33}

Similar to the discussion of different rare earth phosphate nanoparticles as host, an yttrium phosphate shell may be applied in order to prevent lattice mismatch between the core and shell materials.

Silica shell

Furthermore, the growth of a silica shell around the nanoparticles may provide better stability of the particles.

First, the separation between the emitting ions and the quenching organic ligands at the surface will increase even further after silica shell growth. Although the silica shell is expected to contain silanol (Si-OH) groups and the O-H bond typically has a high vibrational energy, the highest phonon energy in silica is reported to be in the order of 1100 cm⁻¹, which is considerably smaller than the previously mentioned 3500 cm⁻¹ for organic bonds in ligands or complexes.³⁴⁻³⁶ Instead, the highest phonon energy of silica is similar to the 1050 cm⁻¹ for LaPO₄, thus the growth of a silica shell around the nanoparticles is expected to decrease the rate of multi-phonon relaxation.

Second, the thermal stability of the particles is expected to increase after silica coating, by replacing the organic ligands on the surface of the nanoparticles. Since these organic ligands are expected to be susceptible to oxidation at elevated temperatures, replacing them with silica is expected to increase the thermal stability of the particles, making them suitable for higher temperature measurements.

Chapter 3

Methodology

An overview of the chemicals that were used, is given in appendix B on page 66. The chemicals were used without further purification, unless stated otherwise.

3.1 Synthesis

3.1.1 Microcrystalline REPO₄:Ln

Microcrystalline LaPO₄:Er,Yb was synthesized by mixing and grinding 3.5 mmol La₂O₃, 0.08 mmol Er₂O₃, 0.7 mmol Yb₂O₃ and 7 mmol (NH₄)₂HPO₄ powders and heating in a tube oven under air at ~1300 °C for three hours. The mixture was cooled down naturally and used without further purification.

Bulk YPO₄:Er,Yb was synthesized using the same method, with the La₂O₃ precursor replaced by 3.5 mmol Y₂O₃ powder.

The products were obtained as a white powder.

3.1.2 REPO₄:Ln nanoparticles

Monazite phase LaPO₄ nanoparticles were synthesized according to the following procedure.³¹

First, 10 mmol of a mixture of LnCl₃ · *x* H₂O was dissolved in 10 mL methanol by magnetic stirring, until no solid material was observed (Ln = La, Ce, Eu, Dy, Er, Yb, where the ratio of the different lanthanide precursors was equal to the desired dopant concentration). To ensure complete dissolution, the solution was placed in an ultrasonic bath for ~15 minutes. Subsequently, the solution was transferred into a reaction vial connected to a Schlenk line set-up. Then, 20 mmol of tributyl phosphate was added and the methanol was evaporated under vacuum. To this mixture, 30 mL of lukewarm diphenyl ether was added and water, released by the LaCl₃ hydrate precursor, was evaporated under vacuum at ~100 °C. The mixture was then cooled down to ~50 °C under N₂ atmosphere. When the temperature reached ~50 °C, 30 mmol of tributyl amine and 7.0 mL of a 2 M phosphoric acid in dihexyl ether solution were added through a septum. Finally, the reaction mixture was heated to 200 °C. The reaction mixture was left to react under N₂ atmosphere overnight.

After ~16 h, the reaction mixture was cooled down to room temperature. The product was washed by adding toluene as an antisolvent and centrifuging for 10 minutes at 2750 rpm. Then, the supernatant was removed. For the next washing step, the product was redispersed in toluene

again. After completing these washing steps three times, the product was dried in a vacuum desiccator overnight to obtain the product as a white powder.

Similarly, for the synthesis of YPO_4 nanoparticles, the same procedure is followed, but with the $\text{LaCl}_3 \cdot 6\text{H}_2\text{O}$ precursor replaced by $\text{YCl}_3 \cdot 6\text{H}_2\text{O}$.

$\text{LaPO}_4\text{:Ln} \cdot x\text{H}_2\text{O}$ nanoparticles

In addition to the monazite phase $\text{LnPO}_4\text{:Ln}$ synthesis method described above, rhabdophane phase $\text{LaPO}_4\text{:Dy,Ce} \cdot x\text{H}_2\text{O}$ nanoparticles were synthesized according to a modified literature procedure.³⁷

First, 0.8 mmol $\text{LaCl}_3 \cdot 6\text{H}_2\text{O}$, 0.05 mmol $\text{DyCl}_3 \cdot 6\text{H}_2\text{O}$ and 0.15 mmol $\text{CeCl}_3 \cdot 7\text{H}_2\text{O}$ were dissolved in 10 mL deionized water. Separately, 3 mmol $(\text{NaPO}_3)_n$ was dissolved in 10 mL deionized water. The solutions were mixed and heated to 90 °C under continuous magnetic stirring for three hours. The product was washed by centrifugation (10 minutes at 2750 rpm) and redispersion in deionized water three times. Finally, the product was dried in an oven at ~ 100 °C overnight and obtained as a white powder.

3.1.3 $\text{REPO}_4\text{:Ln/REPO}_4$ core-shell nanoparticles

$\text{LaPO}_4\text{:Ln/LaPO}_4$ core-shell nanoparticles were synthesized from the crude reaction product of the core synthesis (section 3.1.2), according to a similar procedure.³³ After the reaction, the product mixture of the core synthesis was cooled down and half of the crude product was removed and washed as described above. In a different vessel, the shell-precursor was prepared by dissolving 13.5 mmol of $\text{LaCl}_3 \cdot 6\text{H}_2\text{O}$ in 19 mL methanol. To this solution, 27 mmol of tributyl phosphate was added and the methanol was evaporated under vacuum. Then, 41 mL of lukewarm diphenyl ether was added and water, released by the LaCl_3 hydrate precursor, was evaporated under vacuum at ~ 100 °C. Subsequently, the mixture was cooled down to ~ 50 °C under N_2 atmosphere and 40.5 mmol of tributyl amine was added. To the crude core product, 9.0 mL of a 2 M phosphoric acid in dihexyl ether solution was added, after which the reaction mixture was heated to 200 °C. Finally, the shell-precursor mixture was added dropwise to the core product over a period of ~ 2 h. The reaction mixture was left to react under N_2 atmosphere overnight. The product was washed and dried the following day as described in section 3.1.2, to obtain the product as a white powder.

For the synthesis of $\text{YPO}_4\text{:Ln/YPO}_4$ core-shell nanoparticles, the same procedure is followed, but with the $\text{LaCl}_3 \cdot 6\text{H}_2\text{O}$ precursor replaced by $\text{YCl}_3 \cdot 6\text{H}_2\text{O}$.

Aqueous YPO_4 coating method

In addition to the direct $\text{REPO}_4\text{:Ln/REPO}_4$ core-shell synthesis, an aqueous YPO_4 coating method was performed on purified $\text{YPO}_4\text{:Er,Yb}$ nanoparticles, according to the following procedure.³⁸

First, 0.0320 g of $\text{YPO}_4\text{:Er,Yb}$ nanoparticles were redispersed in 75 mL deionized water. Under vigorous magnetic stirring, 2.65 mL of a 0.15 M $\text{Y}(\text{NO}_3)_3 \cdot 6\text{H}_2\text{O}$ solution in deionized water and 2.65 mL of a 0.15 M $(\text{NH}_4)_2\text{HPO}_4$ solution in deionized water were added. The mixture was stirred for 30 minutes, after which the pH of the mixture was adjusted to pH = 8 by adding ammonia under magnetic stirring. The resulting mixture was transferred into a stainless steel autoclave and sealed. The autoclave was heated to 200 °C for ~ 16 hours and cooled naturally to room temperature. The product was collected by centrifugation and washed three times with deionized water, after which it was dried in an oven at ~ 100 °C overnight. The product was obtained as a white powder.

3.1.4 Silica coating

$\text{REPO}_4\text{:Ln}$ and $\text{REPO}_4\text{:Ln/REPO}_4$ nanoparticles were coated with a silica layer in a reverse micelle method, according to the following procedure.³⁹

First, the coating was performed in a series of five batches, with increasing concentration of nanoparticles per coating batch. This way, the optimal concentration for silica coating was determined and used for a larger scale coating of the nanoparticles. The different amounts of nanoparticles used in the series are listed in table 3.1 in the column marked "NPs (nmol)".

The estimation of the amount of nanoparticles was performed by analyzing TEM images of the nanoparticles. The average diameter of the particles was determined and, by assuming spherical particles and using the density and unit cell volume of the material, the average mass of a single nanoparticle was estimated. The mass of the ligands was neglected.

Using this estimation, a stock dispersion of 250 nmol nanoparticles in 15 mL methanol was prepared.

Batch	Stock (μL)	NPs (nmol)
1	30	0.5
2	60	1
3	90	1.5
4	120	2
5	240	4

Table 3.1: Concentrations of nanoparticles used in silica coating

For each of the five batches in the series, 1.3 mL of NP-5 was dispersed in 10 mL hexane and magnetically stirred for 15 minutes. Then, the amount of stock nanoparticle dispersion in table 3.1 was added to each batch. Subsequently, 80 μL tetraethyl orthosilicate (TEOS) and 150 μL ammonia (28 wt% in water) were added to each batch. In between each addition step, the reaction mixture was stirred for 15 minutes. After the addition of all reagents, the reaction mixture was stirred for one minute and left to react at room temperature overnight.

After ~ 20 hours, the products were washed by adding 3 mL ethanol to each batch and centrifuging for 10 minutes at 2750 rpm. The supernatants were removed and the remaining products were separately redispersed in 10 mL ethanol and centrifuged for 20 minutes at 2750 rpm. This was repeated once more (again doubling the centrifugation time to 40 minutes) and finally, the products were redispersed in 3 mL ethanol.

After determining the optimal nanoparticle concentration in the silica coating, the reaction was scaled up by increasing the amounts of all reactants by a factor of five, in order to obtain more product for further analysis. Here, instead of redispersing in ethanol, the product was dried under vacuum overnight and obtained as a white powder.

3.2 Characterization

The characterization of the products consisted of two parts, i.e. structural characterization and luminescence investigation. First, the products of the reactions were analyzed with X-ray diffraction and transmission electron microscopy to check if the synthesis was successful. Second, the photoluminescence properties were measured.

3.2.1 X-ray diffraction

X-ray diffractograms of the product powders were recorded on Philips PW1729 X-ray diffractometer, using copper K_α radiation ($\lambda = 0.15418$ nm). All diffractograms were recorded over the angular range $10^\circ \leq 2\theta \leq 70^\circ$, with a step size of $\Delta 2\theta = 0.01^\circ$, unless stated otherwise. The recorded diffractograms were compared to literature reference diffractograms, to check the phase purity of the products.

3.2.2 Transmission electron microscopy

Transmission electron microscopy images were obtained on a Philips TECNAI10 transmission electron microscope. TEM samples were prepared by drying drops of diluted particle dispersions in ethanol or methanol on polymer coated copper grids.

Size analysis of the particles was done in analySIS iTEM software. For all size determinations, a total of 50 particles were measured. Since the particles were not perfectly spherical, the diameter was measured in two perpendicular directions for all particles, to obtain an average diameter of the particles.

3.2.3 Photoluminescence

Emission and excitation

Room temperature emission and excitation measurements of the product powders were performed on an Edinburgh Instruments FLS920 fluorescence spectrometer equipped with a 450 W xenon lamp and a Hamamatsu R928 photomultiplier tube with a grating blazed at 500 nm.

Temperature dependent emission

Temperature dependent emission measurements of the product powders were performed on the same equipment as room temperature emission and excitation measurements, with the addition of a Linkam Cell THMS600 heating stage in the place of the normal sample holder to control the temperature.

Time-resolved photoluminescence

Time-resolved photoluminescence measurements of the product powders were performed on the same equipment as regular emission and excitation measurements, with the addition of an Oportek HE 355 II optical parametric oscillator system tuned to a wavelength of 453 nm, to excite the samples.

Chapter 4

Results & discussion

This chapter describes the different materials that were synthesized in this project:

- Dysprosium/cerium-doped LaPO_4 Section 4.1 on page 22
- $\text{LaPO}_4\text{:Dy,Ce}$ nanoparticles on gold nanoparticles Section 4.2 on page 41
- Europium-doped LaPO_4 Section 4.3 on page 43
- Erbium-ytterbium co-doped LaPO_4 Section 4.4 on page 50
- Erbium-ytterbium co-doped YPO_4 Section 4.5 on page 54

The characterization consisted of structural analysis using TEM and XRD techniques, followed by luminescence measurements.

4.1 $\text{LaPO}_4\text{:Dy,Ce}$

To study dysprosium luminescence in a crystalline LaPO_4 host, different dysprosium-doped materials were synthesized. These materials include:

- $\text{LaPO}_4\text{:Dy}$ core nanoparticles Section 4.1.1 on page 22
- $\text{LaPO}_4\text{:Dy,Ce}$ core nanoparticles Section 4.1.2 on page 25
- $\text{LaPO}_4\text{:Dy,Ce/LaPO}_4$ core-shell nanoparticles Section 4.1.3 on page 28
- $\text{LaPO}_4\text{:Dy,Ce/LaPO}_4\text{/Si}$ core-shell-shell nanoparticles Section 4.1.4 on page 32

4.1.1 $\text{LaPO}_4\text{:Dy}$ nanoparticles

First, monazite-phase LaPO_4 nanoparticles doped with 5 mol% dysprosium were synthesized.

Figure 4.1a shows the X-ray diffractogram of the product. Since the XRD analysis of this sample was only used as a quick check for the crystal structure, the diffractogram was measured in steps of $\Delta 2\theta = 0.1^\circ$ to decrease the measuring time (as opposed to the $\Delta 2\theta = 0.01^\circ$ for the standard XRD measurements). The diffractogram corresponds well with a literature reference for the monoclinic monazite-phase known for bulk LaPO_4 (JCPDS No. 01-084-0600, shown in green). As can clearly be seen in the diffractogram, the peaks that originate from the LaPO_4

crystal are relatively broad and show a low signal-to-noise ratio. This is due to the nanocrystalline size of the particles. The same observation is made in the literature for nanocrystalline LaPO_4 particles.^{33,40} The peaks around $2\theta = 38^\circ$, 45° and 65° are caused by the aluminium sample holder (reference for aluminium shown in blue).

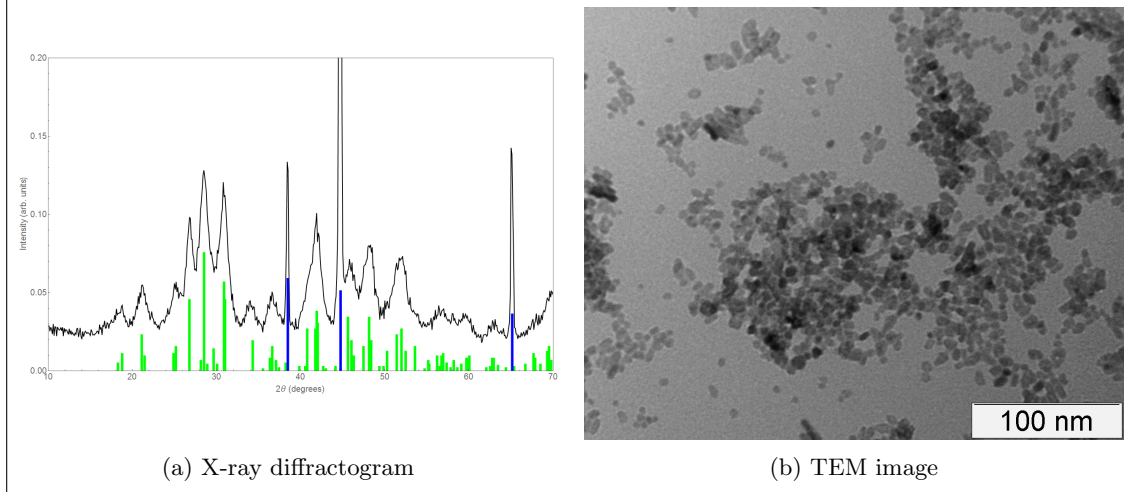


Figure 4.1: X-ray diffractogram (4.1a) and TEM image (4.1b) of the $\text{LaPO}_4\text{:Dy}$ product.

From the XRD data, the crystallite size d can be calculated, using the Scherrer equation⁴¹:

$$d = \frac{2\sqrt{\frac{\ln 2}{\pi}} \cdot \lambda}{\Delta(2\theta) \cdot \cos \theta} \quad (4.1)$$

Here, d is the mean crystallite size in nm, λ is the wavelength of the incident X-ray radiation (0.15418 nm in the case of Cu K_α radiation), $\Delta(2\theta)$ is the full width at half maximum of the peak in radians and θ is the Bragg angle in degrees.

It is important to note, that the evaluation of the Scherrer equation provides an approximation of the mean crystallite size. Various factors, other than the crystallite size, can influence the peak broadening and thus the calculated mean crystallite size, such as crystal lattice imperfections and lattice stress.⁴² Furthermore, the particles of interest might consist of multiple crystallite domains, which means that the evaluation of the Scherrer equation only provides an estimation of the lower bound of the particle size.

Since the peak around $2\theta = 42^\circ$ in the diffractogram is relatively well isolated, the Scherrer equation was evaluated on this peak for $\text{LaPO}_4\text{:Dy}$ nanoparticles. This resulted in an average crystallite size of $d = 4.33$ nm, thus indicating the nanocrystalline size of the product.

Figure 4.1b shows a TEM image of the product. This image further confirms the nanocrystalline size of the particles. Size analysis in analySIS iTEM software yielded an average particle diameter of 5.3 ± 1.2 nm, in the same order of magnitude as the mean crystallite size obtained from the peak broadening in XRD. This indicates that the product consists of monocrystalline nanoparticles. In the image, some agglomeration of the particles is observed. However, single isolated particles are also observed. The agglomeration can be attributed to drying effects of the particle dispersion onto the TEM grids.

The trends in peak broadening and low signal-to-noise ratios in the XRD patterns, due to the small size of the particles, as well as the agglomeration of the particles on the TEM grids,

hold for all products discussed in this chapter, unless stated otherwise.

From the TEM data, it is confirmed that nanocrystalline particles are formed. The XRD analysis further confirms the monoclinic monazite crystal structure of the particles. Therefore, it is concluded that the synthesis successfully yields monazite-phase LaPO_4 nanoparticles.

In order to check the presence of luminescent dysprosium dopant ions, excitation and emission spectra of the product were measured. Figure 4.2 shows the excitation and emission spectra of the $\text{LaPO}_4:\text{Dy}$ nanoparticles. The excitation spectrum (4.2a) was recorded with an emission wavelength of 573 nm. The emission spectrum (4.2b) was recorded with an excitation wavelength of 349 nm.

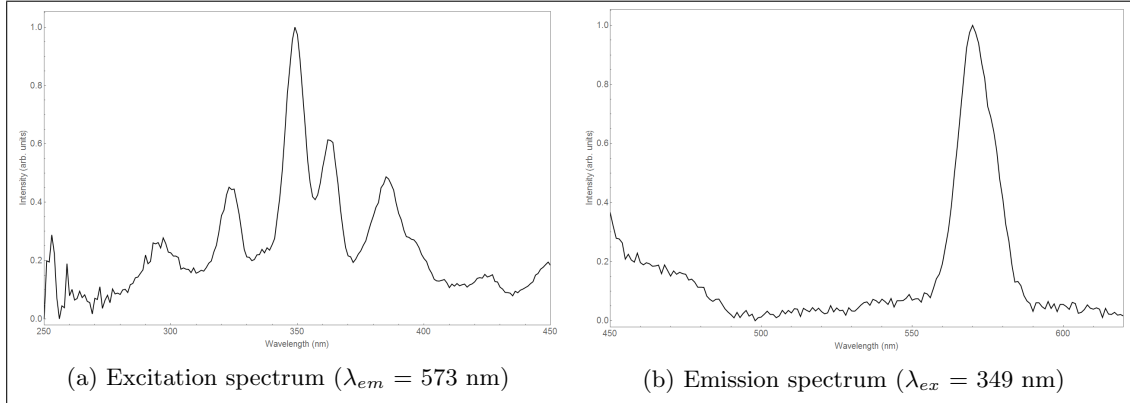


Figure 4.2: Excitation spectrum (4.2a) and emission spectrum (4.2b) of the $\text{LaPO}_4:\text{Dy}$ product.

In the excitation spectrum, peaks around $\lambda = 300$ nm, 325 nm, 350 nm, 365 nm, 385 nm, 425 nm and 450 nm are observed, with the peak around $\lambda = 350$ nm having the highest intensity. This corresponds with excitation spectra of different dysprosium-doped systems reported in literature, such as $\text{LaAlGe}_2\text{O}_7:\text{Dy}$ ⁴³, $\text{Zn}(\text{BO}_2)_2:\text{Dy}$ ⁴⁴ and $\text{KLa}(\text{PO}_3)_4:\text{Dy}$ ⁴⁵. These peaks are attributed to high energy $4f - 4f$ transitions of dysprosium. As can be seen in the Dieke diagram (Appendix A on page 65), a multitude of different $4f$ energy levels at high energies (between $26 \cdot 10^3 \text{ cm}^{-1}$ and $36 \cdot 10^3 \text{ cm}^{-1}$) is present in trivalent dysprosium, such that different transitions between energy levels can have the same energy. For this reason, it can be difficult to accurately attribute some emission peaks to the corresponding electronic transition in trivalent dysprosium. An overview of the different excitation peaks and their proposed corresponding transition from different reports is listed in table 4.1.

An accurate analysis of the different excitation transitions is beyond the scope of this project. However, the good agreement between the measured excitation spectrum and reported excitation spectra for different dysprosium-doped materials, indicates that dysprosium ions were successfully incorporated into the LaPO_4 host lattice.

Table 4.1: Overview of excitation transitions observed in $\text{LaPO}_4:\text{Dy}$ ($\lambda_{em} = 573$ nm).

Peak position (nm)	300	325	350	365	385	425	450
Dy³⁺ transition⁴³	⁴ K _{13/2}	⁴ K _{15/2}	⁶ P _{7/2}	⁴ I _{11/2}	⁴ M _{21/2}	⁴ G _{11/2}	⁴ I _{15/2}
Dy³⁺ transition⁴⁴	⁴ D _{7/2}	⁶ P _{3/2}	⁶ P _{7/2}	⁶ P _{5/2}	⁴ M _{21/2}	⁴ G _{11/2}	⁴ I _{15/2}
Dy³⁺ transition⁴⁵	⁴ H _{11/2}	⁴ M _{17/2}	⁶ P _{7/2}	⁶ P _{5/2}	⁴ K _{17/2}	-	⁴ I _{15/2}

In the emission spectrum, a peak around $\lambda = 570$ nm is observed, which corresponds well with

the ${}^4F_{9/2} \rightarrow {}^6H_{13/2}$ transition for dysprosium. On the basis of the Dieke diagram (Appendix A on page 65), another peak around $\lambda = 480$ nm can also be expected, corresponding with the ${}^4F_{9/2} \rightarrow {}^6H_{15/2}$ transition for dysprosium. However, a clear emission peak can not be distinguished in the emission spectrum. There is an increase in intensity going from $\lambda = 490$ nm to $\lambda = 450$ nm, that remains low in intensity compared to the peak around $\lambda = 570$ nm. This increase might be attributed to a filter effect, which can occur if the cut-off wavelength of the filter and the measured emission wavelengths are not separated well enough. This makes it difficult to distinguish an emission peak.

The observations mentioned above indicate, that the product consists of monocrystalline nanoparticles, with an average diameter of around 5 nm. Furthermore, dysprosium was successfully incorporated in the nanocrystals. However, the signal-to-noise ratio is very low and the emission intensity is not sufficiently high to be observed by eye, after UV excitation.

4.1.2 $\text{LaPO}_4\text{:Dy,Ce}$ nanoparticles

In an attempt to obtain higher intensity dysprosium emission, by increasing the absorption with a sensitizer ion, dysprosium-doped LaPO_4 nanoparticles co-doped with a cerium sensitizer, were synthesized (5 mol% and 15 mol% of Dy and Ce, respectively).

Figure 4.3a shows the X-ray diffractogram of the product. The peaks in the diffractogram show the expected broadening and correspond well with literature references for monoclinic monazite-phase LaPO_4 (JCPDS No. 01-084-0600, shown in green) and aluminium (shown in blue). Using the Scherrer equation (4.1) and the peak around $2\theta = 42^\circ$, an average crystallite size of 5.49 nm was calculated for the product.

Figure 4.3b shows a TEM image of the product. This image confirms the nanocrystalline size of $\sim 5.7 \pm 1.2$ nm of the particles and corresponds well with the calculated crystallite size from the XRD data.

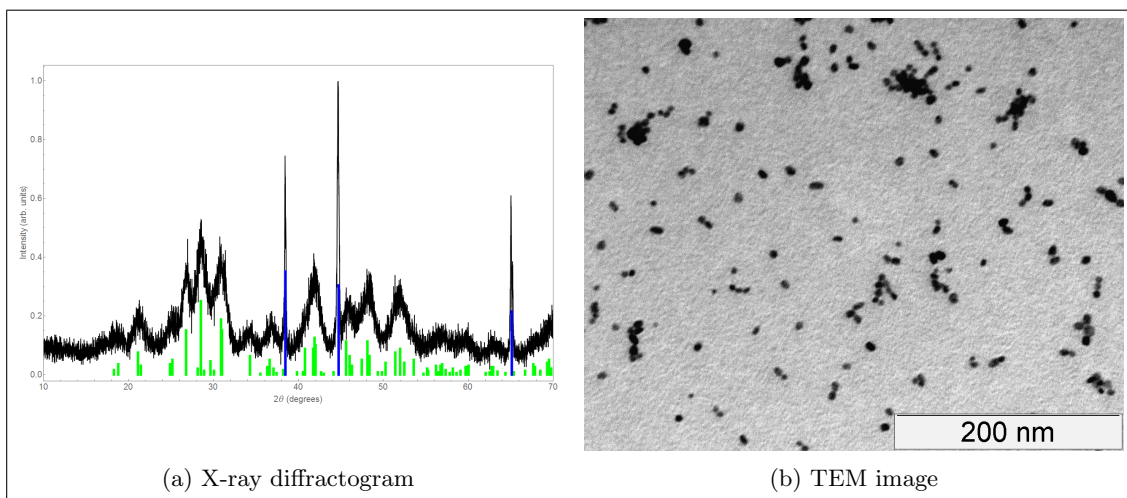


Figure 4.3: X-ray diffractogram (4.3a) and TEM image (4.3b) of the $\text{LaPO}_4\text{:Dy,Ce}$ product.

Figure 4.4 shows the excitation and emission spectra of $\text{LaPO}_4\text{:Dy,Ce}$ nanoparticles. The excitation spectrum (4.4a) was recorded with an emission wavelength of 571 nm. The emission spectrum (4.4b) was recorded with an excitation wavelength of 285 nm.

In the excitation spectrum, peaks around $\lambda = 325$ nm, 350 nm, 365 nm, 385 nm and 450 nm are observed, of which the peak around $\lambda = 350$ nm has the highest intensity. These peaks

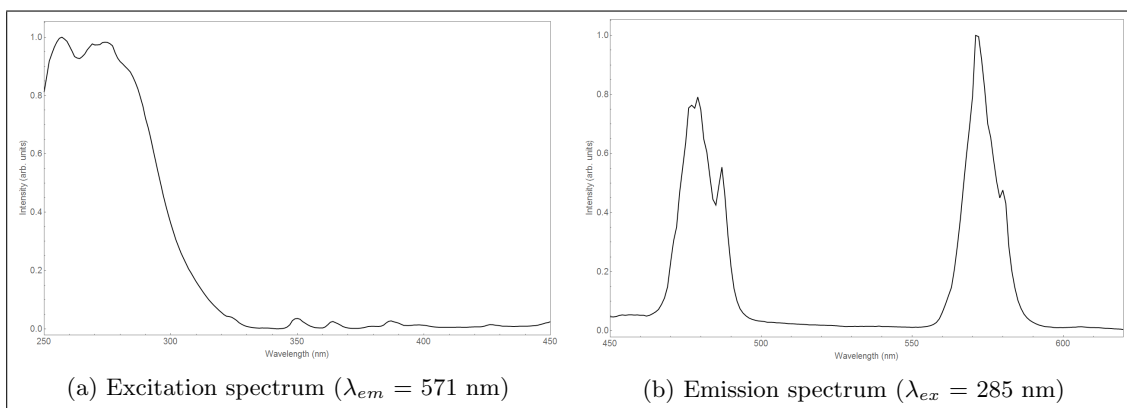


Figure 4.4: Excitation spectrum (4.4a) and emission spectrum (4.4b) of the $\text{LaPO}_4:\text{Dy,Ce}$ product.

are attributed to the direct excitation of dysprosium ($4f - 4f$ transitions), as was the case for $\text{LaPO}_4:\text{Dy}$ in section 4.1.1 on page 22. Additional to these peaks, a large band around $\lambda = 280$ nm is observed in the excitation spectrum, that was not observed for $\text{LaPO}_4:\text{Dy}$. This band is attributed to a $4f - 5d$ transition in cerium.^{46,47} The relative intensity of the band around $\lambda = 280$ nm is much higher than the direct dysprosium excitation peaks, which can be attributed to the nature of this transition. Since $4f - 5d$ transitions are parity allowed, they have a larger oscillation strength than the $4f - 4f$ transitions, thus leading to more absorption. The presence of this excitation band in the excitation spectrum leads to the conclusion, that the cerium ions can efficiently absorb light and transfer the energy to the dysprosium ions. The broadening of the peak corresponds well with the expected broadening for $4f - 5d$ transitions.

In the emission spectrum, a peak around $\lambda = 570$ nm, corresponding with the ${}^4\text{F}_{9/2} \rightarrow {}^6\text{H}_{13/2}$ transition for dysprosium, is observed, as was the case for $\text{LaPO}_4:\text{Dy}$. Additionally, a peak around $\lambda = 480$ nm is observed. This peak corresponds well with the ${}^4\text{F}_{9/2} \rightarrow {}^6\text{H}_{15/2}$ transition for dysprosium. Since the dysprosium-cerium co-doped LaPO_4 nanoparticles can be excited at lower wavelength compared to the dysprosium-doped nanoparticles ($\lambda_{ex} = 285$ nm vs. $\lambda_{ex} = 349$ nm, respectively), a filter with a cut-off wavelength that is further away from the measured emission wavelengths can be used, thereby reducing potential filter effects in the emission spectrum. This can explain the absence of an emission peak around $\lambda = 480$ nm in the emission spectrum of $\text{LaPO}_4:\text{Dy}$, as discussed in section 4.1.1 on page 22.

These observations indicate, that dysprosium and cerium were successfully incorporated in the nanocrystalline LaPO_4 particles. Furthermore, the expected energy transfer from cerium to dysprosium is observed in the luminescence spectra and co-doping of cerium leads to more intense dysprosium emission, compared to the purely dysprosium-doped nanocrystals (*ca.* 40-fold increase under the same measuring conditions).

$\text{LaPO}_4:\text{Dy,Ce} \cdot x \text{H}_2\text{O}$ nanoparticles

In addition to the monoclinic monazite-phase $\text{LaPO}_4:\text{Dy,Ce}$ nanoparticles, rhabdophane-phase $\text{LaPO}_4:\text{Dy,Ce} \cdot x \text{H}_2\text{O}$ nanoparticles were synthesized.

Figure 4.5a shows the X-ray diffractogram of the product. The peaks in the diffractogram show the expected broadening and correspond well with literature references for rhabdophane-phase $\text{LaPO}_4 \cdot 0.5 \text{H}_2\text{O}$ (JCPDS No. 00-046-1439, shown in green) and aluminium (shown in blue). Using the Scherrer equation (4.1) and the peak around $2\theta = 42^\circ$, an average crystallite

size of 7.13 nm was calculated for the product.

Figure 4.5b shows a TEM image of the product. The TEM image clearly shows impurities and highly polydisperse particles. Since it is difficult to accurately separate the $\text{LaPO}_4\text{:Dy,Ce} \cdot x \text{H}_2\text{O}$ nanoparticles from possible impurities in the TEM images, a size analysis from TEM data was not performed.

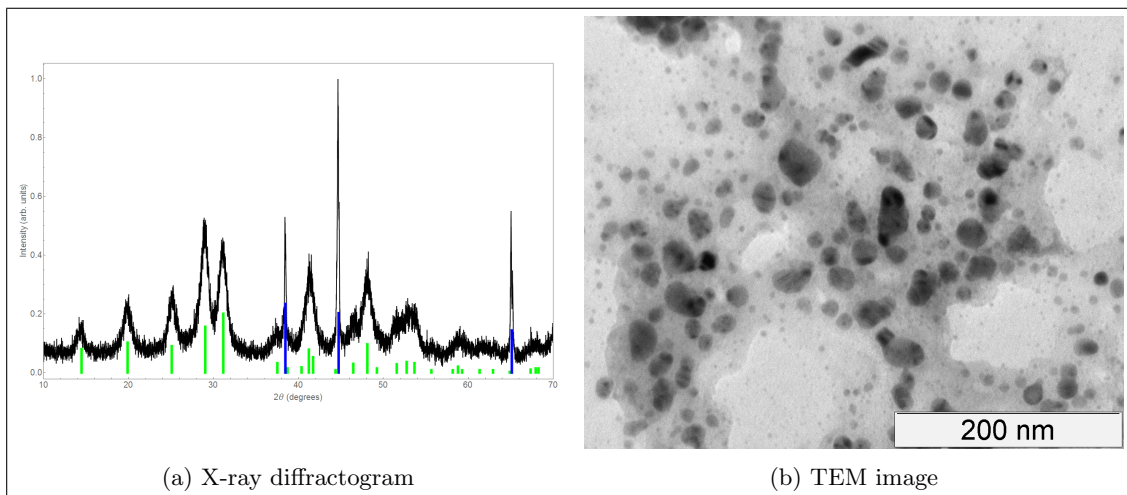


Figure 4.5: X-ray diffractogram (4.5a) and TEM image (4.5b) of the rhabdophane-phase $\text{LaPO}_4\text{:Dy,Ce}$ product.

Figure 4.6 shows the excitation and emission spectra of rhabdophane-phase $\text{LaPO}_4\text{:Dy,Ce}$ particles. The excitation spectrum (4.6a) was recorded with an emission wavelength of 571 nm. The emission spectrum (4.6b) was recorded with an excitation wavelength of 285 nm.

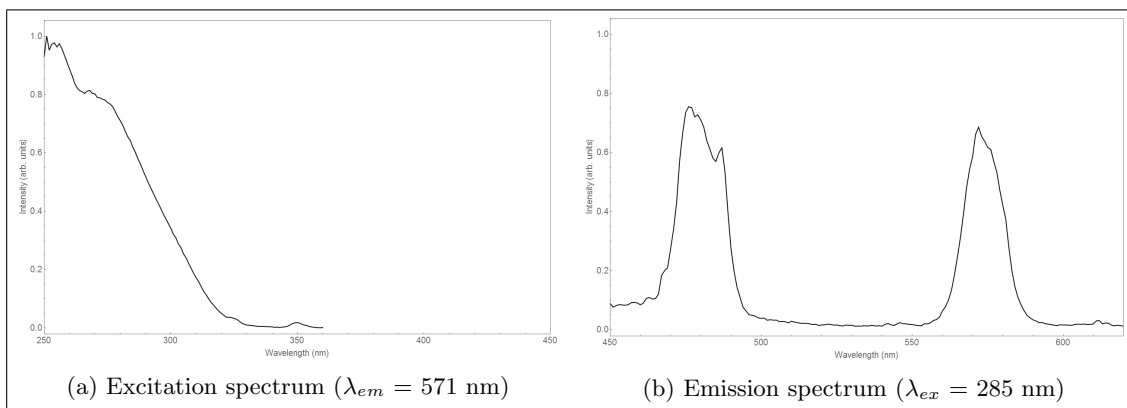


Figure 4.6: Excitation spectrum (4.6a) and emission spectrum (4.6b) of the rhabdophane-phase $\text{LaPO}_4\text{:Dy,Ce}$ product.

In the excitation spectrum, the large band around $\lambda = 280$ nm, caused by the cerium absorption, is observed. However, it is less well defined than was the case for monazite-phase $\text{LaPO}_4\text{:Dy,Ce}$. This may be attributed to the polydisperse nature of the particles, as observed in the TEM images.

In the emission spectrum, the peaks around $\lambda = 480$ nm and 570 nm from dysprosium emission are observed.

These observations indicate that it is possible to obtain dysprosium emission in this system. However, the incorporation of dysprosium and cerium ions into the LaPO_4 nanocrystals could not be confirmed from the XRD and TEM data. Furthermore, TEM analysis clearly showed that this synthesis yields nanocrystals of poor quality. For further experiments, such as the attachment of these particles onto the surface of gold nanoparticles (details in section 4.2 on page 41), high quality nanocrystals are desired. Therefore, the rhabdophane-phase $\text{LaPO}_4\text{:Dy,Ce} \cdot x \text{H}_2\text{O}$ nanoparticles were not studied further.

4.1.3 $\text{LaPO}_4\text{:Dy,Ce/LaPO}_4$ nanoparticles

In order to decrease the non-radiative decay pathways from the dysprosium ions to the surrounding ligands or solvent, $\text{LaPO}_4\text{:Dy,Ce/LaPO}_4$ core-shell nanoparticles were synthesized. Since a decrease in non-radiative decay can ensure an increase in emission intensity, this approach is expected to obtain higher intensity dysprosium emission from the dysprosium-cerium co-doped LaPO_4 nanoparticles.

Figure 4.7a (top) shows the X-ray diffractogram of the product. The peaks in the diffractogram show the expected broadening and correspond well with literature references for monazite-phase LaPO_4 (JCPDS No. 01-084-0600, shown in green) and aluminium (shown in blue). Furthermore, compared to the X-ray diffractogram of LaPO_4 core particles (figure 4.7a, bottom), the peaks are slightly sharper. This indicates that the shell growth was successful, since the increase of particle size due to the addition of a shell is expected to reduce the peak broadening. This is further confirmed by evaluation of the Scherrer equation for the peak around $2\theta = 42^\circ$, obtaining an average crystallite size of 6.98 nm (versus 5.49 for the core particles).

Figure 4.7b shows a TEM image of the product. This image confirms the nanocrystalline size of $\sim 10.5 \pm 2.9$ nm of the particles., although this is slightly larger than the average crystallite size obtained from the XRD data. The difference herein might originate from some aggregation of the particles, which influences the average size that is obtained from analyzing the TEM data but not the XRD data, since a cluster is not expected to be monocrystalline. The increase of the average diameter compared to the core particles, in both XRD and TEM analysis, indicates that the shell growth was successful.

Figure 4.8 shows the excitation and emission spectra of $\text{LaPO}_4\text{:Dy,Ce/LaPO}_4$ core-shell nanoparticles. The excitation spectrum (4.8a) was recorded with an emission wavelength of 571 nm. The emission spectrum (4.8b) was recorded with an excitation wavelength of 285 nm.

The excitation and emission spectra for $\text{LaPO}_4\text{:Dy,Ce/LaPO}_4$ core-shells show the same features as the cores, indicating that the core particles remain intact after shell growth. The intensity of the dysprosium emission in core-shell particles is slightly lower than for the core particles, but in the same order of magnitude under the same measuring conditions ($I_{570 \text{ nm}} = 335\,952$ counts versus $I_{570 \text{ nm}} = 393\,105$ counts, respectively). However, the slightly lower emission intensity can be explained by the fact, that the core-shell particles contain more non-emitting material, i.e. the pure LaPO_4 shell. Since all luminescence measurements were performed with approximately the same amount of product, the absolute amount of emitting centres in the sample is lower for core-shell particles, thus leading to a lower emission signal. For this reason, the emission intensity of core and core-shell particles can not be compared accurately from just the emission spectra.

A rough estimate of the difference in emitting material per volume can be made, assuming spherical, single-crystalline nanoparticles and using the calculated crystallite size from the XRD data of the core and core-shell nanoparticles. This way, the volume of the core-shell particles

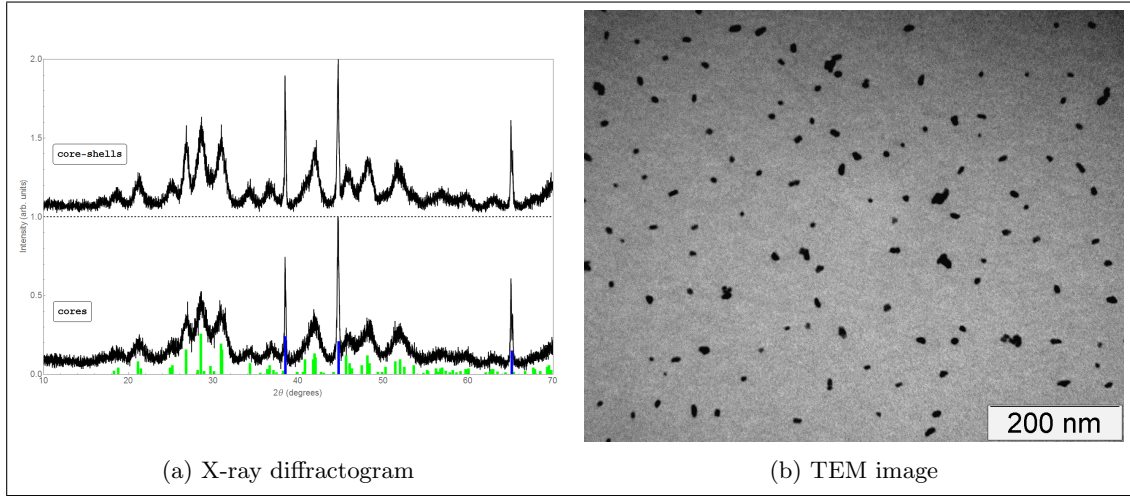


Figure 4.7: X-ray diffractogram (4.7a) and TEM image (4.7b) of the $\text{LaPO}_4:\text{Dy,Ce}/\text{LaPO}_4$ product.

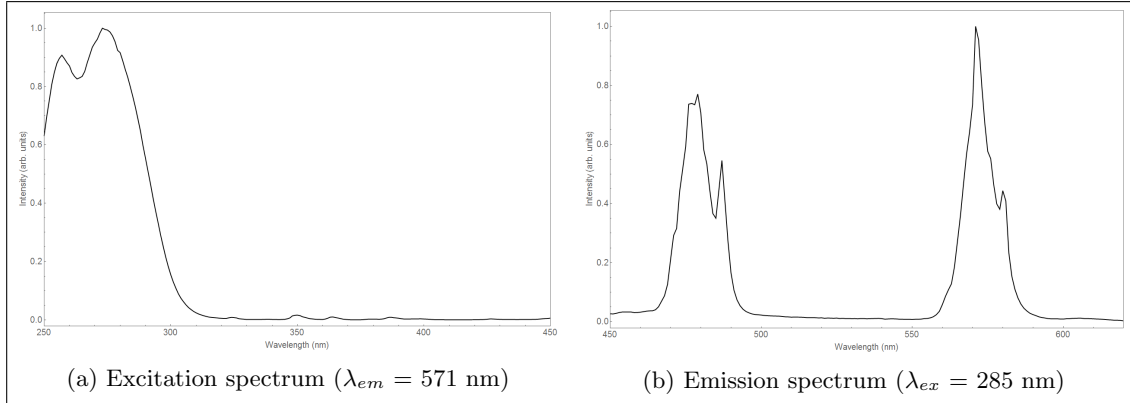


Figure 4.8: Excitation spectrum (4.8a) and emission spectrum (4.8b) of the $\text{LaPO}_4:\text{Dy,Ce}/\text{LaPO}_4$ product.

was estimated to be approximately double that of the core particles ($\sim 178 \text{ nm}^3$ versus $\sim 87 \text{ nm}^3$, respectively). Assuming that the cores are similar for both types of particles, this means that a given volume of core-shell particles will contain about half the amount of emitting centres compared to the same volume of the core particles.

As mentioned above, the dysprosium emission intensity of the core-shell particles is slightly lower, $\sim 85 \%$ of the emission intensity in core particles, whereas the difference in emitting centres is estimated to be $\sim 50 \%$. Although this is a rough estimate, these numbers indicate that the dysprosium emission intensity per particle is higher for $\text{LaPO}_4:\text{Dy,Ce}/\text{LaPO}_4$ core-shell nanoparticles, leading to the conclusion that the addition of a LaPO_4 shell does decrease the availability of non-radiative decay pathways and increases the emission intensity.

Time-resolved photoluminescence measurements

In order to further study the influence of the pure LaPO_4 shell growth on dysprosium emission in $\text{LaPO}_4:\text{Dy,Ce}$ nanoparticles, time-resolved photoluminescence measurements were performed.

Figure 4.9 shows the luminescence decay curves for the core (4.9a) and core-shell (4.9b) particles. The emission was measured at $\lambda = 573$ nm, after excitation at $\lambda = 453$ nm. This excitation wavelength is different to the usual $\lambda_{ex} = 285$ nm, because a tunable laser excitation source was used for the measurements, which had a lower wavelength limit of ~ 400 nm. This way, the sample could not be excited via cerium excitation at $\lambda = 285$ nm. Additionally, if the sample were to be excited via cerium at $\lambda_{ex} = 285$ nm, the adsorbed energy first has to be transferred to the dysprosium ions before being emitted, which would result in an additional rise time, in combination with the measured decay of the dysprosium emission, thereby complicating the interpretation of the decay curves. Instead, the sample was excited directly at $\lambda = 453$ nm, at which the highest intensity excitation peak for dysprosium above 400 nm was observed in the excitation spectra as discussed in sections 4.1.2 and 4.1.3 on pages 25 and 28, respectively.

The curves obtained this way were fitted with a double exponential fit (shown as a red line through the data) in the form of:

$$I_t = I_1 e^{\frac{-t}{\tau_1}} + I_2 e^{\frac{-t}{\tau_2}} + B \quad (4.2)$$

Here, I_t is the intensity at time t , I_1 and I_2 are intensities at different times, with τ_1 and τ_2 the corresponding lifetimes. Since accurate fits of the full curves were not obtained, the curves were fitted starting from $t = 1$ ms. The fit residuals for the obtained fits are shown in the insets of figures 4.9a and 4.9b. From these fits, values for τ_1 and τ_2 were extracted. Since the different lifetimes typically come from different decay mechanisms, of which the physical origin is not known, average lifetimes were calculated. The average lifetime is defined as^{48,49}

$$\tau_{avg} = \frac{I_1 \tau_1^2 + I_2 \tau_2^2}{I_1 \tau_1 + I_2 \tau_2} \quad (4.3)$$

Using the data from the fits and equations 4.2 and 4.3, an indication of the lifetimes for the two samples was obtained.

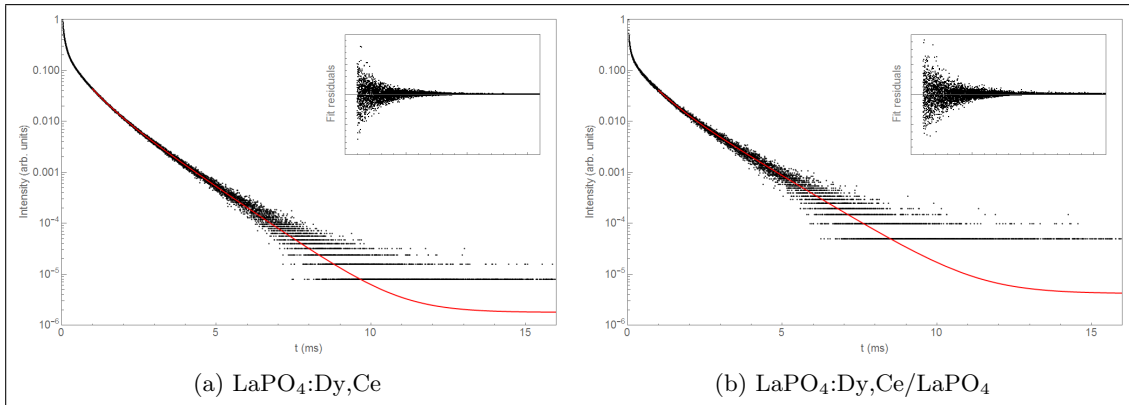


Figure 4.9: Luminescence decay curves of $\text{LaPO}_4:\text{Dy,Ce}$ core (4.9a) and core-shell (4.9b) nanoparticles.

In figure 4.9, it can be seen that the fits reproduce the data well. The fit residuals show a symmetric behaviour. From the fits and equations 4.2 and 4.3, average lifetimes of the core particles and core-shell particles were found to be $\tau_{avg,c} = 0.734$ ms and $\tau_{avg,c-s} = 0.869$ ms, respectively. The order of magnitude for the calculated lifetimes corresponds well with reported lifetimes of dysprosium-doped nanoparticles⁵⁰ and other lanthanide-doped LnPO_4 materials^{51,52}. Furthermore, the increase of τ_{avg} after LaPO_4 shell growth is a good indication, that the LaPO_4 shell provides shielding from the environment for the emitting centres in the core-shell particles, thereby reducing non-radiative decay and providing better luminescence properties.

Temperature dependent emission

In order to study temperature dependent dysprosium emission in $\text{LaPO}_4:\text{Dy,Ce}/\text{LaPO}_4$ nanoparticles, emission spectra were recorded at different temperatures, ranging from room temperature up to 250 °C, in steps of $\Delta T = 50$ °C.

Figure 4.10 shows the emission spectra at different temperatures (4.10a) and the logarithm of the intensity ratios plotted against the inverse of the temperature (4.10b). The emission spectra were recorded with an excitation wavelength of 285 nm and are colour coded in a range from yellow (for $T = 22$ °C) to red (for $T = 250$ °C). All spectra are normalized at the highest peak (around $\lambda = 570$ nm) and the emission spectra at temperatures from room temperature up to 250 °C are shown.

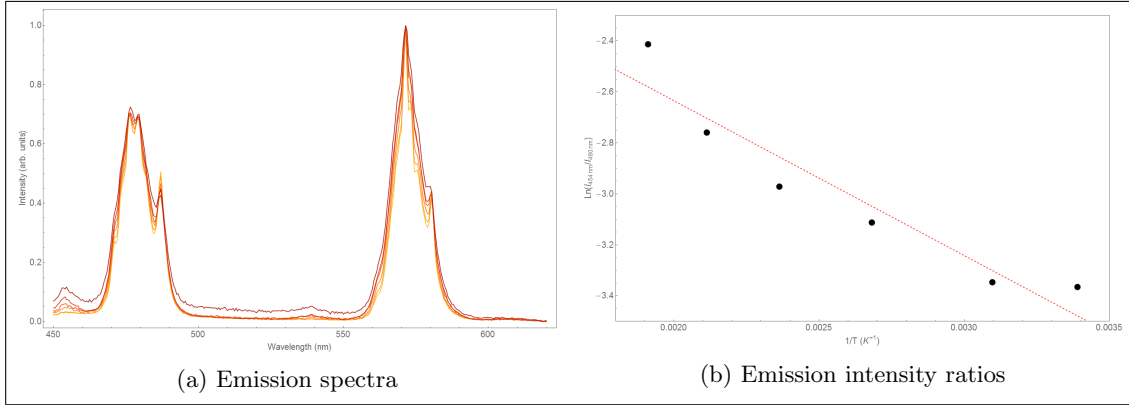


Figure 4.10: Emission spectra (4.10a) and intensity ratios (4.10b) of $\text{LaPO}_4:\text{Dy,Ce}/\text{LaPO}_4$ core-shell nanoparticles at different temperatures.

In the emission spectra, peaks around $\lambda = 480$ nm and 570 nm are observed, corresponding with the $^4\text{F}_{9/2} \rightarrow ^6\text{H}_{15/2}$ and $^4\text{F}_{9/2} \rightarrow ^6\text{H}_{13/2}$ transitions for dysprosium, respectively. Additionally, as the temperature is increased, a small peak around $\lambda = 455$ nm is observed. This peak corresponds well with the $^4\text{I}_{15/2} \rightarrow ^6\text{H}_{15/2}$ transition. Since the $^4\text{I}_{15/2}$ and $^4\text{F}_{9/2}$ levels are expected to be thermally coupled, the peaks around $\lambda = 455$ nm and 480 nm are the peaks of interest in the temperature dependent emission spectra.

When the temperature is increased above 250 °C, the luminescence signal decreases rapidly and at $T = 300$ °C, the luminescence is almost completely quenched. At room temperature, $I_{max} = 27943$ counts whereas at 300 °C, $I_{max} = 1509$ counts, which is only $\sim 5\%$ of the intensity at room temperature.

The decrease in emission intensity as the temperature is increased, can generally be attributed to thermal quenching. However, after the sample was cooled down, the emission intensity at room temperature was in the same order of magnitude as at $T = 300$ °C (i.e. almost completely

quenched). This irreversible quenching might be attributed to oxidation of the ligands at elevated temperature, opening up more pathways for non-radiative decay and thus decreasing the emission probability. This was supported by the observation, that the colour of the sample powder turned from white (before heating was applied) to dark brown (after heating). Additionally, this observation indicates, that the absorption of excitation radiation by cerium ions might compete with absorption in the dark brown (possibly oxidized) material, thereby reducing the luminescence of interest.

The emission intensity ratios were obtained by integrating the area under the peaks of interest. The peak around $\lambda = 455$ nm is integrated between 450 nm – 462 nm, whereas the peak around $\lambda = 480$ nm is integrated between 462 nm – 500 nm. Using the integrated areas of the two peaks, the intensity ratios are calculated for each temperature. The black dots in the intensity ratios plot are the logarithm of the calculated intensity ratios at different temperatures (from room temperature up to $T = 250$ °C), the red, dashed line is a linear fit through the data points.

As shown in figure 4.10b, the intensity ratio increases as the temperature is increased. This corresponds well with the expected Boltzmann redistribution over the $^4I_{15/2}$ and $^4F_{9/2}$ energy levels. Although only a small amount of data points was measured and they do not show the expected linearity, a clear trend of increasing intensity ratio with increasing temperature is observed.

From the slope of the fit, an experimental energy difference between the thermally coupled $^4I_{15/2}$ and $^4F_{9/2}$ energy levels can be calculated, by dividing the slope by $-k_B$ (here, k_B is the Boltzmann constant of 0.695 cm⁻¹/K). This way, an experimental energy difference of $\Delta E = 875$ cm⁻¹ was obtained. This value is in good accordance with the value of $\Delta E = 950$ cm⁻¹ for the $^4I_{15/2}$ and $^4F_{9/2}$ energy levels, reported by Carnall *et al.*⁵³ Alternatively, the experimental energy difference between the $^4I_{15/2}$ and $^4F_{9/2}$ energy levels can be calculated from the difference in emission peak wavelength. This way, an energy difference of $\Delta E = 1062$ cm⁻¹ was obtained. Although larger than the energy difference calculated from the slope of the fit, this value, too, is in good accordance with the reported $\Delta E = 950$ cm⁻¹.

It is worthy to note, that the emission spectra were recorded from $\lambda = 450$ nm, whereas the spectra in figure 4.10a indicate that the peak around $\lambda = 455$ nm has an onset slightly below 450 nm (the peak is cut off at $\lambda = 450$ nm). However, the observations described above provide a good indication, that the expected temperature dependent emission is present in LaPO₄:Dy,Ce/LaPO₄ nanoparticles. Therefore, this specific material was not studied further, but instead, the observations discussed above were considered proof of principle in this system and improvements of this system were attempted.

4.1.4 LaPO₄:Dy,Ce/LaPO₄/Si nanoparticles

In order to obtain dysprosium emission at temperatures above 250 °C, nanoparticle thermal stabilization by the incorporation of these particles in silica spheres, via a reverse micro-emulsion method, was attempted.

LaPO₄:Dy,Ce/LaPO₄/Si synthesis, series

First, a series of five batches with increasing concentrations of LaPO₄:Dy,Ce/LaPO₄ nanoparticles, going from batch 1 – 5, was incorporated in silica spheres, via a reverse micro-emulsion method. Figure 4.11 shows TEM images of batch 1 (4.11a), batch 2 (4.11b), batch 3 (4.11c) and batch 5 (4.11d).

The TEM images of the products of batches 1, 2 and 3 were analyzed and a summary of the analysis is given in table 4.2. For the lowest concentration of nanoparticles (figure 4.11a), a

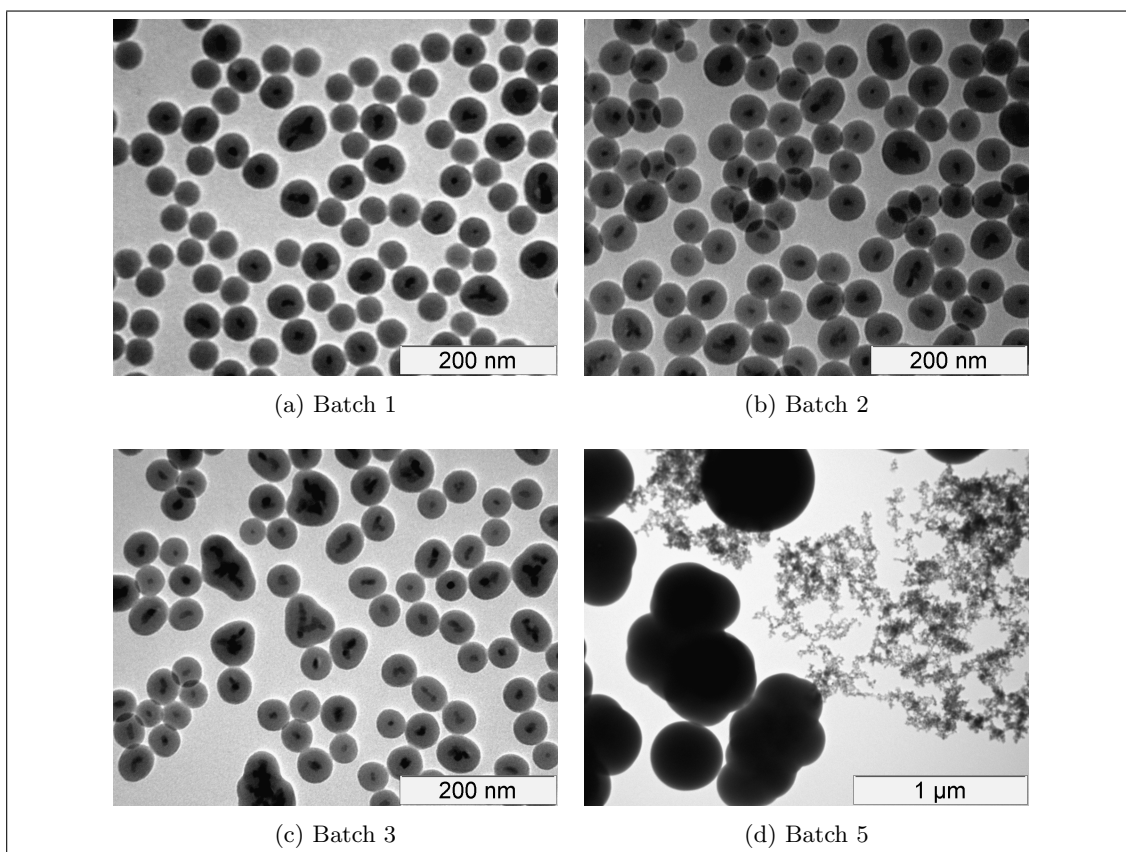


Figure 4.11: TEM images of different batches of silica shell growth on $\text{LaPO}_4:\text{Dy,Ce}/\text{LaPO}_4$ core-shell nanoparticles, with increasing concentrations of nanoparticles.

mixture of silica spheres containing either zero, one or a cluster of nanoparticles is observed. In the second batch (4.11b), the same is observed, but with far less empty silica spheres. In the third batch (4.11c), a mixture of silica spheres containing either one or a cluster of nanoparticles in an approximate ratio of 1 : 1 is observed. Since the third batch already showed a relatively low amount of single particles per silica sphere, batches 4 and 5 were not analyzed. At the highest concentration of nanoparticles, i.e. batch 5 (4.11d), large silica particles and large clusters of bare nanoparticles are observed.

These observations indicate that the synthesis of batch 2 has the optimal concentration of nanoparticles, since the relative amount of single particles per silica sphere is highest for this batch. If the concentration is too low, more empty silica spheres are observed, whereas if the concentration is too high, more silica spheres containing clusters of nanoparticles are observed. Counting of the particles was done by hand. If the contrast was too low to accurately determine the amount of nanoparticles within one silica sphere, that particle was neglected.

$\text{LaPO}_4:\text{Dy,Ce}/\text{LaPO}_4/\text{Si}$ synthesis, scaled up

Since batch 2 from the $\text{LaPO}_4:\text{Dy,Ce}/\text{LaPO}_4/\text{Si}$ synthesis series provided the product with the highest relative amount of single nanoparticles per silica sphere, the concentrations of the reaction for batch 2 were used to scale up the reaction, to obtain enough product for further analysis.

Table 4.2: Filling of silica spheres with $\text{LaPO}_4\text{:Dy,Ce/LaPO}_4$ particles for different batches, as observed in TEM images.

Batch	Amount of particles per silica sphere			
	Empty	One	Cluster	# Counted
1	68.5 %	16.5 %	15.0 %	314
2	1.6 %	64.4 %	34.0 %	376
3	0.0 %	50.8 %	49.2 %	329

Figure 4.12a shows the X-ray diffractogram of the product. The peaks in the diffractogram show the expected broadening and correspond well with literature references for monazite-phase LaPO_4 (JCPDS No. 01-084-0600, shown in green) and aluminium (shown in blue). However, the signal-to-noise ratio is relatively low and a broad band around $2\theta = 25^\circ$ is observed. This large band is caused by the large amount of amorphous silica that is present in the sample.⁵⁴ This also explains the low signal-to-noise ratio for the LaPO_4 peaks, since the presence of silica in the sample reduces the amount of LaPO_4 in the sample volume.

Figure 4.7b shows a TEM image of the product. TEM analysis of ~ 100 particles showed that the filling of the silica spheres is similar to that of batch 2 in table 4.2.

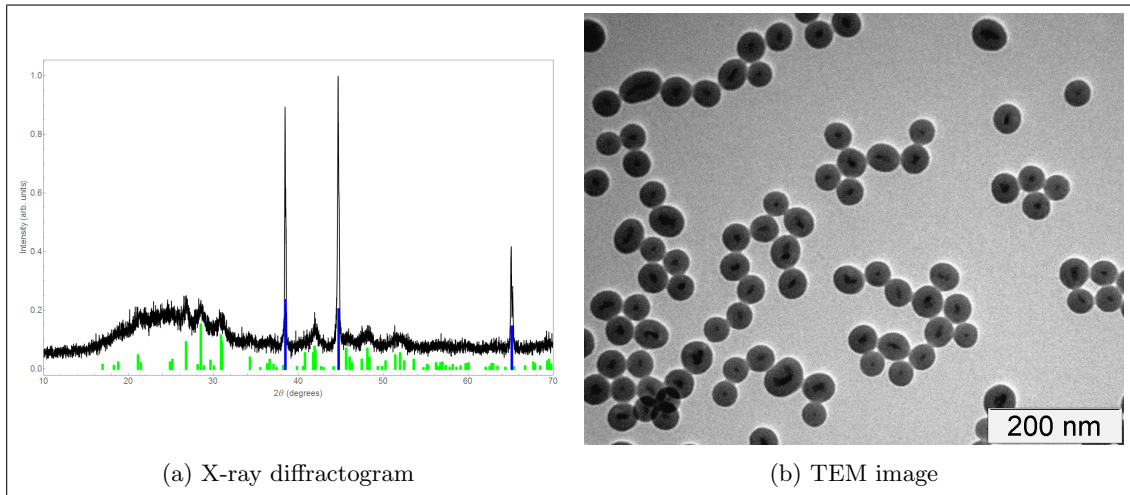


Figure 4.12: X-ray diffractogram (4.12a) and TEM image (4.12b) of the $\text{LaPO}_4\text{:Dy,Ce/LaPO}_4/\text{Si}$ product.

By analyzing the TEM images, the average diameter of the silica spheres was determined to be $\sim 41.3 \pm 2.5$ nm for silica spheres containing one nanoparticle. This is in good correspondence with the results in literature.³⁹

Figure 4.13 shows the emission spectrum of $\text{LaPO}_4\text{:Dy,Ce/LaPO}_4/\text{Si}$ at room temperature. The emission spectrum was recorded with an excitation wavelength of 285 nm. In the emission spectrum, both emission peaks around $\lambda = 480$ nm and 570 nm, that are expected for dysprosium, are observed. However, after the silica shell growth, the relative intensity of the peak around $\lambda = 570$ nm has increased, compared to the peak around $\lambda = 480$ nm.

It has been reported in literature, that the $^4\text{F}_{9/2} \rightarrow ^6\text{H}_{13/2}$ transition in trivalent dysprosium (around $\lambda = 570$ nm) is a hypersensitive electric dipole transition, of which the intensity can

be dependent on the local host environment, in contrast to the $^4F_{9/2} \rightarrow ^6H_{15/2}$ magnetic dipole transition (around $\lambda = 480$ nm).^{55,56} Since the LaPO_4 shell around the core particles is relatively thin, this might explain the relative intensity variation of these transitions upon silica coating.

However, since the transitions of interest for nanothermometry applications are expected to be the $^4I_{15/2} \rightarrow ^6H_{15/2}$ and $^4F_{9/2} \rightarrow ^6H_{15/2}$ transitions and not the $^4F_{9/2} \rightarrow ^6H_{13/2}$ transition, investigation of the origin of this relative intensity variation is beyond the scope of this project.

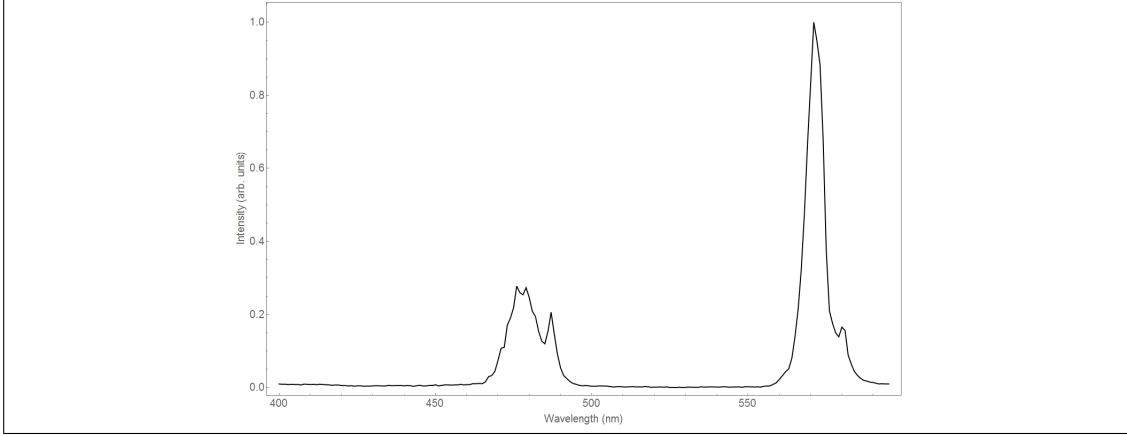


Figure 4.13: Emission spectrum of $\text{LaPO}_4:\text{Dy,Ce}/\text{LaPO}_4/\text{Si}$ particles ($\lambda_{ex} = 285$ nm).

Temperature dependent emission

In order to study temperature dependent dysprosium emission in $\text{LaPO}_4:\text{Dy,Ce}/\text{LaPO}_4/\text{Si}$ core-shell-shell nanoparticles, emission spectra were recorded at different temperatures, ranging from room temperature up to 450°C , in steps of $\Delta T = 25^\circ\text{C}$.

Figure 4.14 shows the emission spectra at different temperatures (4.14a) and the logarithm of the intensity ratios plotted against the inverse of the temperature (4.14b). The emission spectra were recorded with an excitation wavelength of 285 nm and are colour coded in a range from yellow (for $T = 22^\circ\text{C}$) to red (for $T = 450^\circ\text{C}$). All spectra are normalized at the peak around $\lambda = 480$ nm.

In all of the emission spectra, the peak around $\lambda = 480$ nm is observed, corresponding with the $^4F_{9/2} \rightarrow ^6H_{15/2}$ transition for dysprosium. Additionally, the expected peak around $\lambda = 455$ nm is observed at elevated temperatures, corresponding with the $^4I_{15/2} \rightarrow ^6H_{15/2}$ transition.

When the temperature is increased above 450°C , the luminescence signal decreases rapidly. As was the case for $\text{LaPO}_4:\text{Dy,Ce}/\text{LaPO}_4$, the overall emission intensity decreases as the temperature is increased. At $T = 300^\circ\text{C}$, approximately 70 % of the intensity at room temperature is observed, as opposed to the $\sim 5\%$ for the uncoated particles. Upon heating, the colour of the sample powder turned from white (before heating was applied) to light brown (after heating). These observations indicate that, despite the silica shell around the particles, there are still some organic ligands present on the surface of the LaPO_4 , which are oxidized at elevated temperatures and thereby irreversibly quench the luminescence. The presence of organic ligands in between the nanoparticle surface and silica shell has been reported previously, e.g. by Cannas *et al.*⁵⁷ However, the silica coated particles do show luminescence up to a higher temperature than the uncoated particles ($T = 450^\circ\text{C}$ versus $T = 250^\circ\text{C}$, respectively) and a much smaller decrease in emission intensity at $T = 300^\circ\text{C}$, indicating that the silica shell does indeed provide better thermal stability.

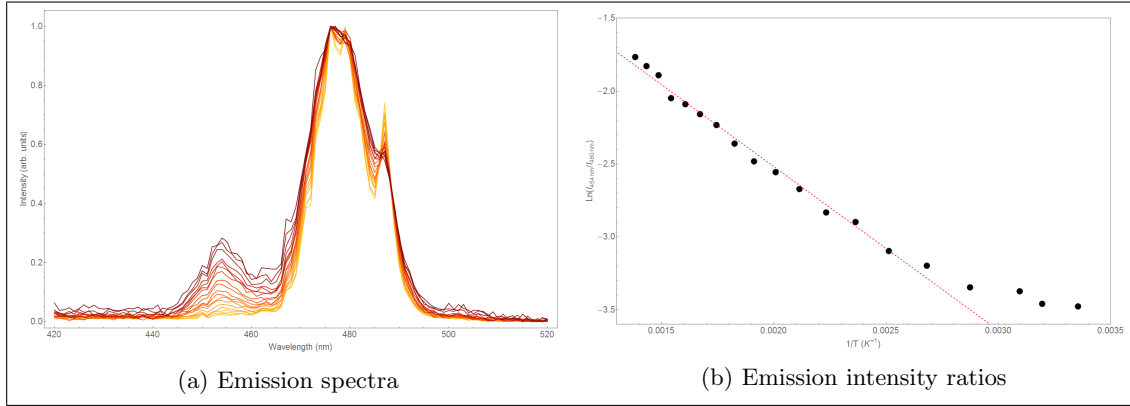


Figure 4.14: Emission spectra (4.14a) and intensity ratios (4.14b) of $\text{LaPO}_4:\text{Dy,Ce}/\text{LaPO}_4/\text{Si}$ particles at different temperatures.

The emission intensity ratios were again obtained by integrating the area under the peaks of interest. The peak around $\lambda = 455$ nm is integrated between 440 nm – 460 nm, whereas the peak around $\lambda = 480$ nm is integrated between 460 nm – 500 nm. Using the integrated areas of the two peaks, the intensity ratios are calculated for each temperature. The black dots in the intensity ratios plot are the logarithm of the calculated intensity ratios at different temperatures (from room temperature up to $T = 450$ °C), the red, dashed line is a linear fit through the data points corresponding to the temperature range of $T = 100$ °C – 450 °C.

As shown in figure 4.14b, the intensity ratio increases as the temperature is increased. This corresponds well with the expected Boltzmann redistribution over the $^4\text{I}_{15/2}$ and $^4\text{F}_{9/2}$ energy levels. Although the data points do not show the expected linearity, a clear trend is observed. The R-squared value for a linear fit of all data points, i.e. room temperature up to 450 °C, is $R^2 = 0.964$ (not shown in figure 4.14b). However, when a linear fit is applied to the data points from $T = 100$ °C – 450 °C (i.e. the first four data points are omitted in the determination of the fit), the R-squared value for the fit is $R^2 = 0.990$ (shown in figure 4.14b). This indicates that the intensity ratios curve becomes linear after a certain onset (above $T = 100$ °C).

From the slope of the fit, an experimental energy difference of $\Delta E = 1617 \text{ cm}^{-1}$ is obtained for the $^4\text{I}_{15/2}$ and $^4\text{F}_{9/2}$ energy levels, which is slightly larger than both the experimental energy difference of $\Delta E = 875 \text{ cm}^{-1}$ obtained from the fit for $\text{LaPO}_4:\text{Dy,Ce}/\text{LaPO}_4$ and the energy difference of $\Delta E = 950 \text{ cm}^{-1}$ reported by Carnall *et al.*⁵³

It has been reported by Henrie *et al.*, that the $^4\text{I}_{15/2} \rightarrow ^6\text{H}_{15/2}$ transition, corresponding to the emission peak around $\lambda = 455$ nm, is a hypersensitive transition.⁵⁸ This observation might explain the difference in the experimental ΔE values upon silica coating, since the silica coating potentially influences the relative intensity of the hypersensitive $^4\text{I}_{15/2} \rightarrow ^6\text{H}_{15/2}$ transition, which would, in turn, influence the emission intensity ratios. However, further studies of the hypersensitivity of this transition were difficult to find, such that the nature of this experimental difference remains unclear.

Influence of silica shell on luminescence quenching

In order to study the quenching of the emission in silica coated particles, a fresh batch of $\text{LaPO}_4:\text{Dy,Ce}/\text{LaPO}_4/\text{Si}$ was heated to 600 °C. Emission spectra were recorded at room temperature, $T = 300$ °C, $T = 450$ °C, $T = 600$ °C and again at room temperature after the heating process.

A summary of the emission intensities is given in table 4.3. Note that the first two rows of data are obtained from the measurements discussed above, in the parts labelled “Temperature dependent emission” of sections 4.1.3 and 4.1.4, respectively. Here, I_0 is the emission intensity before any heating is applied.

It is worthy to note, that in these types of measurements, aligning of the sample in the spectrophotometer is done by hand. This can influence the total intensity of light that is detected, due to inevitable small differences in alignment between the excitation source, the sample holder and the detector. Furthermore, the sample holders were never completely filled, in order to ensure a homogeneous temperature in the whole sample. This way, it is difficult to load the sample holder with the same amount of material each time. Thus, the absolute I_0 -value for the different materials is of little significance in these measurements.

Table 4.3: Emission intensities of $\text{LaPO}_4\text{:Dy,Ce/LaPO}_4$ and $\text{LaPO}_4\text{:Dy,Ce/LaPO}_4\text{/Si}$ particles during and after heating.

Material	Emission intensity as percentage of I_0				
	300 °C	450 °C	600 °	After heating	I_0 (counts)
$\text{LaPO}_4\text{:Dy,Ce/LaPO}_4$ heated to 300 °C	5 %	-	-	3 %	27 943
$\text{LaPO}_4\text{:Dy,Ce/LaPO}_4\text{/Si}$ heated to 450 °C	76 %	32 %	-	92 %	29 865
$\text{LaPO}_4\text{:Dy,Ce/LaPO}_4\text{/Si}$ heated to 600 °C	71 %	32 %	5 %	45 %	18 157

In table 4.3, it can clearly be seen that the emission intensity for silica coated particles at elevated temperatures is much higher than for uncoated particles. This supports the observations that the silica sphere provides better thermal stability, as discussed above. Furthermore, when $\text{LaPO}_4\text{:Dy,Ce/LaPO}_4\text{/Si}$ is heated to 450 °C, 92 % of the luminescence is preserved after cooling down to room temperature. This indicates that for $\text{LaPO}_4\text{:Dy,Ce/LaPO}_4\text{/Si}$, below $T = 450$ °C, the quenching is dominated by reversible thermal quenching. The irreversible quenching (caused by oxidation of organic ligands at the LaPO_4 surface) only affects the luminescence if the sample is heated above 450 °C.

Heating cycles

In order to study the stability of the particles, heating cycles were performed by heating the sample to 600 °C and cooling down to 35 °C three times. Emission spectra were recorded during each cycle at $T = 35$ °C, 300 °C and 600 °C. From these emission spectra, the intensity ratios between the peaks at $\lambda = 455$ nm and $\lambda = 480$ nm were calculated as described above.

Figure 4.15 shows the emission intensity ratios plotted against steps in the cycles (one step in the cycle is taken to be the heating or cooling step in between two measurements). In this figure, the yellow dots correspond to $T = 35$ °C, the orange dots correspond to $T = 300$ °C and the red dots correspond to $T = 600$ °C. The coloured lines are linear fits through data points of the corresponding temperature, the black, dashed line serves as a guide to the eye to illustrate the cycles. Due to an experimental error, the first emission spectrum in the cycle was recorded at room temperature, instead of at $T = 35$ °C. Therefore, the first data point in the cycle is omitted.

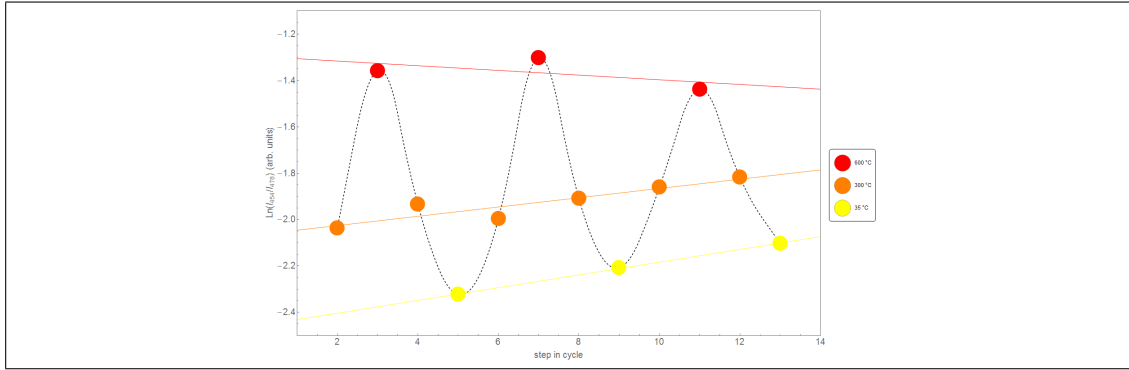


Figure 4.15: Emission intensity ratios of $\text{LaPO}_4\text{:Dy,Ce/LaPO}_4\text{/Si}$ particles during heating cycles ($35\text{ }^\circ\text{C} - 600\text{ }^\circ\text{C}$).

As can be seen in figure 4.15, the emission intensity ratios at a given temperature do not remain constant, neither do they show a constant degradation as the heating cycles are applied. It is worthy to note, that due to temperature related quenching (thermal quenching and irreversible quenching at elevated temperatures), the overall emission intensity decreases rapidly with each heating cycle. Due to the low signal-to-noise ratio that is caused by the quenching processes, accurate calculations of the intensity ratios are difficult. A summary of the intensities during the heating cycles is given in table 4.4.

In order to study to what extent irreversible quenching affects the luminescence properties after heating of the sample, the same procedure was repeated with a fresh sample, this time applying three heating cycles from $35\text{ }^\circ\text{C} - 450\text{ }^\circ\text{C}$. Figure 4.16 shows the emission intensity ratios plotted against steps in the cycles. The yellow dots correspond to $T = 35\text{ }^\circ\text{C}$, the orange dots to $T = 225\text{ }^\circ\text{C}$ and the red dots to $T = 450\text{ }^\circ\text{C}$. The coloured lines are linear fits through data points of the corresponding temperature, the black, dashed line serves as a guide to the eye to illustrate the cycles.

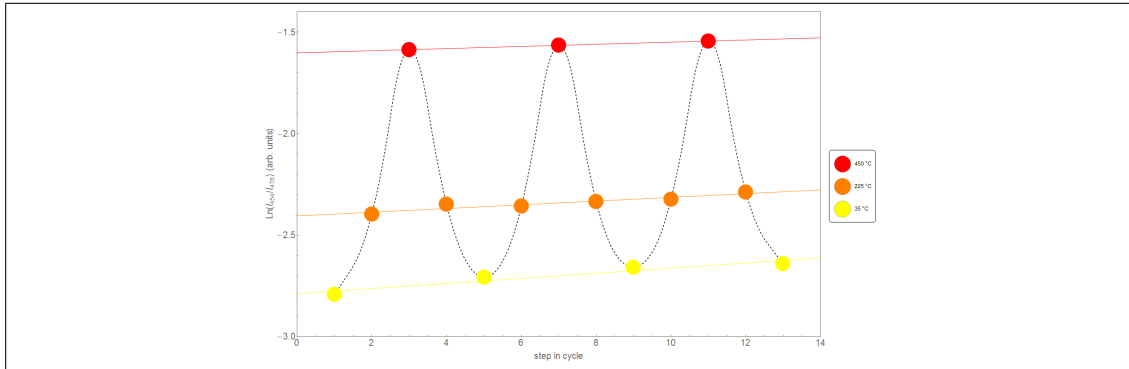


Figure 4.16: Emission intensity ratios of $\text{LaPO}_4\text{:Dy,Ce/LaPO}_4\text{/Si}$ particles during heating cycles ($35\text{ }^\circ\text{C} - 450\text{ }^\circ\text{C}$).

The emission intensity ratios in figure 4.16 show a more constant behaviour than for the heating cycles between $T = 35\text{ }^\circ\text{C} - 600\text{ }^\circ\text{C}$. Although there is a slight increase in intensity ratio after each heating cycle, the observed trend holds for three heating cycles. As was the case for the heating cycles between $T = 35\text{ }^\circ\text{C} - 600\text{ }^\circ\text{C}$, the emission intensity decreases with each

heating cycle. However, in this case, the decrease is smaller than for the heating cycles between $T = 35\text{ }^{\circ}\text{C} - 600\text{ }^{\circ}\text{C}$. A summary of the intensities during the heating cycles is given in table 4.4. Here, the intensities are expressed as percentage of I_0 , which is the intensity in the first step of the heating cycles (at $T = 35\text{ }^{\circ}\text{C}$, before additional heating is applied).

It is worthy to note, that in the heating cycle measurements, the samples are exposed to the corresponding elevated temperatures for longer periods of time, compared to the single heating measurements, as discussed earlier in this section (starting on page 35).

Table 4.4: Emission intensities of $\text{LaPO}_4\text{:Dy,Ce/LaPO}_4\text{/Si}$ particles during three heating cycles to $450\text{ }^{\circ}\text{C}$ and $600\text{ }^{\circ}\text{C}$, as percentage of I_0 .

Emission intensity as percentage of I_0							
	Cycle 1		Cycle 2		Cycle 3		
Temperature	T_{min}	T_{max}	T_{min}	T_{max}	T_{min}	T_{max}	T_{min}
$35\text{ }^{\circ}\text{C} - 450\text{ }^{\circ}\text{C}$	100 %	19.12 %	61.26 %	12.20 %	45.91 %	9.43 %	41.06 %
$35\text{ }^{\circ}\text{C} - 600\text{ }^{\circ}\text{C}$	100 %	9.73 %	45.23 %	9.76 %	38.06 %	9.79 %	30.85 %

$\xrightarrow{\hspace{15em}}$
Steps in heating cycles

As can be seen in table 4.4, the decrease in emission intensity is smaller if the sample is not heated above $450\text{ }^{\circ}\text{C}$. However, the emission intensity at $T = 35\text{ }^{\circ}\text{C}$ even after the first heating cycle (61.26 % of I_0) is lower than the 92 % reported in table 4.3 on page 37. Furthermore, a decrease in emission intensity at $T = 35\text{ }^{\circ}\text{C}$ after the first, second and third heating cycle is observed, going from 61.26 % of I_0 after the first heating cycle, to 41.06 % of I_0 after the third heating cycle. These observations indicate, that the irreversible quenching effects, expected to be the oxidation of organic ligands at the particle surface, still affect the luminescence if the sample is heated to $450\text{ }^{\circ}\text{C}$, albeit at a slower rate compared to heating to $600\text{ }^{\circ}\text{C}$.

X-ray diffraction after heating

In order to mimic the heating conditions of the temperature dependent emission measurements, fresh batches of $\text{LaPO}_4\text{:Dy,Ce/LaPO}_4\text{/Si}$ particles were placed in a tube oven and heated to $450\text{ }^{\circ}\text{C}$ and $600\text{ }^{\circ}\text{C}$ under air for 30 minutes. X-ray diffractograms of the sample were recorded before heating, after heating to $450\text{ }^{\circ}\text{C}$ and after heating to $600\text{ }^{\circ}\text{C}$. Figure 4.17 shows the X-ray diffractograms.

Although the signal-to-noise ratio is low, the peaks corresponding with LaPO_4 (JCPDS No. 01-084-0600, shown in green) and the large band around $2\theta = 25^{\circ}$ corresponding with amorphous silica are observed. The peaks for LaPO_4 become sharper as the sample is heated at higher temperature, which is an indication of increasing crystallite size. This can be due to a higher crystallinity of the particles due to the heating, or fusing together of clusters of nanoparticles within the silica spheres, since $\sim 34\text{ }%$ of the silica spheres are expected to contain clusters of LaPO_4 particles, as observed in section 4.1.4 on page 32.

However, this does not provide an explanation for the irreversible quenching of the luminescence, as observed in the temperature dependent emission measurements, since neither of these processes are expected to have a negative effect on the luminescence. Alternatively, the oxidation of organic ligands at the particle surface, as suggested origin of the irreversible quenching, can not be confirmed from these measurements, since this effect is not expected to influence the X-ray diffraction measurements.

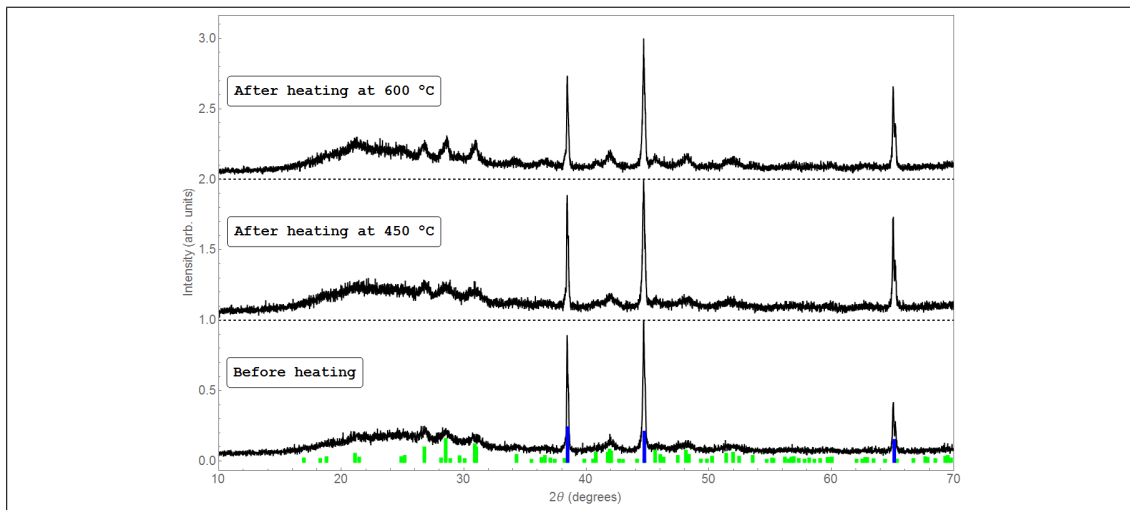


Figure 4.17: X-ray diffractograms of $\text{LaPO}_4:\text{Dy,Ce}/\text{LaPO}_4/\text{Si}$ nanoparticles before heating and after heating at different temperatures.

4.2 LaPO₄:Dy,Ce nanoparticles on gold nanoparticles

One of the potential applications of LaPO₄:Dy,Ce nanoparticles as nanothermometers, is on the surface of gold nanoparticles. Upon laser irradiation of the gold nanoparticles, localized surface plasmons can be generated, which can be of interest in a wide variety of different studies.⁵⁹ One of these studies, is the formation of nanobubbles around the gold surface, where very locally the pressure and temperature are expected to increase around the gold nanoparticle. Nanothermometry techniques might be applied in order to measure this localized temperature increase at the gold surface.

As a pilot for the use of LaPO₄:Dy,Ce nanoparticles as nanothermometers, a batch of these particles was linked to the surface of gold nanoparticles with a diameter of 81 nm, using lipoamide as a linker. This was performed by C. S. Wondergem, a more detailed explanation of this procedure can be found in appendix C on page 67.

Analysis of LaPO₄:Dy,Ce-coated gold nanoparticles

Figure 4.18a shows a TEM image of the LaPO₄:Dy,Ce nanoparticles on a single gold nanoparticle. The LaPO₄:Dy,Ce nanoparticles are visible in light grey on the surface of the larger, darker gold nanoparticle.

Figure 4.18b shows the emission spectra of the bare gold nanoparticles (4.18b bottom) and of LaPO₄:Dy,Ce-coated gold nanoparticles (4.18b top), recorded with an excitation wavelength of $\lambda_{ex} = 274$ nm. The emission spectra were obtained from dispersions of the samples in deionized water. Both spectra show features of the Au nanoparticles, while in the emission spectrum of the coated gold nanoparticles two extra peaks around $\lambda = 480$ nm and 570 nm are observed. These peaks correspond well with the expected dysprosium emission from LaPO₄:Dy,Ce, indicating that dysprosium emission is still present if the particles are linked to a gold surface.

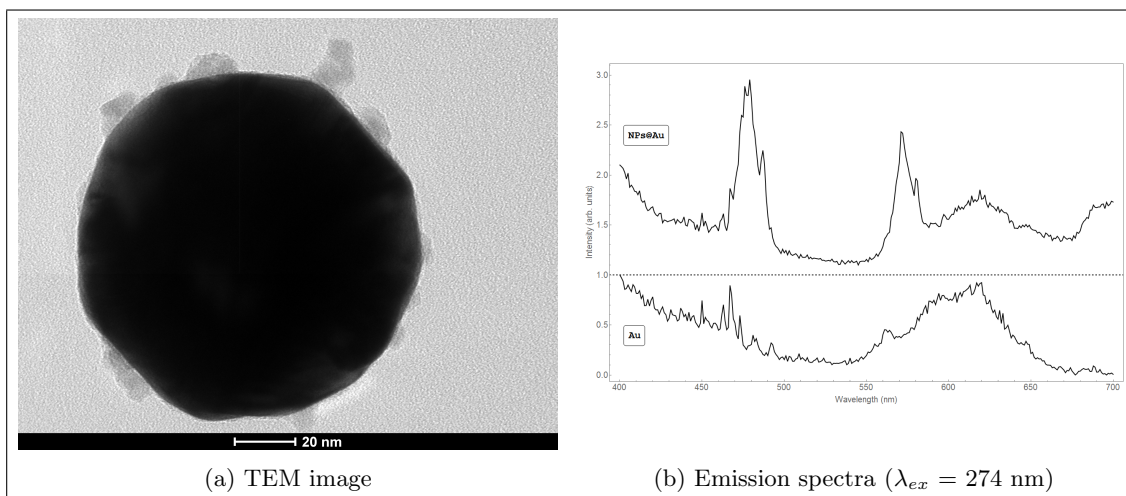


Figure 4.18: TEM image (4.18a) and emission spectrum (4.18b, top) of LaPO₄:Dy,Ce nanoparticles on Au nanoparticles. The emission spectrum of bare gold nanoparticles (4.18b, bottom) is shown for comparison.

In order to compare the dysprosium emission from LaPO₄:Dy,Ce nanoparticles to that of LaPO₄:Dy,Ce-coated gold nanoparticles, the emission spectrum of the bare gold nanoparticles was subtracted from the emission spectrum of the LaPO₄:Dy,Ce-coated particles. Figure 4.19

shows the resulting emission spectrum (4.19 bottom) and the emission spectrum of $\text{LaPO}_4:\text{Dy,Ce}$ nanoparticles (4.19 top) for comparison. This figure clearly shows good agreement between the two spectra, i.e. the presence of dysprosium emission peaks around $\lambda = 480$ nm and 570 nm, indicating that information about the dysprosium emission from the coated gold nanoparticles can, in principle, be extracted from the emission spectrum.

However, since the signal-to-noise ratio is very low and the dysprosium emission intensity is expected to decrease upon increasing the temperature, temperature measurements in this system are expected to be difficult.

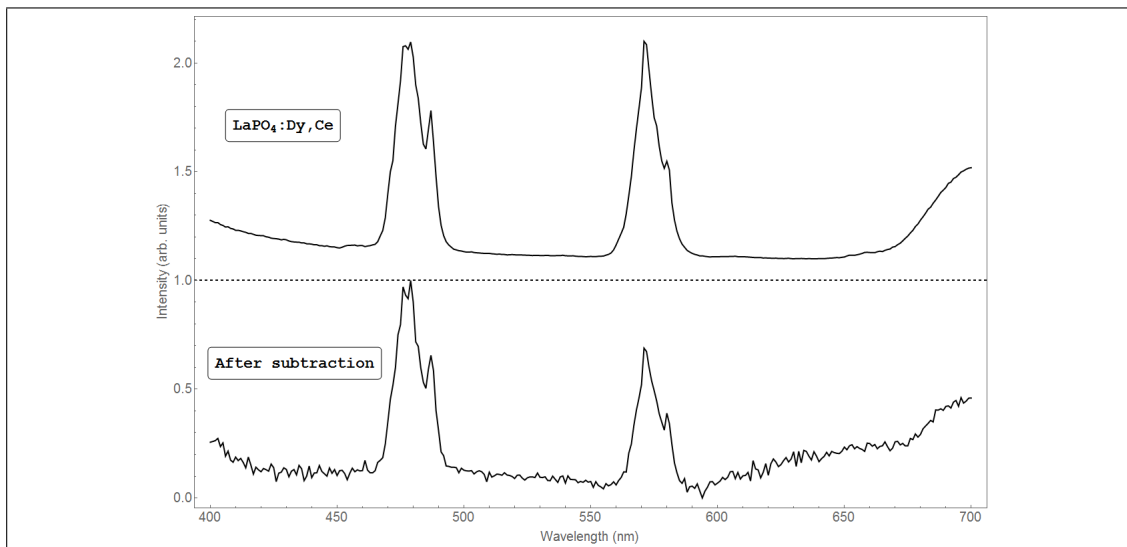


Figure 4.19: Emission spectrum of $\text{LaPO}_4:\text{Dy,Ce}$ nanoparticles (top) and of $\text{LaPO}_4:\text{Dy,Ce}$ nanoparticles on gold nanoparticles, after subtraction of the emission spectrum of bare gold nanoparticles (bottom).

Temperature dependent emission

In an attempt to measure temperature dependent dysprosium emission from $\text{LaPO}_4:\text{Dy,Ce}$ -coated gold nanoparticles, a powder sample holder was placed onto a heating plate, that was heated to $T \sim 50$ °C, and the sample dispersion was dropped onto the sample holder, to evaporate the water and obtain a dry sample. However, the amount of sample material obtained this way was very low, compared to the previous temperature dependent emission measurements, and accordingly, the total emission intensity was too low to measure emission spectra, even at room temperature.

Since the $\text{LaPO}_4:\text{Dy,Ce}$ -coated gold nanoparticles are difficult to obtain in larger quantities, the use of fluorescent nanoparticles that show a higher emission intensity compared to $\text{LaPO}_4:\text{Dy,Ce}$ might provide an interesting alternative in order to measure temperature dependent emission on the gold nanoparticle surface.

4.3 LaPO₄:Eu

In addition to the dysprosium-doped materials, different europium-doped LaPO₄ materials were synthesized, in an attempt to obtain higher intensity emission. These materials include:

- LaPO₄:Eu core nanoparticles Section 4.3.1 on page 43
- LaPO₄:Eu/LaPO₄ core-shell nanoparticles Section 4.3.2 on page 46

4.3.1 LaPO₄:Eu nanoparticles

First, monazite-phase LaPO₄:Eu nanoparticles doped with 5 mol% europium were synthesized.

Figure 4.20 shows the X-ray diffractogram of the product. The peaks in the diffractogram show the expected broadening and correspond well with literature references for monazite-phase LaPO₄ (JCPDS No. 01-084-0600, shown in green) and aluminium (shown in blue). Due to fitting difficulties, the peak around $2\theta = 42^\circ$ could not be used for evaluation of the Scherrer equation. Instead, the peak around $2\theta = 31^\circ$ was used, obtaining an average crystallite size of 5.65 nm.

Figure 4.20b shows a TEM image of the product. This image confirms the nanocrystalline size of the particles. However, the particles seem to be more aggregated than was the case for LaPO₄:Dy,Ce nanoparticles. Due to the low contrast in the TEM images of the product and the agglomeration of the particles, their size could not be determined accurately. Analysis of a small number of particles showed, that the average diameter seems to be in the same order of magnitude as was the case for LaPO₄:Dy,Ce core particles (~ 5 nm), corresponding well with the average crystallite size from the XRD data.

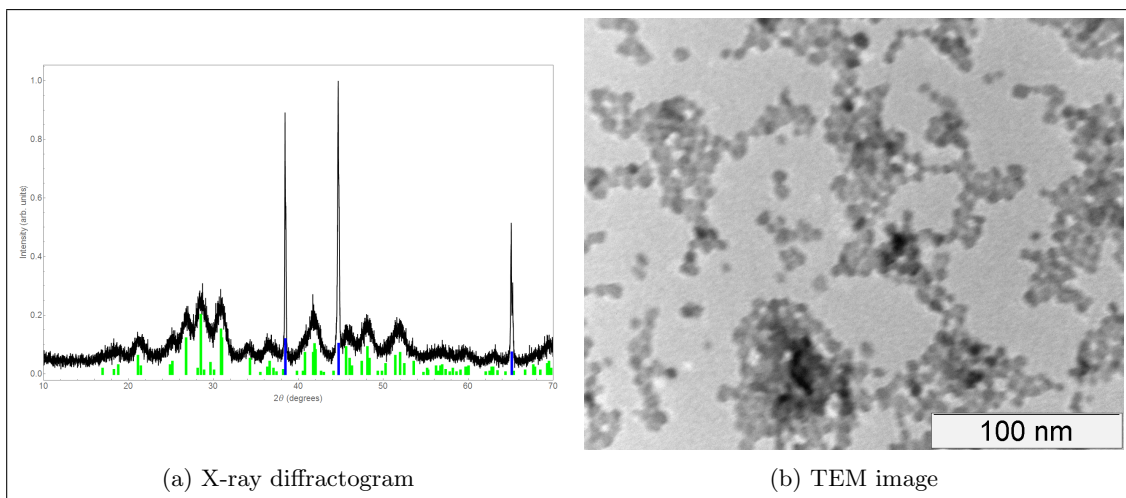


Figure 4.20: X-ray diffractogram (4.20a) and TEM image (4.20b) of the LaPO₄:Eu product.

Figure 4.21 shows the excitation and emission spectra of LaPO₄:Eu nanoparticles. The excitation spectrum (4.21a) was recorded with an emission wavelength of 592 nm. The emission spectrum (4.21b) was recorded with an excitation wavelength of 255 nm.

In the excitation spectrum, a broad band around $\lambda = 250$ nm is observed. This band is attributed to an oxygen-to-europium charge transfer band.^{46,60} At slightly higher energies, a number of smaller excitation peaks are observed, attributed to the direct excitation of europium ($4f - 4f$ transitions). As was the case for LaPO₄:Dy,Ce nanoparticles, the highest intensity

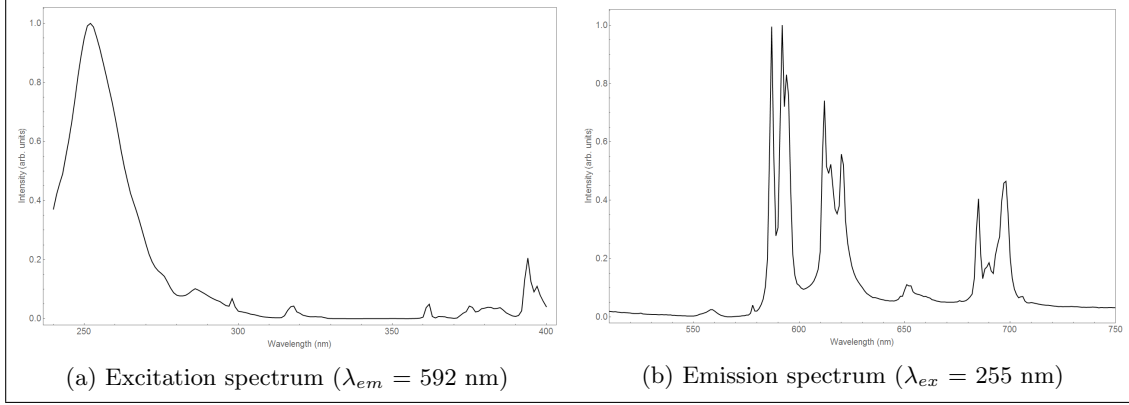


Figure 4.21: Excitation spectrum (4.21a) and emission spectrum (4.21b) of the $\text{LaPO}_4:\text{Eu}$ product.

excitation peak originates from an allowed transition (in this case excitation of the host lattice) and the direct $4f - 4f$ excitation peaks show a much lower intensity.

The measured excitation spectrum of $\text{LaPO}_4:\text{Eu}$ nanoparticles corresponds well with excitation spectra reported for different europium-doped materials, including $\text{LaPO}_4:\text{Eu}$ nanoparticles and nanofibers⁴⁶, europium-doped phosphate glasses^{61,62}, and different Eu^{3+} complexes⁶³. An overview of the different excitation peaks and their proposed corresponding transition is given in table 4.5.

Here, the relatively broad excitation band centered around $\lambda = 380$ nm is attributed to multiple ${}^7\text{F}_0 \rightarrow {}^5\text{G}_J$ transitions, where J can be 2, 3, 4, 5, 6. Additional to the excitation peaks between 300 nm - 400 nm, two small peaks or shoulders are observed around $\lambda = 285$ nm and 298 nm. Although these peaks are not attributed to corresponding Eu^{3+} $4f - 4f$ transitions in literature, they are observed in the reported excitation spectra.

Table 4.5: Overview of excitation transitions observed in $\text{LaPO}_4:\text{Eu}$ ($\lambda_{em} = 592$ nm).

Peak position (nm)	318	362	380	394
Eu^{3+} transition ^{46,61-63}	${}^7\text{F}_0 \rightarrow {}^5\text{H}_3$	${}^7\text{F}_0 \rightarrow {}^5\text{D}_4$	${}^7\text{F}_0 \rightarrow {}^5\text{G}_J$	${}^7\text{F}_0 \rightarrow {}^5\text{L}_6$

In the emission spectrum, several peaks or pairs of peaks are observed, including the peaks around $\lambda = 578$ nm, $\lambda = 590$ nm, $\lambda = 615$ nm, $\lambda = 655$ nm and $\lambda = 690$ nm. The emission spectrum corresponds well with emission spectra of $\text{LaPO}_4:\text{Eu}$ particles reported in literature.^{46,60,64} The different peaks from $\lambda = 578$ nm and higher are attributed to the ${}^5\text{D}_0 \rightarrow {}^7\text{F}_J$ europium transitions as shown in table 4.6. Additionally, a small peak around $\lambda = 560$ nm is observed, corresponding with the ${}^5\text{D}_1 \rightarrow {}^7\text{F}_0$ transition.

Table 4.6: Overview of emission transitions observed in $\text{LaPO}_4:\text{Eu}$ ($\lambda_{ex} = 255$ nm).

Peak position (nm)	578	580 - 600	610 - 630	655	680 - 710
Eu^{3+} transition	${}^5\text{D}_0 \rightarrow {}^7\text{F}_0$	${}^5\text{D}_0 \rightarrow {}^7\text{F}_1$	${}^5\text{D}_0 \rightarrow {}^7\text{F}_2$	${}^5\text{D}_0 \rightarrow {}^7\text{F}_3$	${}^5\text{D}_0 \rightarrow {}^7\text{F}_4$

An accurate analysis of the different excitation and emission transitions is beyond the scope of this project. However, the good agreement between the measured excitation and emission

spectra and reported excitation and emission spectra for different europium-doped materials, indicates that europium ions were successfully incorporated into the LaPO_4 host lattice.

Temperature dependent emission

In order to study temperature dependent europium emission in $\text{LaPO}_4\text{:Eu}$ nanoparticles, emission spectra were recorded at different temperatures, ranging from room temperature up to 250 °C, in steps of $\Delta T = 25$ °C.

Figure 4.22 shows the emission spectra at different temperatures (4.22a) and the logarithm of the intensity ratios plotted against the inverse of the temperature (4.22b). The emission spectra were recorded with an excitation wavelength of 255 nm and are colour coded in a range from yellow (for $T = 22$ °C) to red (for $T = 250$ °C). All of the spectra are normalized at the peak around $\lambda = 560$ nm and the emission spectra at temperatures ranging from room temperature up to 250 °C are shown.

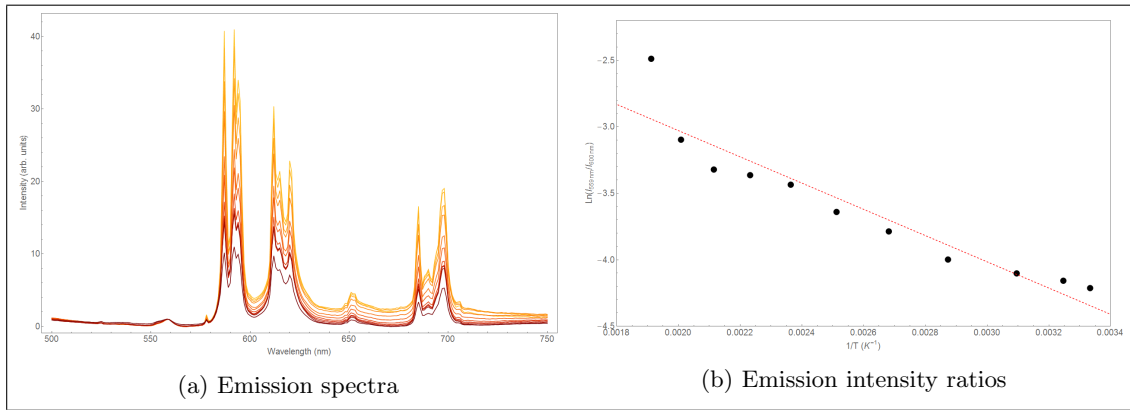


Figure 4.22: Emission spectra (4.22a) and intensity ratios (4.22b) of $\text{LaPO}_4\text{:Eu}$ nanoparticles at different temperatures.

In the emission spectra, the peaks corresponding with the $^5\text{D}_0 \rightarrow ^7\text{F}_J$ transitions in europium are observed, as well as the small peak around $\lambda = 560$ nm, corresponding with the $^5\text{D}_1 \rightarrow ^7\text{F}_0$ transition. Since the $^5\text{D}_0$ and $^5\text{D}_1$ levels are expected to be thermally coupled, the peak around $\lambda = 560$ nm and the peaks at slightly lower energies are the peaks of interest in the emission spectra.

As was the case for $\text{LaPO}_4\text{:Dy,Ce}/\text{LaPO}_4$ nanoparticles without silica coating, the emission intensity decreases rapidly when the temperature is increased above 250 °C. When the temperature is increased above $T = 300$ °C, the luminescence is almost completely quenched (the emission intensity is only ~ 2 % of the intensity at room temperature).

The emission intensity ratios were obtained by integrating the area under the peaks of interest. The peak around $\lambda = 560$ nm is integrated between 520 nm – 570 nm, whereas the peaks above $\lambda = 570$ nm are integrated between 570 nm – 750 nm. Using these integrated areas, the intensity ratios are calculated for each temperature. The black dots in the intensity ratios plot are the logarithm of the calculated intensity ratios at different temperatures (from room temperature up to 250 °C), the red, dashed line is a linear fit through the data points.

As shown in figure 4.22b, the intensity ratio increases as the temperature is increased. This corresponds well with the expected Boltzmann redistribution over the $^5\text{D}_0$ and $^5\text{D}_1$ energy levels. Since the energy gap between the $^5\text{D}_0$ and $^5\text{D}_1$ levels in europium is larger than the energy gap between the $^4\text{I}_{15/2}$ and $^4\text{F}_{9/2}$ levels in dysprosium, the temperature dependence is expected to

appear at higher temperatures. However, this is not clearly observed in the data (i.e. the increase in intensity ratio upon heating is already observed at room temperature). Although the data points do not show the expected linearity, a clear trend is observed. The observations described above provide a good indication that the expected temperature dependent emission is present in $\text{LaPO}_4\text{:Eu}$ nanoparticles.

From the slope of the fit, an experimental energy difference between the thermally coupled $^5\text{D}_0$ and $^5\text{D}_1$ energy levels of $\Delta E = 1420 \text{ cm}^{-1}$ was obtained. This value, although slightly lower, is in the same order of magnitude as the $\Delta E = 1746 \text{ cm}^{-1}$ as reported by Binnemans, for the $^5\text{D}_0$ and $^5\text{D}_1$ energy levels.⁶⁵

4.3.2 $\text{LaPO}_4\text{:Eu/LaPO}_4$ nanoparticles

Similar to the dysprosium-cerium co-doped core-shell nanoparticles described in chapter 4.1 (section 4.1.3, starting on page 28), europium-doped $\text{LaPO}_4\text{:Eu/LaPO}_4$ core-shell nanoparticles were synthesized in order to decrease the non-radiative decay pathways from the europium ions to the surrounding ligands or solvent.

Figure 4.23a (top) shows the X-ray diffractogram of the product. The peaks in the diffractogram show the expected broadening and correspond well with literature references for monazite-phase LaPO_4 (JCPDS No. 01-084-0600, shown in green) and aluminium (shown in blue). Furthermore, compared to the X-ray diffractogram of LaPO_4 core particles (figure 4.23a, bottom), the peaks are slightly sharper. This indicates that the shell growth was successful, since the increase of particle size due to the addition of a shell is expected to reduce the peak broadening. Evaluation of the Scherrer equation for the peak around $2\theta = 31^\circ$ yields an average crystallite size of 8.46 nm, further confirming a successful shell growth.

Figure 4.23b shows a TEM image of the product. This image confirms the nanocrystalline size of the particles. Due to the low contrast in the TEM images, the size of the particles could not be determined accurately. Analysis of a small number of particles showed, that the average diameter seems to be in the same order of magnitude as was the case for $\text{LaPO}_4\text{:Dy,Ce/LaPO}_4$ core-shell particles ($\sim 10 \text{ nm}$). It is worthy to note, that in figure 4.23b, it seems that particle size determination can easily be performed, due to the large amount of individual particles in the image. However, the magnification of this image was too low to accurately identify the edges of the smaller particles. For the images with larger magnification (not shown here), the contrast was too low to accurately determine the size of the particles.

Figure 4.24 shows the excitation and emission spectra of the $\text{LaPO}_4\text{:Eu/LaPO}_4$ core-shell nanoparticles. The excitation spectrum (4.24a) was recorded with an emission wavelength of 592 nm. The emission spectrum (4.24b) was recorded with an excitation wavelength of 255 nm.

The excitation and emission spectra of the $\text{LaPO}_4\text{:Eu/LaPO}_4$ core-shell nanoparticles show the same features as the spectra of the core particles, indicating that the core particles remain intact after shell growth. The intensity of the europium emission in core-shell nanoparticles is slightly less than for the core particles, but in the same order of magnitude ($I_{\text{max}} = 681\,195$ counts versus $I_{\text{max}} = 695\,051$ counts, respectively). However, the slightly lower emission intensity can be explained by the fact, that the core-shell particles contain more non-emitting material, i.e. the pure LaPO_4 shell. Since all luminescence measurements were performed with approximately the same amount of product, the absolute amount of emitting centres in the sample is lower for core-shell particles, thus leading to a lower emission signal. For this reason, the emission of core and core-shell particles can not be compared accurately from just the emission spectra.

However, compared to the dysprosium-cerium co-doped LaPO_4 core-shell nanoparticles, the europium-doped particles do show a much higher emission intensity ($I_{\text{max}} = 681\,195$ counts versus $I_{\text{max}} = 335\,952$ counts, respectively), which indicates that europium shows a higher intensity

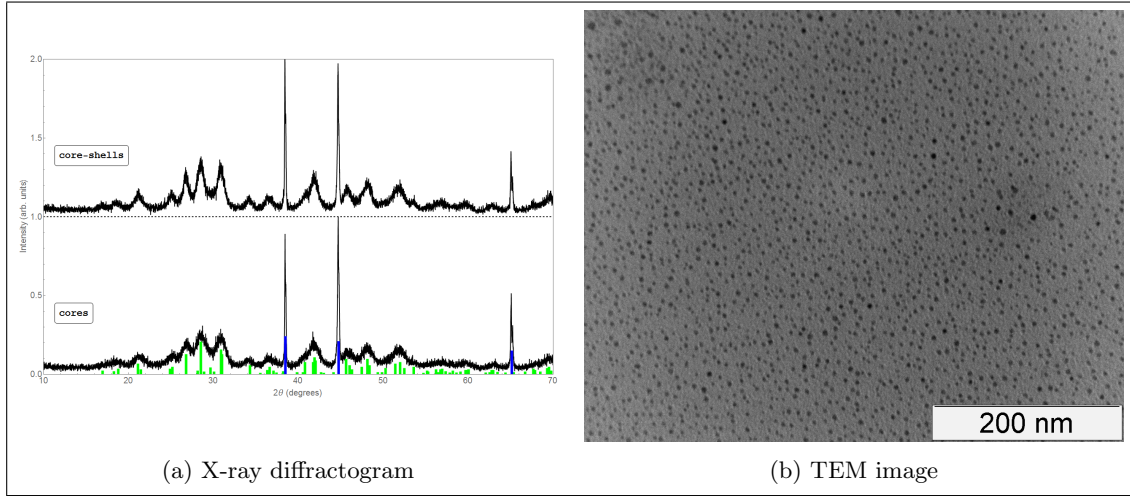


Figure 4.23: X-ray diffractogram (4.23a) and TEM image (4.23b) of the $\text{LaPO}_4\text{:Eu/LaPO}_4$ product.

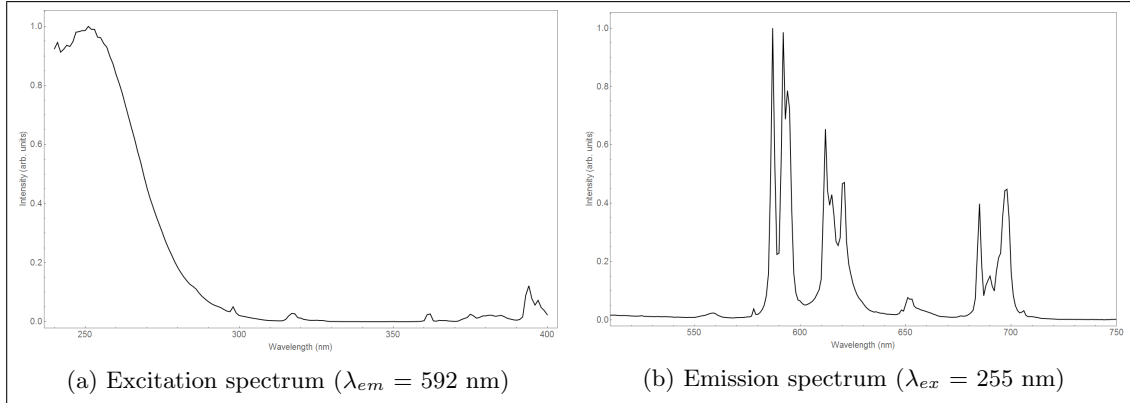


Figure 4.24: Excitation spectrum (4.24a) and emission spectrum (4.24b) of the $\text{LaPO}_4\text{:Eu/LaPO}_4$ product.

luminescence in the same host material. This is supported by the observation that, after excitation with a hand-held UV lamp, the luminescence of $\text{LaPO}_4\text{:Eu/LaPO}_4$ particles was observable by eye, whereas this was not the case for $\text{LaPO}_4\text{:Dy,Ce/LaPO}_4$ core-shell nanoparticles.

Temperature dependent emission

In order to study temperature dependent europium emission in $\text{LaPO}_4\text{:Eu/LaPO}_4$ core-shell nanoparticles, emission spectra were recorded at different temperatures, ranging from room temperature up to 300 °C, in steps of $\Delta T = 25$ °C.

Figure 4.25 shows the emission spectra at different temperatures (4.25a) and the logarithm of the intensity ratios plotted against the inverse of the temperature (4.25b). Emission spectra were recorded with an excitation wavelength of 255 nm and are colour coded in a range from yellow (for $T = 22$ °C) to red (for $T = 300$ °C). All of the spectra are normalized at the peak around $\lambda = 560$ nm and the emission spectra at temperatures from room temperature up to 300

°C are shown.

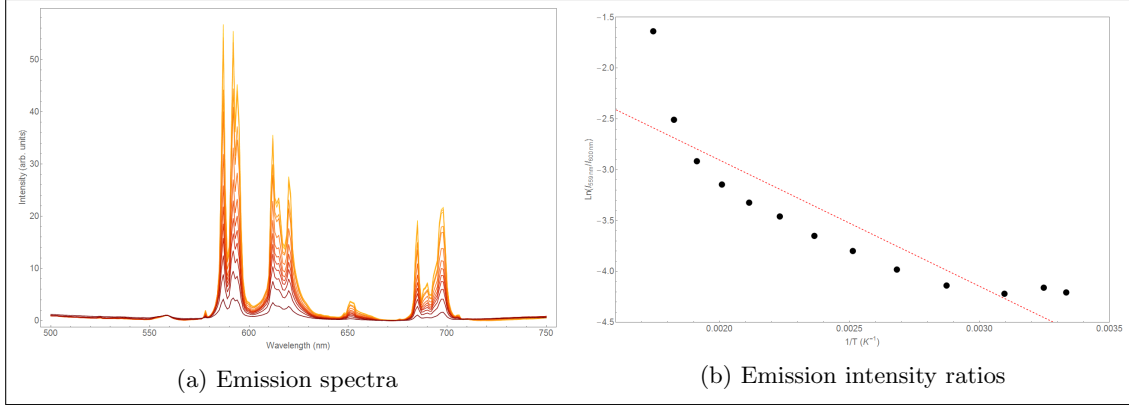


Figure 4.25: Emission spectra (4.25a) and intensity ratios (4.25b) of LaPO₄:Eu/LaPO₄ core-shell nanoparticles at different temperatures.

In the emission spectra, the peaks corresponding with the $^5D_0 \rightarrow ^7F_J$ and $^5D_1 \rightarrow ^7F_0$ transitions in europium are observed, which are the peaks of interest in the emission spectra.

As was the case for LaPO₄:Eu core nanoparticles and LaPO₄:Dy,Ce/LaPO₄ nanoparticles without silica coating, the emission intensity decreases rapidly when the temperature is increased. However, at $T = 300$ °C, the emission intensity of LaPO₄:Eu/LaPO₄ core-shell nanoparticles is ~ 11 % of the intensity at room temperature, which is slightly better than both the LaPO₄:Eu core nanoparticles and LaPO₄:Dy,Ce/LaPO₄ nanoparticles. At $T = 350$ °C, however, the emission intensity is further decreased to only ~ 1 % of the intensity at room temperature.

The emission intensity ratios were obtained by integrating the area under the peaks of interest. The peak around $\lambda = 560$ nm is integrated between 520 nm – 570 nm, whereas the peaks above $\lambda = 570$ nm are integrated between 570 nm – 750 nm. Using these integrated areas, the intensity ratios are calculated for each temperature. The black dots in the intensity ratios plot are the logarithm of the calculated intensity ratios at different temperatures (from room temperature up to 300 °C), the red, dashed line is a linear fit through the data points.

As shown in figure 4.25b, the intensity ratio increases as the temperature is increased. This corresponds well with the expected Boltzmann redistribution over the 5D_0 and 5D_1 energy levels. Furthermore, around $T = 300$ °C and up, the intensity ratios increase much faster than at lower temperatures. This indicates that the temperature dependence of the emission has an onset at lower temperatures (up to $T = 300$ °C) and then increases above $T = 300$ °C. This observation is in accordance to the larger energy gap between the 5D_0 and 5D_1 levels in europium, compared to the energy gap between the $^4I_{15/2}$ and $^4F_{9/2}$ levels in dysprosium. Although the data points do not show the expected linearity, a clear trend is observed. The observations described above provide a good indication that the expected temperature dependent emission is present in LaPO₄:Eu/LaPO₄ nanoparticles.

From the slope of the fit, an experimental energy difference between the thermally coupled 5D_0 and 5D_1 energy levels of $\Delta E = 1787$ cm⁻¹ was obtained. This value, is in good accordance with the $\Delta E = 1746$ cm⁻¹ as reported by Binnemans, for the 5D_0 and 5D_1 energy levels.⁶⁵

However, as observed in figure 4.25b, the slope of the intensity ratios becomes much steeper after the initial onset up to $T = 300$ °C, indicating that the experimental energy difference calculated at higher temperatures (above $T \sim 300$ °C) will not correspond with the energy difference reported by Binnemans.

It has been reported by Malta, that some of the $^5D_0 \rightarrow ^7F_J$ are hypersensitive transitions (i.e. the $^5D_0 \rightarrow ^7F_{2,4,6}$ transitions).⁶⁶ Similar to the $\text{LaPO}_4\text{:Dy,Ce}$ case, as discussed in section 4.1.4, this hypersensitivity might influence the relative intensity of the $^5D_0 \rightarrow ^7F_{2,4,6}$ transitions, thereby influencing the emission intensity ratios. However, detailed studies of the hypersensitivity of these transitions were difficult to find, such that the nature of this experimental difference remains unclear.

4.4 LaPO₄:Er,Yb

Since different erbium-ytterbium co-doped materials have been reported to be promising candidates for band shape luminescence nanothermometry, different erbium-ytterbium co-doped LaPO₄ materials were synthesized in addition to the dysprosium and europium-doped materials. These materials include:

- LaPO₄:Er,Yb core nanoparticles Section 4.4.1 on page 50
- LaPO₄:Er,Yb/LaPO₄ core-shell nanoparticles Section 4.4.2 on page 51
- LaPO₄:Er,Yb bulk Section 4.4.3 on page 51

4.4.1 LaPO₄:Er,Yb nanoparticles

First, monazite-phase LaPO₄:Er,Yb nanoparticles, co-doped with 2 mol% erbium and 18 mol% ytterbium, were synthesized.

Figure 4.26a shows the X-ray diffractogram of the product. Since the XRD analysis of this sample was only used as a quick check for the crystal structure, the diffractogram was measured in steps of $\Delta 2\theta = 0.05^\circ$ to decrease the measuring time (as opposed to the $\Delta 2\theta = 0.01^\circ$ for the standard XRD measurements). The peaks in the diffractogram show the expected broadening and correspond well with literature references for monazite-phase LaPO₄ (JCPDS No. 01-084-0600, shown in green) and aluminium (shown in blue). Evaluation of the Scherrer equation for the peak around $2\theta = 42^\circ$ resulted in a calculated average crystallite size of 3.21 nm. Although this is smaller than expected, this value does indicate peak broadening due to nanocrystalline particles. However, since the measurement was quickly performed and the signal-to-noise ratio was low, this value might deviate from the actual value.

Figure 4.26b shows a TEM image of the product. This image confirms the nanocrystalline size of the particles. Due to the low contrast in the TEM images of the product and the agglomeration of the particles, their size could not be determined accurately. Analysis of a small number of particles showed, that the average diameter seems to be in the same order of magnitude as was the case for the LaPO₄:Ln core particles discussed previously (~ 5 nm).

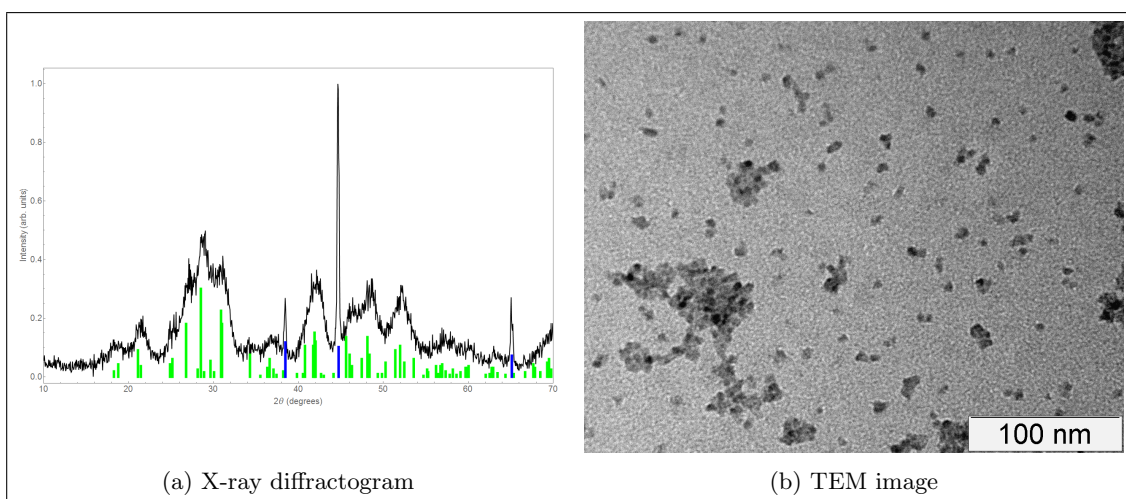


Figure 4.26: X-ray diffractogram (4.26a) and TEM image (4.26b) of the LaPO₄:Er,Yb product.

Emission measurements of $\text{LaPO}_4\text{:Er,Yb}$ nanoparticles were attempted with excitation wavelengths of $\lambda = 378$ nm, 485 nm and laser excitation at $\lambda = 980$ nm. However, no emission was observed in the range of $\lambda = 400$ nm – 700 nm.

4.4.2 $\text{LaPO}_4\text{:Er,Yb/LaPO}_4$ nanoparticles

In an attempt to decrease non-radiative decay pathways and observe erbium luminescence in a nanocrystalline LaPO_4 host, $\text{LaPO}_4\text{:Er,Yb/LaPO}_4$ core-shell nanoparticles were synthesized.

Figure 4.27a (top) shows the X-ray diffractogram of the product. The peaks in the diffractogram show the expected broadening and correspond well with literature references for monazite-phase LaPO_4 (JCPDS No. 01-084-0600, shown in green) and aluminium (shown in blue). Evaluation of the Scherrer equation for the peak around $2\theta = 42^\circ$ resulted in a calculated average crystallite size of 6.44 nm. The increase compared to the calculated average crystallite size for the core particles indicates successful shell growth. Furthermore, the reduced peak broadening for the core-shell particles is clearly observable by eye in the measured X-ray diffractogram.

Figure 4.27b shows a TEM image of the product. This image confirms the nanocrystalline size of the particles.

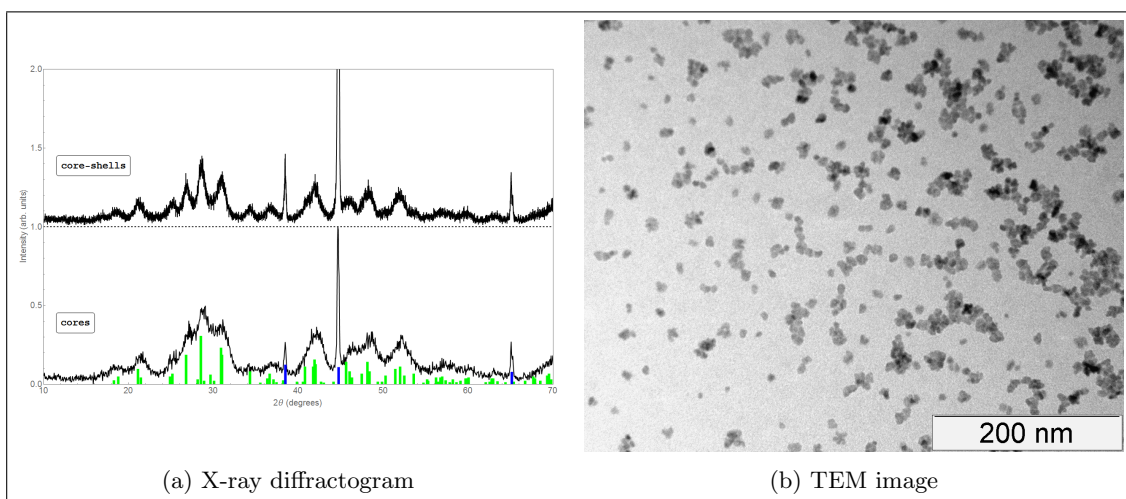


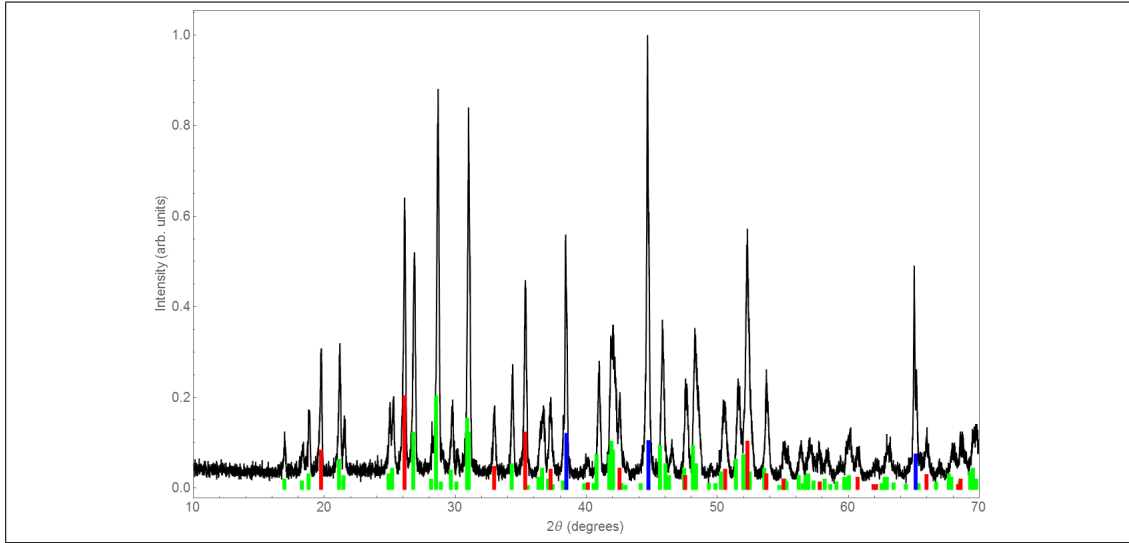
Figure 4.27: X-ray diffractogram (4.27a) and TEM image (4.27b) of the $\text{LaPO}_4\text{:Er,Yb/LaPO}_4$ product.

Emission measurements of $\text{LaPO}_4\text{:Er,Yb/LaPO}_4$ nanoparticles were attempted with excitation wavelengths of $\lambda = 378$ nm, 485 nm and laser excitation at $\lambda = 980$ nm. However, no emission was observed in the range of $\lambda = 400$ nm – 700 nm.

4.4.3 $\text{LaPO}_4\text{:Er,Yb bulk}$

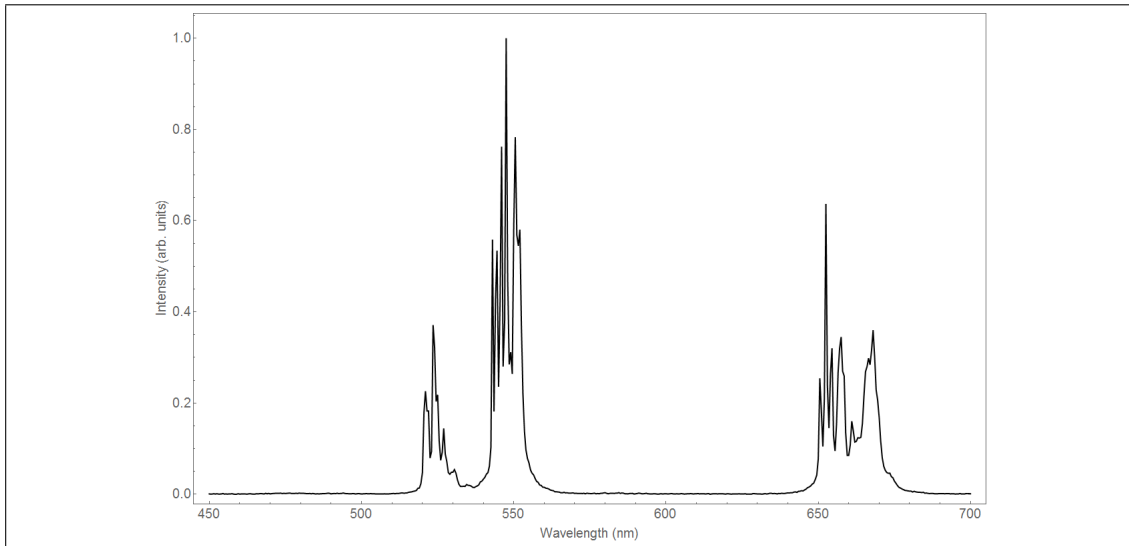
In an attempt to observe erbium luminescence in LaPO_4 , bulk $\text{LaPO}_4\text{:Er,Yb}$ was synthesized.

Figure 4.28 shows the X-ray diffractogram of the product. In the diffractogram, sharp peaks are observed, which is expected for bulk material. In addition to the peaks that correspond well with the monazite-phase LaPO_4 (JCPDS No. 01-084-0600, shown in green) and aluminium (shown in blue) references, peaks corresponding well with a reference for YbPO_4 are observed (JCPDS No. 00-045-0530, shown in red).

Figure 4.28: X-ray diffractogram of the bulk $\text{LaPO}_4\text{:Er,Yb}$ product.

The presence of the YbPO_4 peaks in the diffractogram indicates that ytterbium forms a separate phase in the product and is not properly incorporated in the LaPO_4 lattice. Since erbium and ytterbium phosphate nanoparticles are reported to show a similar crystal structure (with similar XRD patterns), the erbium atoms in the product are expected to be in the YbPO_4 phase in the product, rather than incorporated in the LaPO_4 lattice. Therefore, LaPO_4 is not considered a good host material for this specific system.

Figure 4.29 shows the emission spectrum of bulk $\text{LaPO}_4\text{:Er,Yb}$. The sample was excited by laser excitation at $\lambda = 980$ nm.

Figure 4.29: Emission spectrum of bulk $\text{LaPO}_4\text{:Er,Yb}$ ($\lambda_{ex} = 980$ nm).

In the emission spectrum, groups of peaks are observed around $\lambda = 525$ nm, $\lambda = 550$ nm and

$\lambda = 660$ nm. These peaks are attributed to emission from the following transitions in erbium: $^2H_{11/2} \rightarrow ^4I_{15/2}$ (525 nm), $^4S_{3/2} \rightarrow ^4I_{15/2}$ (550 nm) and $^4F_{9/2} \rightarrow ^4I_{15/2}$ (660 nm).^{67,68}

These observations indicate that ytterbium-erbium upconversion is present in this material. However, since both the ytterbium and erbium atoms are not expected to be incorporated in the $LaPO_4$ lattice, further studies of erbium-ytterbium co-doped $LaPO_4$ were not performed.

The concentrations of erbium and ytterbium dopants in this study (2 mol% and 18 mol%, respectively), were derived from previous studies of erbium-ytterbium co-doped $NaYF_4$.⁶⁹ However, it is well possible that the ideal concentrations of erbium and ytterbium in $LaPO_4$ differ from these concentrations. For instance, Lisiecki *et al.* reported erbium luminescence and ytterbium-erbium upconversion in $LaPO_4$ crystals at dopant concentrations of 0.1 mol% erbium and 0.1 mol% ytterbium.⁷⁰ The absence of erbium emission as described above, might be attributed to concentration quenching, since the dopant concentrations are much larger than the 0.1 mol% reported by Lisiecki *et al.* Although lowering the dopant concentrations might result in erbium luminescence in $LaPO_4$ nanoparticles, due to time constraints, experiments with lower concentrations of erbium and ytterbium were not performed.

4.5 YPO₄:Er,Yb

In an attempt to obtain erbium emission in a different, but similar host material, different erbium-ytterbium co-doped YPO₄ materials were synthesized. These materials include:

- YPO₄:Er,Yb core nanoparticles Section 4.5.1 on page 54
- YPO₄:Er,Yb/YPO₄ core-shell nanoparticles Section 4.5.2 on page 54
- YPO₄:Er,Yb/LaPO₄ core-shell nanoparticles Section 4.5.3 on page 56
- YPO₄:Er,Yb bulk Section 4.5.4 on page 57

4.5.1 YPO₄:Er,Yb nanoparticles

First, xenotime-phase YPO₄:Er,Yb nanoparticles, co-doped with 2 mol% erbium and 18 mol% ytterbium, were synthesized.

Figure 4.30a shows the X-ray diffractogram of the product. The peaks in the diffractogram show the expected broadening and correspond well with literature references for the xenotime-phase known for bulk YPO₄ (JCPDS No. 01-083-0658, shown in green) and aluminium (shown in blue). By evaluation of the Scherrer equation for the peak around $2\theta = 26^\circ$, an average crystallite size of 5.04 nm is obtained.

Figure 4.30b shows a TEM image of the product. This image confirms the nanocrystalline size of $\sim 5.3 \pm 1.2$ nm of the particles.

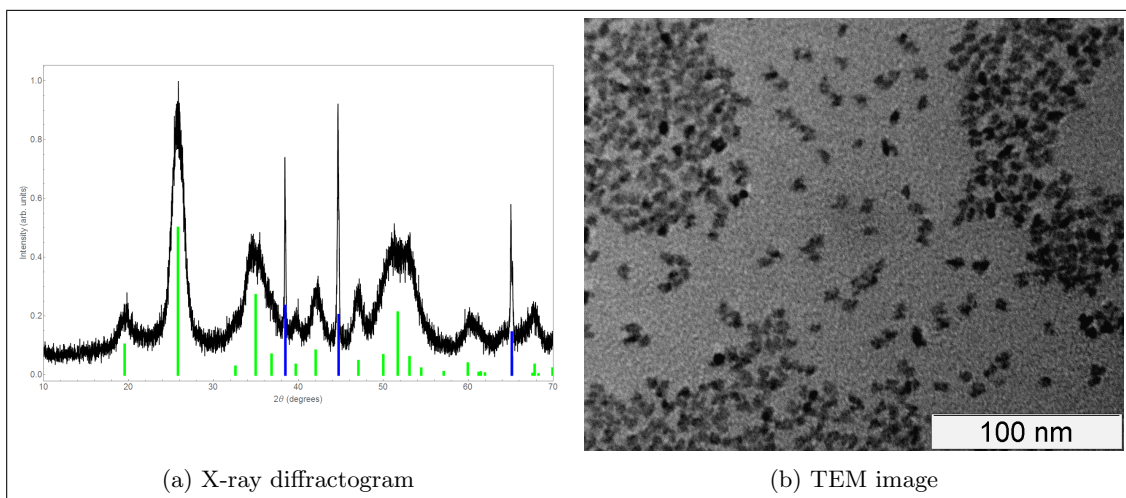


Figure 4.30: X-ray diffractogram (4.30a) and TEM image (4.30b) of the YPO₄:Er,Yb product.

Emission measurements of YPO₄:Er,Yb nanoparticles were attempted with excitation wavelengths of $\lambda = 378$ nm, 485 nm and laser excitation at $\lambda = 980$ nm. However, no emission was observed in the range of $\lambda = 400$ nm – 700 nm.

4.5.2 YPO₄:Er,Yb/YPO₄ nanoparticles

In an attempt to decrease non-radiative decay pathways and observe erbium luminescence in a nanocrystalline YPO₄ host, YPO₄:Er,Yb/YPO₄ core-shell nanoparticles were synthesized.

Direct YPO_4 coating

First, $\text{YPO}_4\text{:Er,Yb}/\text{YPO}_4$ core-shell nanoparticles were synthesized using the same method as for the LaPO_4 core-shell nanoparticles (i.e. direct coating of the crude core product).

Figure 4.31a shows the X-ray diffractogram of the product. While the most intense peak expected for YPO_4 is present in the diffractogram, all other expected peaks are either shifted or absent. By evaluation of the Scherrer equation for the peak around $2\theta = 26^\circ$, an average crystallite size of 9.11 nm is obtained.

Figure 4.31b shows a TEM image of the product. In the TEM image, nanocrystalline particles are observed. However, large parts of unidentified material are also observed. Although the average crystallite size as calculated using the Scherrer equation increases upon shell growth, the deviation of the X-ray data and the observations in the TEM images do not provide sufficient indication that the shell growth was successful.

These observations indicate that, although the core particle synthesis appears to be successful, the direct synthesis method of core-shell nanoparticles is not directly applicable for YPO_4 materials. Therefore, the average size of the particles was not determined from the TEM data.

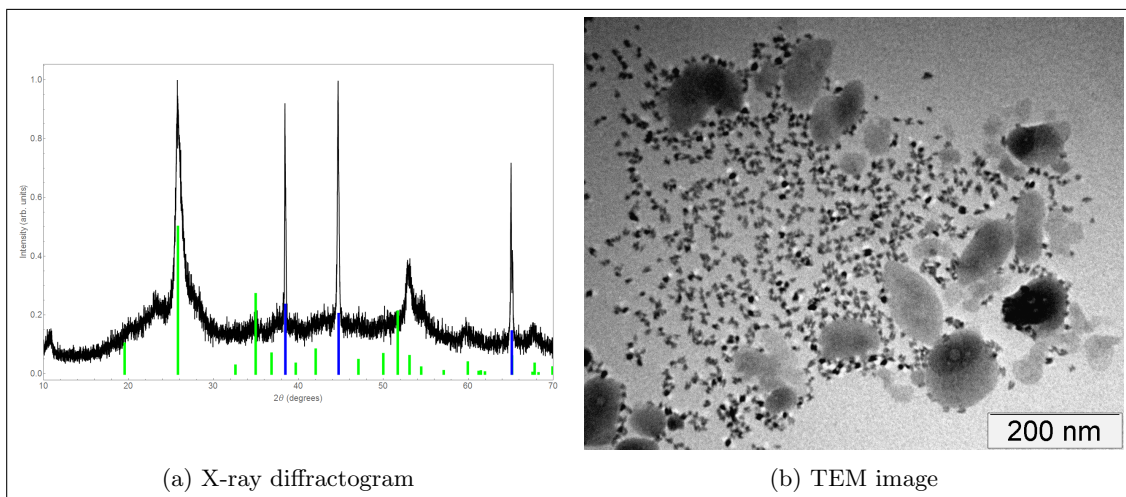


Figure 4.31: X-ray diffractogram (4.31a) and TEM image (4.31b) of the $\text{YPO}_4\text{:Er,Yb}/\text{YPO}_4$ product.

Emission measurements of $\text{YPO}_4\text{:Er,Yb}/\text{YPO}_4$ nanoparticles were attempted with excitation wavelengths of $\lambda = 378$ nm, 485 nm and laser excitation at $\lambda = 980$ nm. However, no emission was observed in the range of $\lambda = 400$ nm – 700 nm.

Aqueous YPO_4 coating

In an attempt to coat the $\text{YPO}_4\text{:Er,Yb}$ core nanoparticles with a pure YPO_4 shell, an aqueous coating method was applied.

Figure 4.32a show the X-ray diffractogram of the product. The peaks in the diffractogram correspond well with literature references for YPO_4 (JCPDS No. 01-083-0658, shown in green) and aluminium (blue). Furthermore, the observed peaks show less broadening than the peaks in the X-ray diffractogram for the core product, indicating that the crystallite size has increased due to the coating.

Figure 4.32b shows a TEM image of the product. In the TEM image, two types of particles are observed. The product is a mixture of the expected nanocrystalline particles and larger particles, with a rod-like or platelet-like morphology. These rod-like particles are attributed to the formation of independent YPO_4 particles.³⁸ Furthermore, analysis of the TEM images revealed that there were large parts of unidentified material present in the product, similar to the product of the direct YPO_4 coating method (figure 4.31b).

These observations indicate that the aqueous coating method was not successful. Therefore, the average size of the particles was not determined.

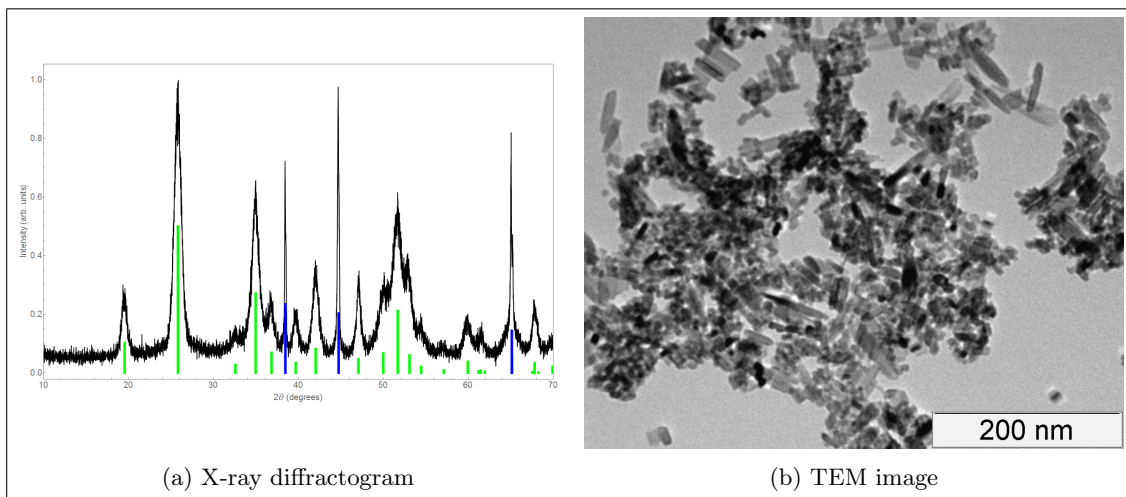


Figure 4.32: X-ray diffractogram (4.32a) and TEM image (4.32b) of the $\text{YPO}_4\text{:Er,Yb/YPO}_4$ product (aqueous coating method).

Emission measurements of $\text{YPO}_4\text{:Er,Yb/YPO}_4$ nanoparticles (obtained via aqueous coating method) were attempted with excitation wavelengths of $\lambda = 378$ nm, 485 nm and laser excitation at $\lambda = 980$ nm. However, no emission was observed in the range of $\lambda = 400$ nm – 700 nm.

4.5.3 $\text{YPO}_4\text{:Er,Yb/LaPO}_4$ nanoparticles

In an attempt to coat $\text{YPO}_4\text{:Er,Yb}$ nanoparticles with a pure LaPO_4 shell, $\text{YPO}_4\text{:Er,Yb/LaPO}_4$ core-shell nanoparticles were synthesized via direct coating method.

Figure 4.33a (top) shows the X-ray diffractogram of the product. The peaks in the diffractogram correspond well with a mixture of literature references for YPO_4 (JCPDS No. 01-083-0658, shown in green), LaPO_4 (JCPDS No. 01-084-0600, shown in red) and aluminium (shown in blue). This indicates that LaPO_4 has formed in the reaction. However, the XRD data do not provide evidence for successful LaPO_4 coating on the surface of the $\text{YPO}_4\text{:Er,Yb}$ nanoparticles, since formation of separate pure LaPO_4 nanoparticles during the coating step is expected to result in the same observations as described here. Therefore, successful coating of the particles can not be confirmed with this analysis.

Figure 4.33b shows a TEM image of the product. This image confirms the nanocrystalline size of the particles. Due to the low contrast in the TEM images, the size of the particles could not be determined accurately. Analysis of a small number of particles showed, that the average diameter seems to be around ~ 7 nm, which is in between the average sizes for core particles (~ 5 nm) and core-shell particles (~ 10 nm) as discussed above. This could indicate that there are both surface coating and separate nanoparticle formation processes present in this reaction.

However, due to the small amount of particles measured for the size determination, sufficient evidence for this observation is lacking.

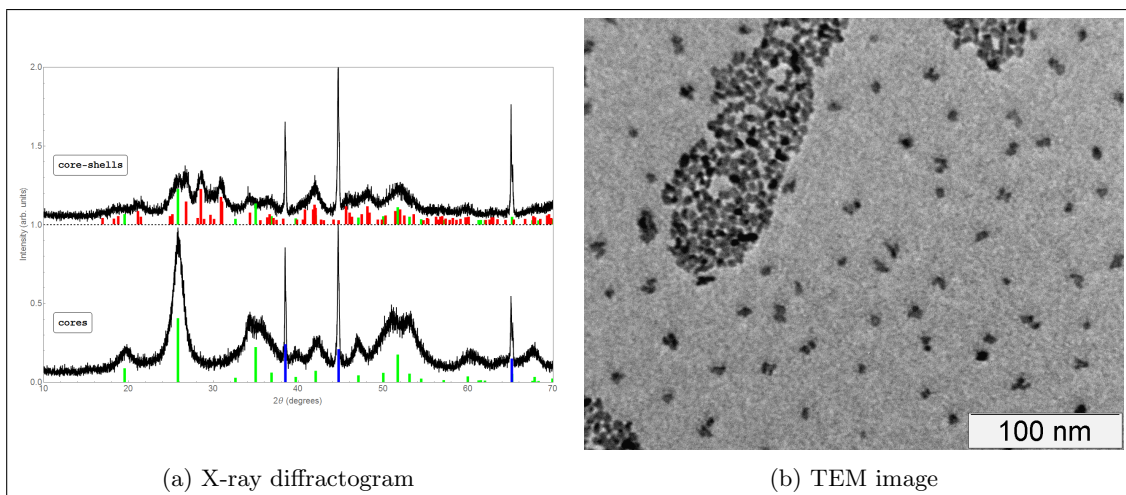


Figure 4.33: X-ray diffractogram (4.33a) and TEM image (4.33b) of the $\text{YPO}_4\text{:Er,Yb/LaPO}_4$ product.

Emission measurements of $\text{YPO}_4\text{:Er,Yb/LaPO}_4$ nanoparticles were attempted with excitation wavelengths of $\lambda = 378$ nm, 485 nm and laser excitation at $\lambda = 980$ nm. However, no emission was observed in the range of $\lambda = 400$ nm – 700 nm.

These observations can indicate that either the LaPO_4 coating was not successful, or that the addition of a LaPO_4 shell on the surface of the $\text{YPO}_4\text{:Er,Yb}$ nanoparticles is not sufficient to allow observation of erbium luminescence in this material.

4.5.4 $\text{YPO}_4\text{:Er,Yb}$ bulk

In an attempt to observe erbium luminescence in YPO_4 , bulk $\text{YPO}_4\text{:Er,Yb}$ was synthesized.

Figure 4.34 shows the X-ray diffractogram of the product. In the diffractogram, sharp peaks are observed, which is expected for bulk material. The peaks in the diffractogram correspond well with references for xenotime-phase YPO_4 (JCPDS No. 01-083-0658, shown in green) and aluminium (shown in blue). Additional to the peaks that originate from the YPO_4 crystal structure, some low intensity peaks are observed, that are not present in the reference. Comparison with different yttrium, phosphor and oxygen containing references, however, did not provide a match with the measured diffractogram, such that the nature of these additional peaks remains unclear.

Figure 4.35 shows the emission spectrum of bulk $\text{YPO}_4\text{:Er,Yb}$. The sample was excited by laser excitation at $\lambda = 980$ nm.

In the emission spectrum, the same groups of peaks are observed as was the case for the emission spectrum of bulk $\text{LaPO}_4\text{:Er,Yb}$ (discussed in section 4.4.3 on page 51). There are groups of peaks around $\lambda = 525$ nm, $\lambda = 550$ nm and $\lambda = 660$ nm. Similarly, these peaks are attributed to emission from the following transitions in erbium: $^2\text{H}_{11/2} \rightarrow ^4\text{I}_{15/2}$ (525 nm), $^4\text{S}_{3/2} \rightarrow ^4\text{I}_{15/2}$ (550 nm) and $^4\text{F}_{9/2} \rightarrow ^4\text{I}_{15/2}$ (660 nm).

These observations indicate that ytterbium-erbium upconversion is present in $\text{YPO}_4\text{:Er,Yb}$ bulk material and, thus, that improved control over the synthesis of $\text{YPO}_4\text{:Er,Yb}$ nanoparticles

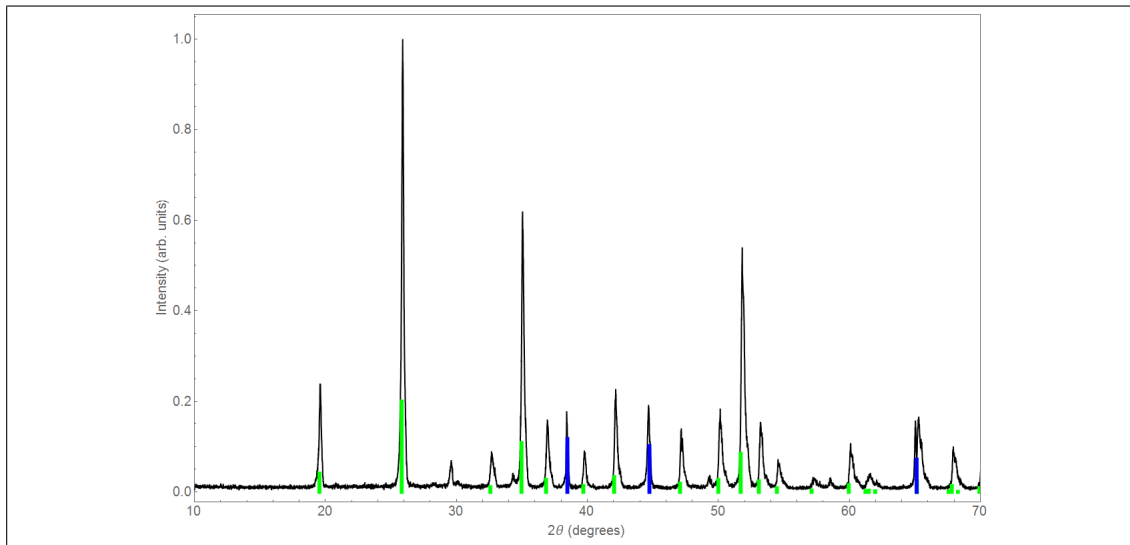


Figure 4.34: X-ray diffractogram of the bulk $\text{YPO}_4\text{:Er,Yb}$ product.

may provide erbium luminescence in these systems. However, with the synthesis methods for different $\text{YPO}_4\text{:Er,Yb}$ materials described above, this is not achieved.

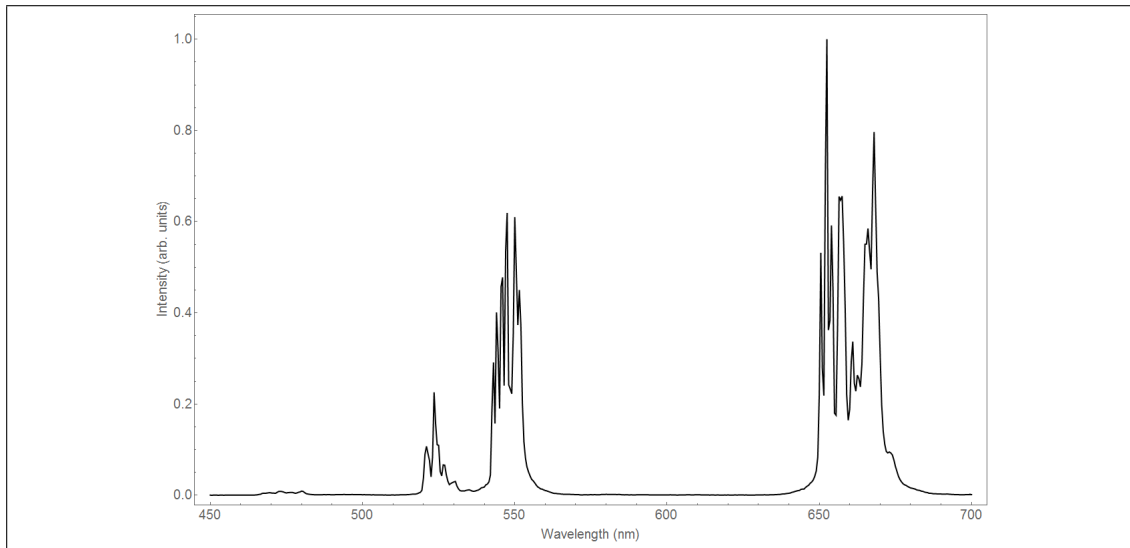


Figure 4.35: Emission spectrum of bulk YPO₄:Er,Yb ($\lambda_{ex} = 980$ nm).

Chapter 5

Conclusions

In this chapter, conclusions on the applicability of the different lanthanide-doped rare earth phosphate materials for nanothermometry will be discussed.

5.1 LaPO₄:Dy,Ce nanoparticles for nanothermometry

As discussed in section 4.1, dysprosium-cerium co-doped LaPO₄ nanoparticles show temperature dependent emission after excitation at $\lambda_{ex} = 285$ nm. Upon heating of the sample, the intensity ratio of the emission peaks around $\lambda = 455$ nm ($^4I_{15/2} \rightarrow ^6H_{15/2}$) and $\lambda = 480$ nm ($^4F_{9/2} \rightarrow ^6H_{15/2}$) increases, indicating that this material can be applicable for nanothermometry. The dysprosium luminescence is improved after coating of the particles with a pure LaPO₄ shell, as confirmed by time-resolved photoluminescence measurements, and subsequent coating of the particles with a silica shell improves the thermal stability of the dysprosium emission, up to a temperature of ~ 450 °C, versus ~ 250 °C for the uncoated particles.

Although the emission intensity ratios are not perfectly reproduced after multiple heating cycles, temperature dependent emission is clearly observed, with a linear dependency of the logarithm of the emission intensity ratios on temperature in the range of $T = 100$ °C – 450 °C. This indicates that, with proper calibration, information about the local temperature can be obtained by analyzing the emission intensity ratios from the dysprosium emission.

Furthermore, as discussed in section 4.2, it is possible to obtain dysprosium emission from dysprosium-cerium co-doped LaPO₄ nanoparticles, after linking the particles to a gold surface, using lipoamide as a linker. This indicates that local surface temperature variations, as a result of surface plasmon induced effects, can, in principle, be measured, using LaPO₄:Dy,Ce as nanothermometers. However, the particles studied in this thesis, i.e. LaPO₄:Dy,Ce without further shell growth, do not show high enough emission intensity in order to experimentally obtain these temperature dependent measurements, such that improvements of this system are necessary. Due to time constraints, experiments with coated LaPO₄:Dy,Ce nanoparticles on a gold surface have not been performed.

5.2 LaPO₄:Eu nanoparticles for nanothermometry

As discussed in section 4.3, europium-doped LaPO₄ nanoparticles show temperature dependent emission after excitation at $\lambda_{ex} = 255$ nm. Upon heating of the sample, the intensity ratio of the emission peaks around $\lambda = 560$ nm ($^5D_1 \rightarrow ^7F_0$) and $\lambda = 570$ nm – 750 nm ($^5D_0 \rightarrow ^7F_J$)

increases, indicating that this material can be applicable for nanothermometry. The europium luminescence is improved after coating of the particles with a pure LaPO_4 shell. Due to a lack of time, further studies of temperature dependent emission in $\text{LaPO}_4:\text{Eu}$ materials were not performed.

However, the preliminary results presented here show that $\text{LaPO}_4:\text{Eu}$ nanoparticles show temperature dependent emission up to a temperature of $\sim 300^\circ\text{C}$. Although the logarithms of the emission intensity ratios do not show a linear dependency on the temperature in the range of room temperature up to 300°C , if reproducible, information about the temperature could be obtained from the emission intensity data, by calibration of the data with higher order fits.

Furthermore, europium-doped LaPO_4 nanoparticles show a higher emission intensity, compared to dysprosium-cerium co-doped LaPO_4 nanoparticles, indicating that $\text{LaPO}_4:\text{Eu}$ is a promising alternative to $\text{LaPO}_4:\text{Dy,Ce}$ to obtain temperature dependent emission at lower concentrations of nanoparticles.

5.3 $\text{LaPO}_4:\text{Er,Yb}$ nanoparticles for nanothermometry

As discussed in section 4.4, with the current synthesis techniques, erbium emission is not observed in $\text{LaPO}_4:\text{Er,Yb}$ nanoparticles. This might be due to concentration quenching, since erbium emission from erbium-ytterbium co-doped nanoparticles has been reported at lower dopant concentrations (2 mol% Er, 18 mol% Yb in this report versus 0.1 mol% Er, 0.1 mol% Yb in literature). Furthermore, incorporation of the erbium/ytterbium dopants into the LaPO_4 host lattice could not be confirmed with the analysis techniques used in this study, such that further experiments are needed in order to explain the absence of erbium emission in nanocrystalline erbium-ytterbium co-doped LaPO_4 nanoparticles.

5.4 $\text{YPO}_4:\text{Er,Yb}$ nanoparticles for nanothermometry

As discussed in section 4.5, erbium/ytterbium dopants can be successfully incorporated in a YPO_4 host lattice. Although erbium emission is observed in bulk $\text{YPO}_4:\text{Er,Yb}$, corresponding nanoparticles do not show erbium luminescence. This indicates that more control over the synthesis of the nanoparticles (e.g. the ability to coat the surface of the nanoparticles) could provide luminescent erbium-ytterbium co-doped YPO_4 nanoparticles. However, with the current synthesis techniques, this is not achieved. Additionally, concentration quenching might influence the luminescent properties of the nanoparticles, such that lowering the dopant concentrations might provide erbium luminescence in this system.

Chapter 6

Outlook

The results discussed in this thesis provide a variety of new, interesting subjects of research, some of which are listed below.

LaPO₄:Dy,Ce

- LaPO₄:Dy,Ce coating on gold nanoparticles with more product could be attempted, in order to obtain enough product material to measure temperature dependent dysprosium emission on the gold surface.
- Coating of gold nanoparticles with core-shell LaPO₄:Dy,Ce/LaPO₄ nanoparticles could be attempted, in order to enhance the dysprosium emission from the gold surface.

LaPO₄:Eu

- Silica coating of LaPO₄:Eu/LaPO₄ nanoparticles could be attempted, in order to enhance the thermal stability and study temperature dependent europium emission above 300 °C.
- Heating cycles could be applied to (silica coated) LaPO₄:Eu/LaPO₄ nanoparticles, in order to study the thermal quenching and reproducibility of the temperature dependent europium emission.
- Coating of gold nanoparticles with LaPO₄:Eu nanoparticles could be attempted, in order to study temperature dependent europium emission from the gold surface.

REPO₄:Er,Yb

- Temperature dependent emission measurements could be performed on bulk YPO₄:Er,Yb, in order to check if temperature dependent erbium emission is observed in this material.
- In addition to YPO₄:Er,Yb nanoparticles, other rare earth phosphate nanoparticles could be synthesized in order to gain more control over the particle formation and observe erbium luminescence. Lutetium phosphate, for example, could be a viable option.

Chapter 7

Acknowledgements

The work presented in this thesis would not have been possible without the help of many dedicated people. In this chapter, I would like to express my gratitude for everyone involved.

First of all, I would like to thank my daily supervisor, Robin Geitenbeek. I have experienced your personal and open style of supervision as very pleasant and informative, both on a scientific level and on a personal level. Your dedication and knowledge have been of great help during my project and from the beginning you have been able to motivate me and challenge me to make this project a success. Thanks to you, I will be able to look back on a very nice and interesting time in my life as a student.

Secondly, I would like to thank prof. dr. Andries Meijerink, for giving me the opportunity to do my master's project at the Condensed Matter and Interfaces group. I am also very grateful for the informative meetings and discussions we had. Your scientific knowledge and interest was very much appreciated during the discussions of my plans and results.

Finally, I would like to thank all the people at CMI, for being helpful whenever I had questions or problems, and, more generally, for the very nice and warm atmosphere that I experienced during my time at CMI. Although I was not always there for social activities, I have always felt welcome, which is greatly appreciated. Of all the people at CMI, I would like to specifically thank the master's students for the nice atmosphere in our master's room, and helpfulness with all kinds of questions.

Appendices

List of appendices

- Appendix A: Dieke diagramPage 65
- Appendix B: ChemicalsPage 66
- Appendix C: $\text{LaPO}_4\text{:Dy,Ce}$ -coated gold nanoparticles; coating procedurePage 67
- Appendix D: BibliographyPage 68

Appendix A

Dieke diagram

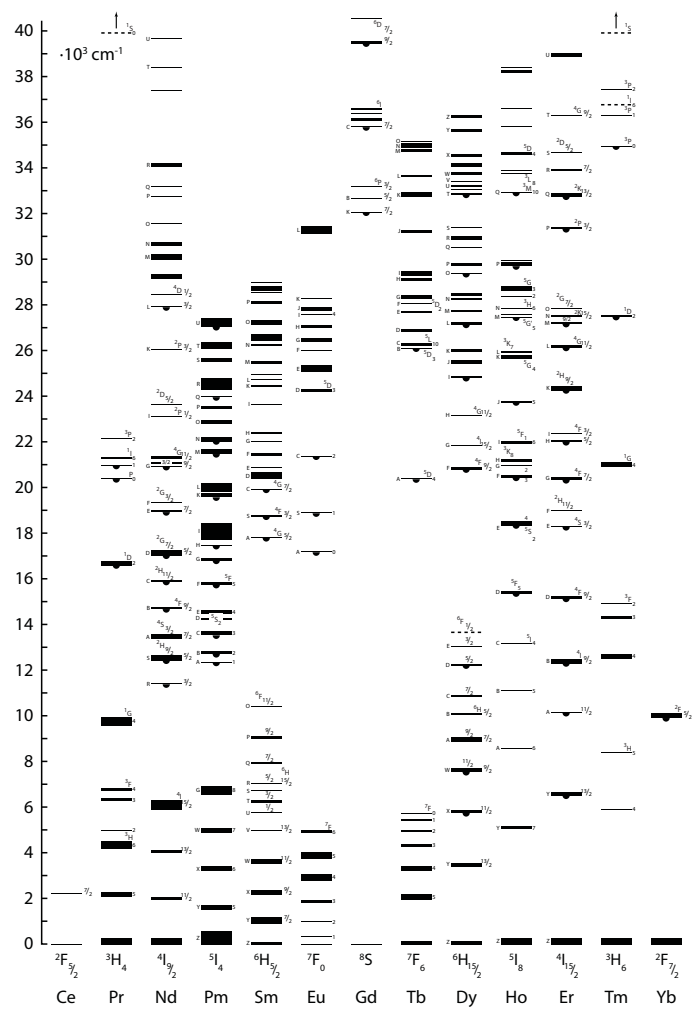


Figure A.1: Dieke diagram

Appendix B

Chemicals

Name	Purity	Formula	Manufacturer
Ammonium hydroxide (aqueous)	28.0 wt%	NH ₄ OH	Sigma-Aldrich
Cerium(III) chloride heptahydrate	99.9 %	CeCl ₃ · 7 H ₂ O	Sigma-Aldrich
Deionized water ¹	-	H ₂ O	Ondeo
Diammonium phosphate	99.99 %	(NH ₄) ₂ HPO ₄	Sigma-Aldrich
Dihexyl ether	97 %	(C ₆ H ₁₃) ₂ O	Sigma-Aldrich
Diphenyl ether	99 %	(C ₆ H ₅) ₂ O	Sigma-Aldrich
Dysprosium(III) chloride hexahydrate	99.99 %	DyCl ₃ · 6 H ₂ O	Sigma-Aldrich
Erbium(III) chloride hexahydrate	99.9 %	ErCl ₃ · 6 H ₂ O	STREM Chemicals
Erbium(III) oxide	99.99 %	Er ₂ O ₃	Highways Int.
Ethanol (anhydrous)	96 %	C ₂ H ₅ OH	Alfa Aesar
Ethanol (flushing)	Tech. grade	C ₂ H ₅ OH	Interchem
IGEPAL CO-520 ²	-	C ₁₅ H ₂₄ O(C ₂ H ₄ O) _n	Sigma-Aldrich
Lanthanum(III) chloride hexahydrate	99.9 %	LaCl ₃ · 6 H ₂ O	Strem Chemicals
Lanthanum(III) oxide	99.5 %	La ₂ O ₃	Merck
Methanol	99.8 %	CH ₃ OH	Sigma-Aldrich
Phosphoric acid	99.9 %	H ₃ PO ₄	Sigma-Aldrich
Sodium polyphosphate	96 %	(NaPO ₃) _n	Sigma-Aldrich
Tetraethyl orthosilicate	99.999 %	Si(OC ₂ H ₅) ₄	Sigma-Aldrich
Toluene	99.9 %	C ₆ H ₅ CH ₃	VWR Chemicals
Tributyl amine	99.0 %	(C ₄ H ₉) ₃ N	Sigma-Aldrich
Tributyl phosphate	99.0 %	(C ₄ H ₉) ₃ PO ₄	Sigma-Aldrich
Ytterbium(III) chloride hexahydrate	99.9 %	YbCl ₃ · 6 H ₂ O	STREM Chemicals
Ytterbium(III) oxide	99.99 %	Yb ₂ O ₃	Highways Int.
Yttrium(III) chloride hexahydrate	99.99 %	YCl ₃ · 6 H ₂ O	Sigma-Aldrich
Yttrium(III) nitrate hexahydrate	99.8 %	Y(NO ₃) ₃ · 6 H ₂ O	Sigma-Aldrich
Yttrium(III) oxide	99.97 %	Y ₂ O ₃	Koch Light Lab.

Table B.1: An overview of the chemicals used

¹Obtained from an Ondeo Purite Select deionizer

²No purity information available; average $M_n = 441$ ($n \sim 5$)

Appendix C

LaPO₄:Dy,Ce-coated gold nanoparticles; coating procedure

In order to coat the surface of gold nanoparticles with LaPO₄:Dy,Ce nanoparticles, 1.08 mg lipoamide in 10 mL ethanol was added to $\sim 1.38 \times 10^{12}$ gold particles in 20 mL. The mixture was washed to remove excess lipoamide ligands and subsequently $\sim 21 \mu\text{g}$ LaPO₄:Dy,Ce nanoparticles were added. The resulting mixture was washed again to remove unadsorbed particles and the product was redispersed in 20 mL deionized water.

Appendix D

Bibliography

- [1] C. D S Brites, P. P. Lima, N. J O Silva, A. Millán, V. S. Amaral, F. Palacio, and L. D. Carlos. Thermometry at the nanoscale using lanthanide-containing organic-inorganic hybrid materials. *Journal of Luminescence*, 133(16):230–232, 2013.
- [2] Daniel Jaque and Fiorenzo Vetrone. Luminescence nanothermometry. *Nanoscale*, 4(15):4301–4326, aug 2012.
- [3] Seid Sadat, Aaron Tan, Yi Jie Chua, and Pramod Reddy. Nanoscale thermometry using point contact thermocouples. *Nano Letters*, 10(7):2613–2617, jul 2010.
- [4] Yihua Gao, Yoshio Bando, Zongwen Liu, Dmitri Golberg, and Haruyuki Nakanishi. Temperature measurement using a gallium-filled carbon nanotube nanothermometer. *Applied Physics Letters*, 83(14):2913–2915, oct 2003.
- [5] Jui Ming Yang, Haw Yang, and Liwei Lin. Quantum dot nano thermometers reveal heterogeneous local thermogenesis in living cells. *ACS Nano*, 5(6):5067–5071, jun 2011.
- [6] Laura Martinez Maestro, Emma Martín Rodríguez, Francisco Sanz Rodríguez, M C Iglesias-de la Cruz, Angeles Juarranz, Rafik Naccache, Fiorenzo Vetrone, Daniel Jaque, John a Capobianco, and José García Solé. CdSe quantum dots for two-photon fluorescence thermal imaging. *Nano letters*, 10(12):5109–15, dec 2010.
- [7] Y.P. Varshni. Temperature dependence of the energy gap in semiconductors. *Physica*, 34(1):149–154, jan 1967.
- [8] David Ross, Michael Gaitan, and Laurie E Locascio. Temperature Measurement in Microfluidic Systems Using a Temperature-Dependent Fluorescent Dye. *Analytical Chemistry*, 73(17):4117–4123, sep 2001.
- [9] Xia Xu, Zhuo Wang, Pengpeng Lei, Yingning Yu, Shuang Yao, Shuyan Song, Xiuling Liu, Yue Su, Lile Dong, Jing Feng, and Hongjie Zhang. α -NaYb(Mn)F₄:Er³⁺/Tm³⁺@NaYF₄ UCNP as Band-Shape Luminescent Nanothermometers over a Wide Temperature Range. *ACS Applied Materials & Interfaces*, 7(37):20813–20819, sep 2015.
- [10] L. P. Goss, A. A. Smith, and M. E. Post. Surface thermometry by laserinduced fluorescence. *Review of Scientific Instruments*, 60(12):3702–3706, dec 1989.
- [11] Lawrence P. Bevy. *Trends in Catalysis Research*. Nova Science Publishers, 2006.

- [12] James R. Adleman, David A. Boyd, David G. Goodwin, and Demetri Psaltis. Heterogenous Catalysis Mediated by Plasmon Heating. *Nano Letters*, 9(12):4417–4423, dec 2009.
- [13] Nadine Harris, Michael J. Ford, and Michael B. Cortie. Optimization of Plasmonic Heating by Gold Nanospheres and Nanoshells. *The Journal of Physical Chemistry B*, 110(22):10701–10707, jun 2006.
- [14] Catherine E. Housecroft and Alan G. Sharpe. *Inorganic chemistry*. Prentice Hall, first edition, 2001.
- [15] T. Ala-Kleme, J.-C. G. Bünzli, H. Bazin, S. V. Eliseeva, S. Faulkner, P. Hänninen, H. Härmä, I. Hemmilä, I. Hyppänen, J. Kankare, S. Kulmala, A. Kuusisto, V. Laitala, G. Mathis, T. Nann, M. Schäferling, T. Soukka, C. Spangler, U.-H. Stenman, J. Suomi, D. Sykes, H. J. Tanke, P. A. Tanner, H.-Q. Wang, and M. H. V. Werts. *Lanthanide Luminescence*, volume 7 of *Springer Series on Fluorescence*. Springer Berlin Heidelberg, Berlin, Heidelberg, 2011.
- [16] Chunhui Huang and Zuqiang Bian. Introduction. In *Rare Earth Coordination Chemistry: Fundamentals and Applications*, chapter 1, pages 1–40. 2010.
- [17] G. Blasse and B. C. Grabmaier. *Luminescent Materials*. Springer Science & Business Media, first edition, 1994.
- [18] Baldassare Di Bartolo, John Collins, and Luciano Silvestri, editors. *Nano-Optics: Principles Enabling Basic Research and Applications*. NATO Science for Peace and Security Series B: Physics and Biophysics. Springer Netherlands, Dordrecht, 2017.
- [19] P. W. Atkins. *Physical chemistry*. Oxford University Press, sixth edition, 1998.
- [20] D. F. Shriver and P. W. Atkins. *Inorganic Chemistry*. Oxford University Press, fourth edition, 2006.
- [21] Simon Cotton. *Lanthanide and Actinide Chemistry*. John Wiley & Sons, Ltd, Chichester, UK, first edition, jan 2006.
- [22] Peter A. Tanner and Chang Kui Duan. Luminescent lanthanide complexes: Selection rules and design. *Coordination Chemistry Reviews*, 254(23-24):3026–3029, 2010.
- [23] Peter A. Tanner. Some misconceptions concerning the electronic spectra of tri-positive europium and cerium. *Chemical Society Reviews*, 42(12):5090, 2013.
- [24] Jan W. Stouwdam, Gerald A. Hebbink, Jurriaan Huskens, and Frank C. J. M. van Veggel. Lanthanide-Doped Nanoparticles with Excellent Luminescent Properties in Organic Media. *Chemistry of Materials*, 15(24):4604–4616, dec 2003.
- [25] Piers Andrew. Forster Energy Transfer in an Optical Microcavity. *Science*, 290(5492):785–788, oct 2000.
- [26] Naohiro Ishiwada, Satoko Fujioka, Toshihisa Ueda, and Takeshi Yokomori. Co-doped Y2O3:Tb3+/Tm3+ multicolor emitting phosphors for thermometry. *Optics Letters*, 36(5):760–2, mar 2011.
- [27] Carlos D S Brites, Patricia P. Lima, Nuno J O Silva, Angel Millán, Vitor S. Amaral, Fernando Palacio, and Luís D. Carlos. A luminescent molecular thermometer for long-term absolute temperature measurements at the nanoscale. *Advanced Materials*, 22(40):4499–4504, oct 2010.

- [28] Yuanjing Cui, Hui Xu, Yanfeng Yue, Zhiyong Guo, Jiancan Yu, Zhenxia Chen, Junkuo Gao, Yu Yang, Guodong Qian, and Banglin Chen. A luminescent mixed-lanthanide metal-organic framework thermometer. *Journal of the American Chemical Society*, 134(9):3979–3982, mar 2012.
- [29] Baldassare D. Di Bartolo, John Collins, and Luciano Silvestri. *Nano-structures for optics and photonics: Optical strategies for enhancing sensing, imaging, communication and energy conversion*. NATO Science for Peace and Security Series B: Physics and Biophysics. Springer Netherlands, Dordrecht, first edition, 2015.
- [30] Joseph R. Lakowicz, editor. *Principles of Fluorescence Spectroscopy*. Springer US, Boston, MA, 2006.
- [31] O. Lehmann, H. Meyssamy, K. Kömpe, H. Schnablegger, and M. Haase. Synthesis, Growth, and Er 3+ Luminescence of Lanthanide Phosphate Nanoparticles . *The Journal of Physical Chemistry B*, 107(30):7449–7453, jul 2003.
- [32] Karsten Kömpe, Holger Borchert, Jörg Storz, Arun Lobo, Sorin Adam, Thomas Möller, and Markus Haase. Green-Emitting CePO₄:Tb/LaPO₄ Core-Shell Nanoparticles with 70 % Photoluminescence Quantum Yield. *Angewandte Chemie International Edition*, 42(44):5513–5516, nov 2003.
- [33] Olaf Lehmann, Karsten Kömpe, and Markus Haase. Synthesis of Eu³⁺-doped core and core/shell nanoparticles and direct spectroscopic identification of dopant sites at the surface and in the interior of the particles. *Journal of the American Chemical Society*, 126(45):14935–14942, nov 2004.
- [34] A. Miller and D. M. Finlayson. *Laser Sources and Applications*. The Scottish Universities Summer School in Physics Publications, Edinburgh, 1997.
- [35] Michel J. F. Dignonnet. *Rare-Earth-Doped Fiber Lasers and Amplifiers, Revised and Expanded*, volume 71 of *Optical Science and Engineering*. CRC Press, 2 edition, may 2001.
- [36] B. Faure, W. Blanc, B. Dussardier, and G. Monnom. Improvement of the Tm³⁺:3H₄ level lifetime in silica optical fibers by lowering the local phonon energy. *Journal of Non-Crystalline Solids*, 353(29):2767–2773, sep 2007.
- [37] Valérie Buissette, Mélanie Moreau, Thierry Gacoin, Jean-Pierre Boilot, Jean-Yves Chane-Ching, and Thierry Le Mercier. Colloidal Synthesis of Luminescent Rhabdophane LaPO₄:Ln³⁺ · x H₂O (Ln = Ce, Tb, Eu; x ≈ 0.7) Nanocrystals. *Chemistry of Materials*, 16(19):3767–3773, sep 2004.
- [38] Hongliang Zhu and Diantai Zuo. Highly Enhanced Photoluminescence from YVO₄:Eu³⁺@YPO₄ Core/Shell Heteronanostructures. *The Journal of Physical Chemistry C*, 113(24):10402–10406, jun 2009.
- [39] Rolf Koole, Matti M. Van Schooneveld, Jan Hilhorst, Celso Mello De Donegal, Dannis C. ’T Hart, Alfons Van Blaaderen, Daniel Vanmaekelbergh, and Andries Meijerink. On the incorporation mechanism of hydrophobic quantum dots in silica spheres by a reverse microemulsion method. *Chemistry of Materials*, 20(7):2503–2512, 2008.
- [40] Anke Oertel, Cornelia Lengler, Thomas Walther, and Markus Haase. Photonic Properties of Inverse Opals Fabricated from Lanthanide-Doped LaPO₄ Nanocrystals. *Chemistry of Materials*, 21(16):3883–3888, aug 2009.

- [41] P. Scherrer. Bestimmung der Grösse und der inneren Struktur von Kolloidteilchen mittels Röntgenstrahlen. *Nachrichten von der Gesellschaft der Wissenschaften zu Göttingen, Mathematisch-Physikalische Klasse*, pages 98–100, 1918.
- [42] A. K. Singh. *Advanced X-ray Techniques in Research and Industry*. IOS Press, 2005.
- [43] Yu-Chun Li, Yen-Hwei Chang, Yu-Feng Lin, Yee-Shin Chang, and Yi-Jing Lin. Synthesis and luminescent properties of Ln^{3+} (Eu^{3+} , Sm^{3+} , Dy^{3+})-doped lanthanum aluminum germanate $\text{LaAlGe}_2\text{O}_7$ phosphors. *Journal of Alloys and Compounds*, 439(1-2):367–375, jul 2007.
- [44] Juan Li, Chunxiang Zhang, Qiang Tang, Jingquan Hao, Yanli Zhang, Qiang Su, and Shubin Wang. Photoluminescence and thermoluminescence properties of dysprosium doped zinc metaborate phosphors. *Journal of Rare Earths*, 26(2):203–206, apr 2008.
- [45] S. Chemingui, M. Ferhi, K. Horchani-Naifer, and M. Férid. Synthesis and luminescence characteristics of Dy^{3+} doped $\text{KLa}(\text{PO}_3)_4$. *Journal of Luminescence*, 166:82–87, oct 2015.
- [46] Heike Meyssamy, Karsten Riwozki, Andreas Kornowski, Sabine Naused, and Markus Haase. Wet-Chemical Synthesis of Doped Colloidal Nanomaterials: Particles and Fibers of $\text{LaPO}_4\text{:Eu}$, $\text{LaPO}_4\text{:Ce}$, and $\text{LaPO}_4\text{:Ce,Tb}$. *Advanced Materials*, 11(10):840–844, jul 1999.
- [47] Karsten Riwozki, Heike Meyssamy, Heimo Schnablegger, Andreas Kornowski, and Markus Haase. Liquid-Phase Synthesis of Colloids and Redispersible Powders of Strongly Luminescing $\text{LaPO}_4\text{:Ce,Tb}$ Nanocrystals. *Angewandte Chemie International Edition*, 40(3):573–576, feb 2001.
- [48] M Yu, J Lin, and J Fang. Silica Spheres Coated with $\text{YVO}_4\text{:Eu}^{3+}$ Layers via SolGel Process: A Simple Method To Obtain Spherical CoreShell Phosphors. *Chemistry of Materials*, 17(7):1783–1791, apr 2005.
- [49] N. Shanta Singh, R.S. Ningthoujam, M. Niraj Luwang, S. Dorendrajit Singh, and R.K. Vatsa. Luminescence, lifetime and quantum yield studies of $\text{YVO}_4\text{:Ln}^{3+}$ ($\text{Ln}^{3+}=\text{Dy}^{3+}$, Eu^{3+}) nanoparticles: Concentration and annealing effects. *Chemical Physics Letters*, 480(4-6):237–242, oct 2009.
- [50] H. Wang, M. Yu, C.K. Lin, and J. Lin. Coreshell structured $\text{SiO}_2\text{:YVO}_4\text{:Dy}^{3+}/\text{Sm}^{3+}$ phosphor particles: Solgel preparation and characterization. *Journal of Colloid and Interface Science*, 300(1):176–182, aug 2006.
- [51] Ganngam Phaomei, R.S. Ningthoujam, W. Rameshwor Singh, Naorem Shanta Singh, M. Niraj Luwang, R. Tewari, and R.K. Vatsa. Low temperature synthesis and luminescence properties of re-dispersible Eu^{3+} doped LaPO_4 nanorods by ethylene glycol route. *Optical Materials*, 32(5):616–622, mar 2010.
- [52] N. Yaiphaba, R.S. Ningthoujam, N. Shanta Singh, R.K. Vatsa, and N. Rajmuhon Singh. Probing of inversion symmetry site in Eu^{3+} -doped GdPO_4 by luminescence study: Concentration and annealing effect. *Journal of Luminescence*, 130(1):174–180, jan 2010.
- [53] W. T. Carnall, G. L. Goodman, K. Rajnak, and R. S. Rana. A systematic analysis of the spectra of the lanthanides doped into single crystal LaF_3 . *The Journal of Chemical Physics*, 90(7):3443–3457, apr 1989.

- [54] Marcin Runowski, Krystyna Dąbrowska, Tomasz Grzyb, Paulina Miernikiewicz, and Stefan Lis. Core/shell-type nanorods of Tb³⁺-doped LaPO₄, modified with amine groups, revealing reduced cytotoxicity. *Journal of Nanoparticle Research*, 15(11):2068, nov 2013.
- [55] M. Yu, J. Lin, Z. Wang, J. Fu, S. Wang, H. J. Zhang, and Y. C. Han. Fabrication, Patterning, and Optical Properties of Nanocrystalline YVO₄:A (A = Eu³⁺, Dy³⁺, Sm³⁺, Er³⁺) Phosphor Films via SolGel Soft Lithography. *Chemistry of Materials*, 14(5):2224–2231, may 2002.
- [56] Lokesh Mishra, Anchal Sharma, Amit K. Vishwakarma, Kaushal Jha, M. Jayasimhadri, B.V. Ratnam, Kiwan Jang, A.S. Rao, and R.K. Sinha. White light emission and color tunability of dysprosium doped barium silicate glasses. *Journal of Luminescence*, 169:121–127, jan 2016.
- [57] Carla Cannas, Anna Musinu, Andrea Ardu, Federica Orru, Davide Peddis, Mariano Casu, Roberta Sanna, Fabrizio Angius, Giacomo Diaz, and Giorgio Piccaluga. CoFe₂O₄ and CoFe₂O₄/SiO₂ Core/Shell Nanoparticles: Magnetic and Spectroscopic Study. *Chemistry of Materials*, 22(11):3353–3361, jun 2010.
- [58] D.E. Henrie, R.L. Fellows, and G.R. Choppin. Hypersensitivity in the electronic transitions of lanthanide and actinide complexes. *Coordination Chemistry Reviews*, 18(2):199–224, feb 1976.
- [59] Vincenzo Amendola, Roberto Pilot, Marco Frasconi, Onofrio M Maragò, and Maria Antonia Iatì. Surface plasmon resonance in gold nanoparticles: a review. *Journal of Physics: Condensed Matter*, 29(20):203002, may 2017.
- [60] Wei Li and Joonho Lee. Microwave-Assisted SolGel Synthesis and Photoluminescence Characterization of LaPO₄:Eu³⁺/Li⁺ Nanophosphors. *The Journal of Physical Chemistry C*, 112(31):11679–11684, aug 2008.
- [61] R. Reisfeld, R. A. Velapoldi, L. Boehm, and M. Ish-Shalom. Transition probabilities of europium in phosphate glasses. *The Journal of Physical Chemistry*, 75(26):3980–3983, dec 1971.
- [62] H. M. Farok, H. B. Senin, G. A. Saunders, W. Poon, and H. Vass. Optical and ultrasonic properties of europium phosphate glasses. *Journal of Materials Science*, 29(11):2847–2859, 1994.
- [63] V. Tsaryuk, V. Zolin, and J. Legendziewicz. The structure of ligands and effects of the europium luminescence excitation. *Journal of Luminescence*, 102-103:744–750, may 2003.
- [64] M. Haase, K. Riwotzki, H. Meyssamy, and A. Kornowski. Synthesis and properties of colloidal lanthanide-doped nanocrystals. *Journal of Alloys and Compounds*, 303-304:191–197, may 2000.
- [65] Koen Binnemans. Interpretation of europium(III) spectra. *Coordination Chemistry Reviews*, 295:1–45, jul 2015.
- [66] O.L. Malta. Lanthanide f f transitions hypersensitive to the environment. *Molecular Physics*, 42(1):65–72, jan 1981.
- [67] Shili Gai, Chunxia Li, Piaoping Yang, and Jun Lin. Recent Progress in Rare Earth Micro/Nanocrystals: Soft Chemical Synthesis, Luminescent Properties, and Biomedical Applications. *Chemical Reviews*, 114(4):2343–2389, feb 2014.

- [68] Fiorenzo Vetrone, Rafik Naccache, Alicia Zamarron, Angeles Juarranz de la Fuente, Francisco Sanz-Rodriguez, Laura Martinez Maestro, Emma Martin Rodriguez, Daniel Jaque, Jose Garcia Sole, and John A. Capobianco. Temperature Sensing Using Fluorescent Nanothermometers. *ACS Nano*, 4(6):3254–3258, jun 2010.
- [69] Robin G. Geitenbeek, P. Tim Prins, Wiebke Albrecht, Alfons van Blaaderen, Bert M. Weckhuysen, and Andries Meijerink. NaYF₄:Er³⁺, Yb³⁺/SiO₂ Core/Shell Upconverting Nanocrystals for Luminescence Thermometry up to 900 K. *The Journal of Physical Chemistry C*, 121(6):3503–3510, feb 2017.
- [70] Radosław Lisiecki, Witold Ryba-Romanowski, Adolfo Speghini, and Marco Bettinelli. Luminescence spectroscopy of Er³⁺-doped and Er³⁺, Yb³⁺-codoped LaPO₄ single crystals. *Journal of Luminescence*, 129(5):521–525, may 2009.